

QUANTUM TRANSPORT IN MESOSCOPIC SYSTEM

THESIS SUBMITTED FOR THE DEGREE OF
DOCTOR OF PHILOSOPHY (SCIENCE)
OF THE
UNIVERSITY OF JADAVPUR
2005

SWARNALI BANDOPADHYAY



SATYENDRANATH BOSE NATIONAL CENTRE
FOR BASIC SCIENCES
JD BLOCK, SECTOR 3, SALT LAKE CITY
KOLKATA 700 098, INDIA

QUANTUM TRANSPORT IN MESOSCOPIC SYSTEM

THESIS SUBMITTED FOR THE DEGREE OF
DOCTOR OF PHILOSOPHY (SCIENCE)
OF THE
UNIVERSITY OF JADAVPUR
2005

SWARNALI BANDOPADHYAY



SATYENDRANATH BOSE NATIONAL CENTRE
FOR BASIC SCIENCES
JD BLOCK, SECTOR 3, SALT LAKE CITY
KOLKATA 700 098, INDIA

CERTIFICATE FROM THE SUPERVISOR(S)

This is to certify that the thesis entitled “Quantum Transport in Mesoscopic System” submitted by Smt. Swarnali Bandopadhyay, who got her name registered on 12th November, 2002 for the award of Ph.D.(Science) degree of Jadavpur University, is absolutely based upon her own work under the supervision of Dr. Prosenjit Singha Deo and that neither this thesis nor any part of it has been submitted for any degree/diploma or any other academic award anywhere before.



Prosenjit Singha Deo

Reader,

Satyendranath Bose National Centre For Basic Sciences,
JD Block, Sector 3, Salt Lake City, Kolkata 700098
India

Date : 28/1/05

Dr. Prosenjit Singha Deo
Reader

S. N. Bose National Centre
JD Block, Sector-III
Salt Lake, Kolkata-98

(Signature of the Supervisor(s) & date with official seal)

Acknowledgments

This thesis is the result of almost four and half years of work whereby I have been accompanied and supported by many people. It is a pleasant aspect that I have now the opportunity to express my gratitude to all of them.

First, I would like to thank Dr. Prosenjit Singha Deo, my thesis advisor, for introducing me to the fascinating world of mesoscopic physics.

A large part of my work was done in a close collaboration with Prof. Arun M. Jayannavar. I am deeply indebted to Prof. Jayannavar for his constant support, guidance, patience and encouragement. I appreciate the opportunity to learn from his expertise and dedication to physics.

I would like to extend these words of thanks to Prof. Binayak Dutta-Roy who kept an eye on the progress of my work and always was available whenever I needed his advices.

I'm grateful to Dr. Surajit Sengupta whose support, suggestions and continuous encouragement helped me a lot during my research career.

I'm also grateful to Prof. H. S. Mani. The several hours of discussions we had in which he encouraged me a lot by his valuable comments, enthusiasm and his positive attitude towards science in general.

I wish to thank Dr. P. A. Sreeram. I have benefited a lot from several discussions with him over the years.

It is my pleasure to acknowledge all the supports provided by Prof. Sushanta Datta-Gupta, the Director of SNBNCBS, my host institution.

I would like to thank Dr. Sumathi Rao for granting me a visit to Harishchandra Research Institute, Allahabad in 2001 and for all her time to teach me the techniques of bosonization and Luttinger liquids.

I am very much thankful to my husband, Debasish Chaudhuri, whose patience, understanding and encouragement helped me to fulfill my academic responsibilities. I also benefitted a lot from all the academic discussions that we had during this period.

It was a great pleasure working with my collaborators Dr. Raishma Krishnan, Sourin Das and Colin Benjamin.

I acknowledge the timely help of academic as well as non-academic staffs of S. N. Bose National Centre for Basic Sciences, Kolkata. I would like to specially mention Mr. Swapan Ghosh and Ms. Ruma Mazumdar of the library, Mr. Biman Roy of mailing section for their quick service. I would like to thank Mr. A. K. Sarkar of Accounts section and Mr. S. K. Deb of Administration section for their efficient handling of bureaucratic procedures.

I would like to thank Institute of Physics, Bhubaneswar, where I carried out some parts of the works on 'Quantum current magnification' and 'Tunneling time', for providing me

local hospitality.

Acknowledgements would be little for the close friendship that I enjoyed with Abhishek, Anuj, Kamal, Santa, Samir, Sumana. I feel privileged to have enjoyed the company of my seniors and colleagues Gautamda, Subhrada, Indrada, Monodeepda, Atishda, Rumani, Ram, Mani, Ankush, Arya, Arnab, Deepanjan, Joyee, Suman, Malay.

I would like to thank the following organizations/organizers/convenors for warm hospitality and pleasant stay during the respective conferences/schools/workshops etc. :

1. Condensed Matter Days 2004, N.E.H.U., Shilong, India, 25th-27th August, 2004.
2. Workshop on Quantum Systems out of Equilibrium, **ICTP**, Trieste, Italy, 14th June - 25th June, 2004.
3. Spring College on Science at the Nanoscale, **ICTP**, Trieste, Italy, 24th May - 11th June, 2004.
4. SERC school on Statistical Physics, TIFR, Mumbai-5, India, 16th-28th February, 2004.
5. International Conference on Nano Science and Technology (ICONSAT 2003), Hyatt Regency, Kolkata, India, 17th-20th December, 2003.
6. Condensed Matter Days 2003 (CMDAYS 03), Dept. of Physics, Jadavpur University, Kolkata-32, India, 27th-29th August, 2003.
7. India and Abroad Condensed Matter III, SNBNCBS, Kolkata, India, 3rd and 4th January, 2003.
8. School on Quantum Physics and Information Processing, TIFR, Mumbai-5, India, 18th-27th February, 2002.

List of Publications

1. *Scattering phase shifts in quasi-one-dimension* P. Singha Deo, **Swarnali Bandopadhyay** and Sourin Das, Int. J. Mod. Phys. B, **16**, p 2247 - 2277 (2002).
2. *Survival of $\phi_0/2$ periodicity in presence of incoherence in asymmetric Aharonov-Bohm rings*, C. Benjamin, **Swarnali Bandopadhyay** and A. M. Jayannavar, Solid State Communication **124** p 331 - 334 (2002).
3. *Friedel Sum Rule for single channel quantum wire*, **Swarnali Bandopadhyay** and P. Singha Deo, Phys. Rev. B **68**, 113301 (2003) (4 pages).
4. *Hartman effect in presence of Aharonov Bohm flux*, **Swarnali Bandopadhyay**, Raishma Krishnan and A. M. Jayannavar, Sol. St. Commun. **131**, p 447- 451 (2004)
5. *Quantum Current Magnification in a multi-channel mesoscopic ring*, **Swarnali Bandopadhyay**, P. Singha Deo and A. M. Jayannavar, Phys. Rev. B **70**, 075315 (2004).
6. *Understanding the Fano Resonance : through Toy Models*, **Swarnali Bandopadhyay**, Binayak Dutta-Ray and H.S.Mani, Am. J. Phys., **72**, p 1501 - 1507 (2004).
7. *Hartman effect and non-locality in quantum networks*, **Swarnali Bandopadhyay** and A. M. Jayannavar, Phys. Lett. A, **335**, p 266-273 (2005).
8. *Phase delay time and superluminal propagation in barrier tunneling*, **Swarnali Bandopadhyay** and A. M. Jayannavar, to appear in the proceedings of Condensed Matter Days 2004 (2005); quant-ph/0411161.

Contents

Acknowledgments	iii
List of Publications	v
1 Introduction	1
1.1 Mesoscopic Physics	1
1.1.1 Fabrication of high mobility samples	2
1.1.2 Observed Quantum phenomena in Mesoscopic Conductor	3
1.2 This Thesis	7
2 Basics of electron transport in mesoscopic system	9
2.1 Introduction	9
2.2 Effect of environment on mesoscopic conductor	9
2.3 Landauer-Büttiker conductance formula:	11
2.3.1 General Landauer formula	12
2.3.2 Büttiker solution	15
2.4 Experiment on phase-shift:	15
2.5 Phase time for tunneling particle	17
2.6 Persistent Current	18
2.7 Current magnification	21
2.8 Scattering matrix for Q1D systems	21
3 Friedel-Sum-Rule in Quasi-one-dimensional Quantum Wire	25
3.1 Introduction	25
3.1.1 FSR <i>for</i> isolated mesoscopic conductor	26
3.2 FSR <i>for</i> open mesoscopic conductor	26
3.3 Scattering in one-dimension and negative values of $d\theta_f/dE$	27
3.4 FSR <i>for</i> single channel Q1D quantum wire	31
3.4.1 First principle calculation of scattering matrix and DOS in Q1D quantum wire	32
3.4.2 Results and Discussion	34
3.5 Phase shifts, phase times and FSR in multi-channel Q1D quantum wire	36
3.5.1 Wigner delay time in quasi-one-dimensions	38
3.5.2 Density of States and Friedel sum rule in quasi-one-dimension	47
3.5.3 Phase Behavior at Critical Energies	49

3.6	Fano resonance	50
3.6.1	Dirac Delta model for the Fano resonance	52
3.6.2	Discussion and results :	57
3.6.3	Conclusions	58
4	Quantum current magnification in a multi-channel mesoscopic ring	61
4.1	results and discussions	65
4.2	Possible Experiment	73
4.3	conclusion	74
5	Phase time for tunneling particle	79
5.1	Introduction	79
5.2	Hartman effect in presence of AB-flux	81
5.2.1	Ring connected with two leads	82
5.2.2	Ring connected with one lead	86
5.3	Hartman effect and non-locality in quantum networks	91
5.3.1	Theoretical treatment	92
5.3.2	Results and Discussions	94
5.4	Conclusions	98
6	Conclusions	101
A	Scattering and transition amplitudes in Q1D quantum wire	103
A.1	Mode rescaling procedure	103
A.2	transmission and reflection amplitudes	106
A.3	Transition amplitude from propagating to evanescent mode	107
B	Global DOS in a Q1D quantum wire	109
C	Scattering amplitudes from double-delta potential in 1D	113
D	Location of the transmission zero	117
E	Location of the Resonance and determination of the width	119
	References	121

Chapter 1

Introduction

1.1 Mesoscopic Physics

In 1947, with the invention of world's first transistor [1], a trend towards miniaturization started. In his seminal lecture entitled "There's plenty of room at the bottom" [2] delivered on 29th December 1959 at the annual meeting of the American Physical Society at the California Institute of Technology, R. P. Feynman discussed, predicted and challenged the future generations of physicists to unravel the beauty and huge potential utility lying in the realm of 'small' world. Mesoscopic physics is the branch of solid state physics that deals with this world of 'small', the system sizes intermediate between the length scale regimes of atoms and molecules and the macroscopic world. Since the building of first transistors, the size of the devices have steadily shrunk, coming down to the micrometer scale in 1980's. The technological drive of miniaturization is to make new devices which occupy less space, can contain more information, can perform operations faster and also cost effective. This drive of miniaturization has lead us into the world of 'nanoscience'. Besides technological aspects this leads us to several fundamental issues of quantum mechanics, possibilities and experimental verifications of new phenomena. Furthermore, the measurements of most of the basic effects requires little more than a conductance measurement.

Massive industrial research and development efforts towards the miniaturization of semiconductor devices has produced sophisticated crystal growth and lithographic techniques, which allow fabrication of artificial structures, or devices having dimensions of a few atomic spacings. Nowadays it is possible to confine electrons in a conductor with a lateral extent of 100 nm or less, resulting in narrow quantum wires, constrictions and quantum dots. The small size of these structures largely eliminates the defect scattering and one can get extremely high mobility conducting channels, thus motivating interest in ballistic transport. Physical properties of such systems can differ significantly from what one would expect on the basis of classical description. These systems exhibit several new phenomena as their dimension become shorter than some relevant physical length scales. The only relevant process in mesoscopic systems having dimensions less than the phase coherence length l_ϕ is elastic scattering. This l_ϕ is the typical length on which a wave packet can travel without losing its phase coherence. l_ϕ depends on coupling of electron to other degrees of freedom like phonons, electromagnetic fluctuations, other electrons, magnetic impurities etc. The phase

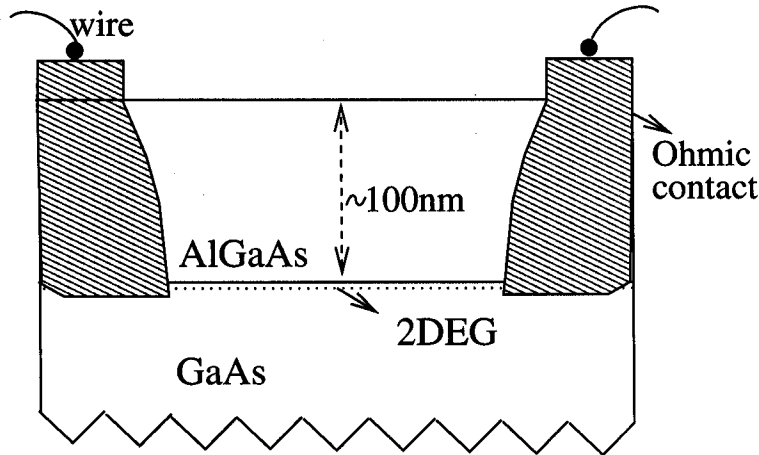


FIGURE 1.1: Schematic cross section of a GaAs/AlGaAs heterostructure. The 2DEG is located at the interface.

breaking scattering of electrons due to these other degrees of freedom decreases with decreasing temperature, thereby increasing l_ϕ . If system size is much much larger than l_ϕ we recover classical behaviour, due to average over several phase-breaking processes. One can by tuning temperature, observe quantum effects at low temperatures which crossover to classical results at high temperatures. In low temperature properties of mesoscopic systems, quantum interference plays the most crucial role. Except for quantum interference, discreteness of charge, electron numbers being even or odd, specific techniques (two or four probe) of conductance measurement, system lead coupling strength etc. control the observed mesoscopic phenomena. As the phase coherence is maintained over the entire sample, several intrinsic quantum mechanical phenomena have been observed [3, 4]. Convincing demonstrations of quantum transport regime have come from experiments in thin metal or semiconductor films or multiply connected structures. Some of the observed quantum phenomena include breakdown of Ohm's law [5], quantized conductance in the point contact [6, 7], breakdown of Onsager's symmetry relation [8], Integral and Fractional Quantum Hall Effect (IQHE and FQHE) [5, 9], Aharonov-Bohm oscillations in the magnetoresistance [10, 11], universal conductance fluctuations, persistent current, reproducible sample specific non self-averaging fluctuations in conductance as the magnetic field or the chemical potential is varied. A few such notable mesoscopic phenomena are described below following the 'fabrication of mesoscopic samples'.

1.1.1 Fabrication of high mobility samples

In a modulation-doped GaAs/ $\text{Al}_x\text{Ga}_{1-x}\text{As}$ heterostructure the two-dimensional electron gas (2DEG) is formed at the interface (see Fig.1.1) [9]. On the GaAs substrate a layer of typically 100nm $\text{Al}_x\text{Ga}_{1-x}\text{As}$ is grown. Somewhere halfway in the $\text{Al}_x\text{Ga}_{1-x}\text{As}$ layer there is a thin layer where the Ga atoms are replaced by Si donor atoms. With a proper amount of Si one finds that at low temperature the only mobile electrons are located at the GaAs/ $\text{Al}_x\text{Ga}_{1-x}\text{As}$

interface. These free electrons are attracted by the GaAs since they can lower their energy in this smaller band gap material. They are also held as close as possible to their ionized Si^+ donors and thus they form a thin conducting layer near the interface. Since GaAs and $\text{Al}_x\text{Ga}_{1-x}\text{As}$ can form a nearly perfect interface on the atomic scale and since the Si donors are spatially separated, the electrons experience very little scattering. In n-type or p-type semiconductor where the sample is doped with impurities which are necessary to create carriers, the sample loses the periodicity and scattering at these impurities reduces mobility. But in the 2DEG the donors are spatially separated from the region of carriers and hence the high mobility. This 2DEG has a low electron density which implies a large Fermi-wavelength, comparable to the dimensions of the smallest structures that can be fabricated. For example, at low temperature in GaAs/ $\text{Al}_{0.3}\text{Ga}_{0.7}\text{As}$ semiconductor heterostructure, it is possible to reach mobilities of $10^6 \text{cm}^2/\text{Vs}$, which leads to an elastic mean-free-path of the order of $10 \mu\text{m}$ and an inelastic mean-free path even larger. A unique feature of a 2DEG is that it can be given any desired shape using lithographic techniques. The shape is defined by etching a pattern (resulting in permanent removal of the electron gas), or by electrostatic depletion using a patterned gate electrode (which is reversible). A local (partial) depletion of the 2DEG below a gate is associated with a local increase of the electrostatic potential, relative to the undepleted region. At the boundaries of the gate a potential step is thus induced in the 2DEG. The potential step is smooth, because of the large lateral depletion length (of the order of 100 nm for a step height of 10 meV). This large depletion length is at the basis of the split-gate technique [12, 13], used to define narrow channels of variable width with smooth boundaries.

One of the simplest devices that may be fabricated using this technique is the quantum point contact (QPC), which basically is a very short and narrow constriction in the 2DEG. The width of this constriction being comparable to the Fermi wavelength, this is called QPC. At low temperatures, the conductance of such a QPC is approximately quantized in units of $2e^2/h$.

1.1.2 Observed Quantum phenomena in Mesoscopic Conductor

Quantized conductance : In 1988, van Wees et al. [6, 14] and Wharam et al. [7] independently observed the two-probe conductance of a QPC at sub-Kelvin temperature. In absence of applied magnetic field *i.e.* $B = 0$, they measured the conductance G as a function of the gate voltage V_g . Assuming the linear dependence of the width on V_g , they showed the conductance decreases with narrowing constriction. However, around this classical dependence, G changes in quantized steps of $\frac{2e^2}{h}$. These data exhibited conductance plateaus quantized in integer multiples of fundamental conductance $G_0 = \frac{2e^2}{h}$ as $G = NG_0$. Typically all these measurements were performed in a two-terminal configuration where voltage and current measured through the same set of source-drain contacts. The number N increases with the decrease in gate voltage *i.e.* as the gate-voltage is made less negative. As the gate voltage is made more negative, the potential in the narrow region of the QPC squeezes the 2DEG, pushing successive 1D sub-bands through the Fermi energy. As each 1D sub-band is depopulated, the conductance drops by an amount G_0 until finally all the sub-bands are completely depopulated and conductance approaches zero. The conductance quantization is

not as exact as the Hall effect. A series resistance originating from the wide 2DEG regions has been subtracted [6] to line up the plateaus at their quantized values and the plateaus are not completely flat.

Integer and Fractional Quantum Hall Effect : ‘Hall measurement’ or measurement of conductivity in presence of weak magnetic field is useful for characterizing semiconducting thin films because both the electron density and mobility can be measured simultaneously. When a magnetic field (\vec{B}) is applied in perpendicular direction to the current (\vec{I}) through a rectangular conducting bar, the charge carriers experience a Lorentz force ($q\vec{v} \times \vec{B}$) in the perpendicular direction to both the current and applied magnetic field. These charge carriers are accumulated in the direction of force. As a result, an electric field is generated in the system. This effect is named after its discoverer as ‘Hall effect’. From Classical Drude model, the longitudinal resistance is independent of the applied magnetic field whereas the Hall resistance is a linear function of B . As long as the magnetic field is very low, this Drude model for ‘Hall effect’ is valid. At cryogenic temperatures ($\leq 4K$) for stronger magnetic fields, the longitudinal resistance shows oscillations in B and the Hall resistance exhibits plateau corresponding to the minima in longitudinal resistance. These features can be explained in terms of Landau levels which are purely quantum effect. Thus two-dimensional electron gas (2DEG) shows Quantum Hall effect (QHE) [5] when it is placed under a strong perpendicular magnetic field. QHE was discovered in 1980 by Klaus von Klitzing, Michael Pepper, and Gerhard Dorda. In an isolated 2DEG in Quantum Hall state, the Hall current is carried by the edge channels as all the bulk states are localized. These edge channels are free from backscattering because of chirality. The most striking feature of the QHE is the precise quantization of the Hall resistance. The plateaus are precisely quantized at integer and fractional multiples of $\frac{h}{e^2}$. The integer plateaus are known as the integer quantum Hall effect (IQHE). The precision of the IQHE is so accurate that it now forms the international standard of resistance. An important quantity in the quantum Hall regime is the filling factor which is defined as number of electrons divided by the flux quanta per magnetic field *i.e.* $\nu = \frac{hn_s}{eB}$. For filling factor $\nu = 1$, the system is in the center of the first plateau at h/e^2 , for $\nu = 2$, in the center of the second plateau at $h/2e^2$. and so forth. The filling factor is convenient for determining the electron density. The oscillations in the longitudinal resistance which have minima at the same magnetic fields where Hall resistance shows plateaus, are called the Shubnikov-de Hass oscillations. The temperature dependence of the oscillation minima is an accurate determination of the mobility and mean free path of the 2DEG. In 1982, Daniel Tsui and Horst Stormer discovered the FQHE. It refers to fractional plateaus *i.e.* $\nu = 1/3, 1/5$ etc.

Aharonov-Bohm oscillations in magnetoresistance : Aharonov and Bohm [10] first proposed an experiment to show that there exist effects of potentials on charged particles, even in the region where all the fields (electric or magnetic) vanish. This effect is named after Aharonov and Bohm. In Fig. 1.2 an experimental set-up, suited for verifying the prediction of Aharonov and Bohm, is given schematically. To see the interference pattern for the electron traversing the ring, the circumference of the ring should be smaller than the phase coherence length. One of the pioneering experiments in mesoscopic physics was performed by Washburn *et al.* [11] using a small ring, 820nm in diameter, etched out of a high quality gold film. They

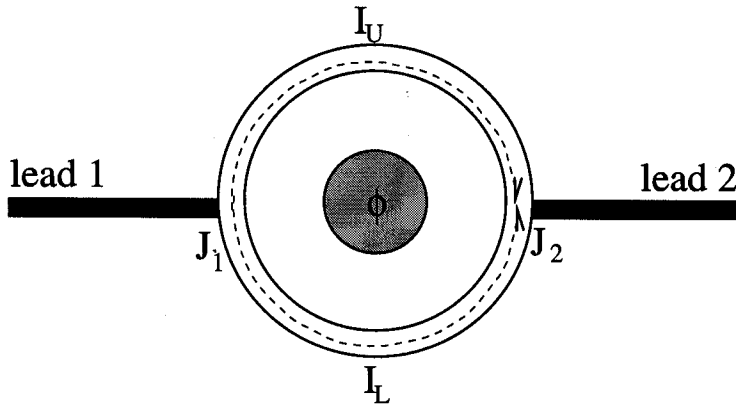


FIGURE 1.2: Schematic diagram of a circular loop connected to semi infinite leads. The conductor exhibits periodic oscillations in its conductance as a function of enclosed magnetic flux ϕ

observed that the conductance of the normal metal ring oscillates as a function of the magnetic flux enclosed by the ring. The fundamental period of the oscillations is found out to be the flux quantum $\Phi_0 = \frac{hc}{e}$. Classically no such oscillation can occur. This is because the quantum phase memory of the electron is not randomized during a travel around the whole circumference. A quantum wave associated to such an electron separates into two partial waves at the entrance of the ring and recombines at the exit point. These electron waves moving along fixed paths acquire a phase difference because of monotonically changing magnetic field. The interference between these two partial waves traversing two arms of the ring leads to this oscillatory behaviour of the conductance. In presence of the magnetic field \vec{B} using proper gauge for the vector potential in which the magnetic field appears only in the boundary conditions rather than explicitly in the Hamiltonian [15, 16], the transmission coefficient becomes $t_j(B) = t_j(0) \exp[i\frac{e}{\hbar} \int_j \vec{A} \cdot d\vec{l}]$, where \vec{A} is the vector potential defined by $\vec{B} = \vec{\nabla} \times \vec{A}$. Here j denotes the upper (say $j = 1$) or lower ($j = 2$) arms of the ring. While interfering the resultant transmission probability will be proportional to the phase difference between two transmission coefficients correspond to waves traversing two arms of the ring. Thus the probability of resultant transmission coefficient becomes $|T(B)| \sim \cos(\Delta\alpha)$, where the phase difference $\Delta\alpha = \frac{|e|}{\hbar} \oint \vec{A} \cdot d\vec{l} = \frac{|e|}{\hbar} \int_S \vec{B} \cdot d\vec{S} = \frac{2\pi\Phi}{\Phi_0}$, $\Phi_0 = \frac{hc}{e}$ is the quantum unit of flux. Conductance being proportional to transmission probability [Landauer formula] is also periodic in flux. This is known as ' ϕ_0 ' oscillation. Note that here we have not considered all possible paths while calculating transmission from a mode in lead 1 to another mode in lead 2. Depending on the nature of the 'beam-splitters' at J_1 and J_2 there will be more complicated paths such as one going through the upper arm, transmitting into the lower arm at J_2 , getting reflected back into the lower arm at J_1 and then exiting into lead 2 at J_2 . These paths would contribute to higher order oscillations that could be classified as $\frac{\phi_0}{N}$ oscillations, N being an integer. Experimentally the higher order effects are increasingly more difficult to observe because they involve longer paths and it is difficult to maintain phase coherence over the entire path. Another important point to note is that randomly distributed static non-magnetic impurities do not destroy phase coherence of electrons. So

the Aharonov-Bohm (AB-) effect holds in presence of these impurities.

Universal conductance fluctuations : At low temperatures quantum interference gives rise to fluctuations in conductance. In 1986, Washburn and Webb [17] measured the fluctuation in conductance of an Au wire as a function of applied magnetic field at 10mK. These fluctuations are not time dependent noise as they are completely reproducible. Supporting the earlier theory on conduction fluctuations [6] these data showed that the magnitude of fluctuation is of order $\frac{e^2}{h}$. These fluctuations are universal in nature because firstly the variance of conductance is of order $\left(\frac{e^2}{h}\right)^2$, independent of the sample size and the strength of the impurities and secondly this variance decreases precisely by a factor of two when time reversal symmetry is broken. This variance of conductance is weakly dependent on the shape of the conductor. At zero temperature, for a quantum wire the variance $\frac{\Delta G}{G_0} = \frac{2}{15}\beta^{-1}$. This is independent of the mean free path l_e , wire length L or the number of transverse modes N as long as the wire is much longer than the mean free path but much shorter than the localization length i.e. $l_e \ll L \ll Nl_e$. Various explanations came after the discovery of the universality of conductance fluctuations. Imry's argument was in terms of transmission eigenvalues [18]. Most transmission eigenvalues are exponentially small in a disordered conductor while a fraction $\frac{l_e}{L}$ of the total number N of transmission eigenvalues is of order unity. Depending on these transmission eigenvalues, the corresponding channels are referred as closed and open channels. Only the open channels contribute to the conductance: $\frac{G}{G_0} \equiv N_{open} \approx N \frac{l_e}{L}$. Thus the fluctuations in conductance can be interpreted as the fluctuations in number N_{open} of the open channels in the sample. If the transmission eigenvalues were uncorrelated, one would calculate that the fluctuations in N_{open} would have been of the order $\sqrt{N_{open}}$ which would imply the variance in conductance $\frac{\Delta G}{G_0}$ would be of order $N_{open}^{-1/2}$ ($>= 1$). Due to the strong suppression of fluctuations in N_{open} by eigenvalue repulsion the variance of conductance is of order unity.

Violation of Onsager's symmetry relation : The Onsager-Casimir relations was originally derived for macroscopic conductors using thermodynamic arguments. These are symmetry conditions for correlation functions. In electronic transport measurements, microscopic reversibility requires that in the presence of a magnetic field \vec{B} the conductance obeys $G_{ij}(B) = G_{ji}(-B)$ between contacts i and j . In particular, for a two-probe conductor the conductance is an even function of magnetic field $G(B) = G(-B)$. Such relations generally hold for macroscopic systems near thermodynamic equilibrium. Experimentally [19], there is no evidence that this relation is ever violated in the linear response regime regardless of the nature of the transport. When transport is phase coherent as it occurs in mesoscopic conductors, the conductance is not just material specific but also depends on the probe configuration. Four probe conductance of a sample is not symmetric under flux reversal i.e. $G_{ij,kl}(B) \neq G_{ij,kl}(-B)$. Herein, the first pair of indices represent the probes used to supply and draw current, while the last pair of indices denote the probes used to measure the potential difference. Though Onsager's symmetry relations fail in this regime but it holds Onsager's reciprocity relations. The reciprocity relations tell us the conductance of a mesoscopic sample is invariant under the magnetic field reversal accompanied by the exchange of voltage and current probes i.e. $G_{ij,kl}(B) = G_{kl,ij}(-B)$. This also prove that unlike bulk sample there is no material specific quantities like resistivity (or conductivity). Instead there are only global properties like resistance [20].

1.2 This Thesis

In this thesis, some novel low dimensional electronic transport problems are discussed. All through phase coherence is assumed as low temperature behaviours of mesoscopic conductors are dominated by phase coherence.

Chapter 2 describes some basic concepts and theoretical frameworks which will be extensively used throughout the thesis. Mesoscopic samples being finite the system-environment coupling often have strong effect on system properties. In section 2.2 we discuss this effect. In section 2.3 we introduce the generalized Landauer-Büttiker formula. The importance of scattering phase-shifts, Fano lineshapes etc. have been discussed in context of a couple of experiments in section 2.4. In sections 2.5, 2.6 and 2.7 we introduce the important concepts of tunneling phase time, persistent current and current magnification. In section 2.8 we discuss the framework of scattering matrix.

Chapter 3 addresses Friedel-Sum-Rule (FSR) which connects the experimentally measurable scattering phase shifts to the density of states (DOS) of a given system. We derive the canonical form of FSR in section 3.1.1. In section 3.2 we generalize FSR to incorporate the effect of system-environment coupling through a self-energy term. In following sections we show that the impact of this term is appreciable for a quasi-one dimensional (Q1D) quantum wire (in presence of elastic scattering) even in those energy regimes where transport occurs. We show this, in the energy regime where a single channel is propagating [21], in section 3.4. We digress a bit and show in section 3.3 that the impact of self energy term is negligible in higher energies for a truly one dimensional wire. We return to multi-channel transport in Q1D wire in section 3.5.1 and in section 3.5.2 we prove the non-negligible effect of self-energy in FSR for transport through multi-channel Q1D quantum wires [22], in general. We generally observe the Fano lineshapes in various transmission amplitudes for multi-channel quantum transport eg. in section 3.5.1. We discuss Fano resonance for a simple model system [23] in section 3.6 to obtain better understanding of the underlying phenomenon. In the appendix of this chapter except for the other derivations required in its main body we present the mode rescaling technique for a singular potential in a multi-moded Q1D system. This will, in general, be required for calculations of any such Q1D transport properties eg. current magnification in chapter 4.

Chapter 4 discusses a novel effect called quantum ‘current magnification’ in a Q1D quantum ring [24] in presence of time invariant biasing. This effect was earlier predicted for purely one dimensional quantum wires. We have shown that the effect persists for multi-channel wires despite mode mixing (at scatterer sites) and cancellations. We systematically study the effects of ring-lead coupling, scattering potential strength, quasi-bounded states and Fano resonances. In section 4.2 we discuss about the possible experiments which can verify our predictions.

In chapter 5 we have described ‘phase time’ which is one of the well-accepted ‘tunneling times’ in the community. For opaque barrier, the ‘phase time’ shows saturation as the length of the barrier, known as ‘Hartman effect’. In section 5.2 we have studied this effect even in presence of embedded Aharonov-Bohm (AB) flux in two different ring geometries. In section 5.2.1 and section 5.2.2 we have focused on the transmission and reflection phase times respectively for a ring connected with two external leads [25] and a single lead [26]. We have

seen the effect of different system parameters eg. the strength of the barrier, flux etc. on the saturation phase times. In section 5.3 we have considered another geometry, a quantum network [27] consisting of several side branches attached to a base arm, to study ‘Hartman effect’. In addition to this effect, we have studied the saturation phase time through a barrier in one arm varying nonlocal parameters eg. strength of the barrier in other arm, shifting this barrier from the junction etc.

Finally we draw overall conclusions in chapter 6.

Chapter 2

Basics of electron transport in mesoscopic system

2.1 Introduction

Mesoscopic conductors having dimensions less than the phase coherence length of the electrons can be treated as phase coherent scatterers and all their conductance related features and thermodynamic properties can be studied through underlying scattering phenomena. At sufficiently low temperatures, only elastic scattering survives. In this chapter, we provide a brief overview of the basics of electronic transport through such phase coherent scatterers. In experiments on non-equilibrium electron transport through such a phase coherent conductor, it is connected to the environment (reservoir) through leads and due to small size of the conductor its physical properties get affected by the couplings at the conductor-lead interfaces. This will be discussed in the section 2.2. In section 2.3 we shall present the Landauer-Büttiker formula for calculating conductance from the scattering matrix elements. This is a key ingredient of transport studies. The conductance is proportional to the available density of states (DOS), the measure of the occupied energy states by the electrons in the system. This DOS can be obtained from experimentally measurable scattering phase-shifts. In section 2.4 we shall describe an experiment on phase measurement in a quantum dot by R. Schuster et al. The measurement of phase-shift is connected to another crucial concept in scattering, the ‘phase time’, which is a measure of the time spent by a quasi-monochromatic wave in a scatterer region. In section 2.5 we discuss the concept of ‘phase time’ in the context of tunneling particles. ‘Persistent current’ is one of the experimentally observed thermodynamic properties which can be studied using the scattering properties of the system, we shall describe the effect briefly in the section 2.6. In the last section 2.8 of this chapter we shall discuss the formulation of scattering matrix in context of elastic scattering in a typical quasi-one-dimensional (Q1D) mesoscopic conductor.

2.2 Effect of environment on mesoscopic conductor

Conductance by a mesoscopic system must be considered in the presence of an environment provided, for instance, by the leads. The very fact that the system is mesoscopic implies some

subtleties in the description of the underlying process. In statistical mechanics of thermodynamically large systems, the probability distribution for the Grand Canonical Ensemble can be derived from that of the Canonical Ensemble by hypothetically decomposing the full domain of constant (N, V, T) system into a grand canonical system and an environment. The total Hamiltonian $H(p, q, N)$ of the canonical system with N particles of coordinates and momenta (q, p) can be decomposed as [28],

$$H(p, q, N) = H_c(p_1, q_1, N_1) + H_l(p_2, q_2, N_2), \quad (2.1)$$

where $H_c(p_1, q_1, N_1)$ is Hamiltonian of the grand canonical system with N_1 particles in presence of the environment consisting of N_2 ($N_2 \gg N_1$) particles having Hamiltonian $H_l(p_2, q_2, N_2)$. While decomposing in the above fashion, the interactions between particles in the system in contact with the environment at the interfaces have been neglected. This is plausible if the system size is thermodynamically large. For a finite sized system, instead, the interface effect is not negligible and hence the probability distribution of this truncated part, called system, has to be in addition a function of the interfacial energy.

In mesoscopic systems, having dimensions of the order of few hundred nanometers, the effect of environment is important. In this case one needs to incorporate the ‘interaction’ between the system and the environment to obtain correct physical properties. In what follows we show how this conductor-lead (system-environment) interaction is taken into account in mesoscopic transport problems. The ‘density of states (DOS)’ play a crucial role in all of quantum statistical physics. In particular it is required to calculate conductance, a central quantity in all quantum transports. The DOS of an isolated conductor can be expressed in terms of its retarded (advanced) Green’s function

$$\begin{aligned} \hat{G}_c^{r(a)} &= \left[(E \pm i\epsilon) \hat{\mathbb{I}} - \hat{H}_c \right]^{-1} \\ &= \left[\mathbb{P} \left(\frac{1}{E \hat{\mathbb{I}} - \hat{H}_c} \right) \mp i \pi \delta(E \hat{\mathbb{I}} - \hat{H}_c) \right], \end{aligned} \quad (2.2)$$

where \mathbb{P} denotes the principal part in the sense of integration on complex plane. The DOS is defined as $\rho = \sum_i \delta(E - E_i) = Tr \left[\delta(E \hat{\mathbb{I}} - \hat{H}_c) \right]$. Hence the above expression yields

$$\rho = \mp \frac{1}{\pi} Im \left[Tr \left(\hat{G}_c^{r(a)} \right) \right]. \quad (2.3)$$

This ensures that any change in Green’s function affects the DOS. Now we show how the Green’s function of an ‘open conductor’ (conductor in contact with the environment) is affected in presence of interactions with the reservoirs through the leads. The retarded Green’s function for a conductor-lead composite system can be written as,

$$\hat{G}^r = \left[(E + i\epsilon) \hat{\mathbb{I}} - \hat{H}_{\text{tot}} \right]^{-1} \quad (2.4)$$

which is infinite dimensional because the total system of conductor plus lead stretch out to infinity. H_{tot} is the Hamiltonian for conductor-lead composite system. In the same spirit as

in statistical mechanical case discussed above, we can partition the overall Green's function of Eq. (2.4) into submatrices [5]

$$\begin{bmatrix} \hat{G}_l^r & \hat{G}_{lo}^r \\ \hat{G}_{ol}^r & \hat{G}_o^r \end{bmatrix} = \begin{bmatrix} (E + i\epsilon)\hat{\mathbb{I}} - \hat{H}_l & \hat{\tau}_l \\ \hat{\tau}_l^+ & E\hat{\mathbb{I}} - \hat{H}_c \end{bmatrix}^{-1} \quad (2.5)$$

where the operator $(E + i\epsilon)\hat{\mathbb{I}} - \hat{H}_l$ represents the isolated lead, while $E\hat{\mathbb{I}} - \hat{H}_c$ represents the isolated conductor. $\hat{\tau}_l$ gives the coupling between the conductor and the lead. This allows us to avoid calculation of infinite dimensional \hat{G}^r and reduces the problem to the conductor's (open) Green's function \hat{G}_o^r . From Eq. (2.5), using the matrix identity, *i.e.*

$$\begin{bmatrix} \hat{G}_l^r & \hat{G}_{lo}^r \\ \hat{G}_{ol}^r & \hat{G}_o^r \end{bmatrix}^{-1} \begin{bmatrix} \hat{G}_l^r & \hat{G}_{lo}^r \\ \hat{G}_{ol}^r & \hat{G}_o^r \end{bmatrix} = \begin{bmatrix} \hat{\mathbb{I}} & \hat{\mathcal{O}} \\ \hat{\mathcal{O}} & \hat{\mathbb{I}} \end{bmatrix}, \quad (2.6)$$

we obtain the explicit expression for \hat{G}_o^r in terms of the Green's function of the isolated lead and conductor-lead coupling as,

$$\hat{G}_o^r = \left[E\hat{\mathbb{I}} - \hat{H}_c - \hat{\Sigma}^r \right]^{-1}, \quad (2.7)$$

with $\hat{\Sigma}^r = \hat{\tau}_l^+ \hat{g}_l^r \hat{\tau}_l$, called the (retarded) 'self-energy'. Here $\hat{g}_l^r = \left[(E + i\epsilon)\hat{\mathbb{I}} - \hat{H}_l \right]^{-1}$ is the Green's function for the isolated lead. Thus the 'self-energy' $\hat{\Sigma}^r$ provides the effect of environment in the conductor's Green's function \hat{G}_o^r of a finite sized conductor. Similarly, the advanced Green's function \hat{G}_o^a depends on the advanced self-energy $\hat{\Sigma}^a (= \hat{\Sigma}^{r\dagger})$ through the relation,

$$\hat{G}_o^a = \left[E\hat{\mathbb{I}} - \hat{H}_c - \hat{\Sigma}^a \right]^{-1}, \quad (2.8)$$

where $\Sigma^a = \hat{\tau}_l^+ \hat{g}_l^a \hat{\tau}_l$. Now the DOS being a function of the system's Green's function (as we see from Eq. (2.3)), it also gets affected in presence of the environment and it becomes

$$\rho = (1/\pi) \text{Im} \left[\text{Tr} (\hat{G}_o^a) \right], \quad (2.9)$$

in the conductor, which is the region of interest, thereby affecting all the conductance properties. In Chapter 3 we shall describe in details the effect of environment on DOS and the related consequences in the context of the Friedel-sum-rule.

2.3 Landauer-Büttiker conductance formula:

Landauer-Büttiker (LB) scattering theory provides a powerful approach to multi-terminal transport in conventional (Fermi-liquid) mesoscopic devices where leads are explicitly accounted for. The effect of environment comes into picture through the attached leads. In contrast to the Kubo formalism which is time-dependent, the Landauer formula connects the conductance of a mesoscopic system to its static scattering properties. Landauer in his pioneering work [29] expressed the current through a conductor in terms of the probability that

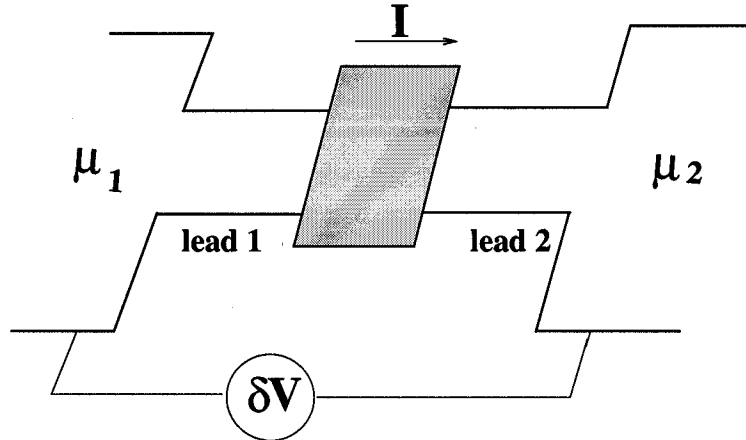


FIGURE 2.1: Mesoscopic sample (shaded region) connected to two electron reservoirs, characterized by chemical potential μ_1 and μ_2 respectively, by ideal leads (lead1 and lead2). A voltage difference $\delta V = (\mu_1 - \mu_2)/e$ between the reservoirs causes a current I through the sample.

an electron can transmit through it. Thus the electrical conduction of a device is reduced to a scattering problem. This approach is intuitively very appealing because it seems obvious that the conductance of a sample ought to be proportional to the ease with which electrons can transmit through it. For ballistic conductor, the transmission probability being unity, the finite current obtained from Landauer approach gave rise to a question 'where does this resistance come from?' Imry [30] clarified this question using earlier notions due to Engquist and Anderson. Büttiker [8] extended this approach to describe multi-terminal measurements in presence of magnetic field.

In Chapter 4 for a Quasi-one-dimensional (two dimensional system with width much less than its length) quantum ring geometry (the ring shaped system having mesoscopic length scale, where wave properties of electrons become important) in contact with electron-reservoirs via leads, we use Landauer-Büttiker conductance formula to calculate the electronic current in different segments of the system.

2.3.1 General Landauer formula

To derive the Landauer conductance formula, we consider a mesoscopic conductor at zero temperature connected to two electron reservoirs by ideal leads as shown in Fig. 2.1. The left and right reservoirs are characterized by chemical potentials μ_1 and μ_2 respectively. The 'conductor' is represented as a scattering region. The current is seen as a consequence of the imbalance of chemical potential at the external reservoirs. When μ_1 is greater than μ_2 a current starts flowing through the system from left to right. The current flow takes place entirely in the energy range between μ_1 and μ_2 . The contacts are assumed to be 'reflectionless' *i.e.* electrons can exit the device into the contacts without any reflection. In a narrow conductor due to confinement in transverse direction, several modes or channels are present. Only the propagating modes *i.e.* $k_x^2 \geq 0$ participate in conductance. The dispersion

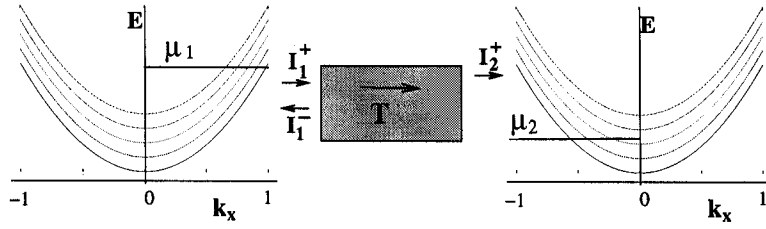


FIGURE 2.2: Dispersion relations for several transverse modes. Just for clarity we have drawn only five modes. The electrons that constitute the net current have energies ranging in between μ_1 and μ_2 .

curves for each mode has a cut-off energy

$$\epsilon_n = E(n, k = 0).$$

For a given energy E of the system the number of propagating modes can be obtained by counting the number of modes having cut-off energy smaller than E :

$$N \equiv \sum_n \Theta(E - \epsilon_n)$$

For simplicity we consider equal number of transverse modes ' N ' are present in both leads *i.e.* leads are of equal width. Since $\mu_1 > \mu_2$, carriers are injected into the left lead from the left reservoir. The incoming current (see Fig. 2.2) carried by channel i is

$$I_i^{in} = e v_i \frac{\partial n_i}{\partial E} (\mu_1 - \mu_2) \quad (2.10)$$

where v_i is the longitudinal velocity along x -direction and the density of states in the leads for the i -th mode is

$$\frac{\partial n_i}{\partial E} = \frac{\partial n_i}{\partial k_i} \frac{\partial k_i}{\partial E} = \frac{1}{2\pi} \frac{1}{\hbar v_i}.$$

Apart from this there will be another term, originating from the oscillatory local density of states (LDOS) in the leads, which has been ignored to derive Landauer conductance formula. Though in quantum regime, the oscillatory LDOS can be very large yet predictions of Landauer conductance formula has been observed to an accuracy of one part in a billion. Therefore, it is suitable to assume that the reservoirs screen away the oscillatory LDOS and it has no effect on transport properties or thermodynamic properties of the mesoscopic sample. Both v_i and $\frac{\partial n_i}{\partial E}$ are evaluated at the Fermi energy. Using these two relations in Eq. (2.10) we find that

$$I_i^{in} = \frac{e}{2\pi\hbar} (\mu_1 - \mu_2) \quad (2.11)$$

which is same for all the propagating modes (channels) present in the system. Thus the total influx of current from lead 1 is given by

$$I_i^{in} = \frac{e}{2\pi\hbar} N (\mu_1 - \mu_2) \quad (2.12)$$

The outflux from lead 2 is simply the influx at lead 1 times the transmission probability

$$I^{out} = \frac{e}{2\pi\hbar} N \sum_{i,j=1}^N T_{ij} (\mu_1 - \mu_2), \quad (2.13)$$

where T_{ij} denotes transmission coefficient from mode j in the left lead into the mode i of the right lead. The rest of the flux is reflected back to left reservoir

$$I^- = \frac{e}{2\pi\hbar} N (\mu_1 - \mu_2) \left(1 - \sum_{i,j=1}^N T_{ij}\right).$$

Thus the net current I flowing at any point in the conductor is given by

$$I = I^{in} - I^- = I^{out} = \frac{e}{2\pi\hbar} N \sum_{i,j=1}^N T_{ij} (\mu_1 - \mu_2) \quad (2.14)$$

Hence the conductance is equal to the net current divided by the proper voltage difference ΔV . When two non-invasive voltage probes (*i.e.* there is no (finite) current flowing through the probes) are attached at the reservoirs $\Delta V = (\mu_1 - \mu_2)/|e|$ and thus

$$G = \frac{I}{\Delta V} = \frac{2e^2}{h} N \sum_{i,j=1}^N T_{ij} \quad (2.15)$$

which is the celebrated 'Landauer two probe conductance formula'.

When these voltage probes are attached to the leads adjacent to the conductor the potential difference is determined by the piled up charges to the left and to the right of the conductor represented by the chemical potentials μ_A and μ_B respectively. μ_A and μ_B are smaller than μ_1 and larger than μ_2 . μ_A (μ_B) is found from the condition that the number of occupied states (electrons) above μ_A (μ_B) must equal the number of unoccupied states (holes) below μ_A (μ_B). Then potential difference is

$$\Delta V = \frac{\mu_A - \mu_B}{|e|} = \frac{\sum_i [1 + \sum_j (R_{ij} - T_{ij})] / v_i}{\sum_i 2/v_i} (\mu_1 - \mu_2).$$

Thus we obtain the conductance as

$$G_4 = \frac{2e^2}{h} \sum_{i,j} T_{ij} \frac{\sum_n 2/v_n}{\sum_n [1 + \sum_m (R_{nm} - T_{nm})] / v_n}. \quad (2.16)$$

Since the voltage probes do not coincide with the reservoirs (current probe), hence Eq. (2.16) is called four probe conductance formula.

For decoupled channels $T_{ij} = \delta_{ij} T_j$ and $R_{ij} = \delta_{ij} R_j$ and for each channel j , $T_j + R_j = 1$. Then the Landauer two probe and four probe conductance formulas *i.e.* Eq. (2.15) and Eq. (2.16) reduce to

$$G = \frac{2e^2}{h} N \sum_{j=1}^N T_j \quad (2.17)$$

$$G_4 = \frac{2e^2}{h} \sum_j T_j \frac{\sum_n 2/v_n}{\sum_n [1 + (R_n - T_n)] / v_n}. \quad (2.18)$$

For single channel case these equations are simplified to

$$G = \frac{2e^2}{h} T_1 \quad (2.19)$$

$$G_4 = \frac{2e^2}{h} \frac{T_1}{1 - T_1}. \quad (2.20)$$

One can view the total resistance G^{-1} as a reservoir-lead contact resistance G_c^{-1} in series with the conductor resistance G_4^{-1} . When transmission vanishes, *e.g.* for tunneling systems, G and G_4 converge to one another. When transmission is close to unity ($T_1 \rightarrow 1$), the resistance $G_4^{-1} \propto R_1$, *i.e.* the resistance is proportional to the back-scattering probability.

2.3.2 Büttiker solution

The difference in points of view expressed by Eq. (2.15) or Eq. (2.16) for the conductance has its roots in the location of the non-invasive voltage probes. Büttiker treated [8] the current probes and voltage probes on equal footing. He made no qualitative distinction between current and voltage leads. The advantage of this approach is that the inherent invasive property of the probes is taken into account in a natural way. He then evaluated the current flowing from one reservoir to another *i.e.* Eq. (2.13) for the difference in chemical potentials inside two reservoirs *i.e.* μ_1 and μ_2 . He argued that the current in Eq. (2.13) arose due to the difference of the chemical potentials inside the reservoir.

In his approach [8], each probe connected to the conductor by leads is considered as a carrier emitting reservoir held at some chemical potential. If we have a total of l_P probes, the current through lead l_i connected from the conductor to probe l_i (current/voltage probe) is then given by

$$I_{l_i} = \sum_{l_j=1}^{l_P} G_{l_i, l_j} \mu_{l_j}, \quad (2.21)$$

with μ_{l_j} is the chemical potential of probe l_j and

$$G_{l_i, l_j} = \frac{2e^2}{h} N \sum_{i, j=1}^N T_{ij}^{l_i l_j} \quad (2.22)$$

is the two-probe Landauer conductance due to the transport from probe l_j to probe l_i via lead l_j to lead l_i through the conductor. Here $T_{ij}^{l_i l_j}$ denotes the transmission coefficient from mode i in lead l_i to mode j at probe l_j .

2.4 Experiment on phase-shift:

Yacoby et al. [31] and Schuster et al. [32] had performed two interference experiments on the phase coherent transmission through quantum dots (QD) in the Coulomb blockade regime. Both the experiments utilized the double-slit interference procedure to measure the phase shift of an electron while traversing the QD. To introduce measurable phase shift between

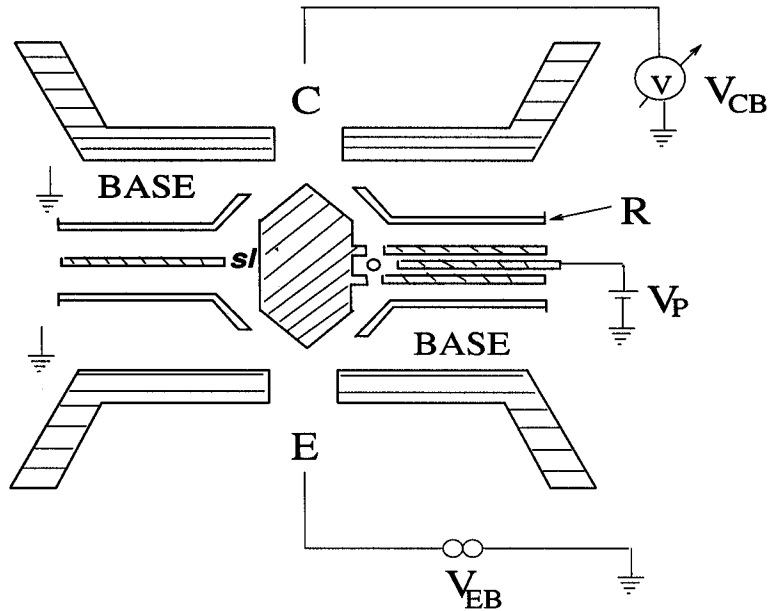


FIGURE 2.3: Schematic description of the device structure used by Schuster et al. An AB-ring is connected to an emitter E, a collector C and base region. Reflector gates R reflect diverging electrons towards the collector. \bullet is the QD. Taken from Ref. [32].

arms of the Aharonov-Bohm (AB-) interferometer they inserted the QD in one of the arms. In the former experiment [31], a two-probe measurement was done. In this measurement, due to Onsager symmetries, the phase of the AB-oscillations were restricted to either 0 or π , thus this experiment could not provide the required phase-shift. Schuster et al. [32] overcame this drawback by using four-probe measurement. Their device, schematically shown in Fig. 2.3, was defined by metallic gates on the top of a GaAs-AlGaAs heterostructure. Different contacts, namely, the emitter (E), the collector (C) and the base region and additional reflecting barriers (R) are connected with the ring. The base contacts were held at zero chemical potential. Another gate (the plunger gate V_P) controlled the area and electrostatic potential at the QD. Using Landauer-Büttiker's four-probe conductance formula, Schuster et al. measured the current at the collector as

$$I_C = \frac{2e^2}{h} [T_{EC} V_{EB} \pm T_C V_{CB}],$$

where T_C is the transmission probability through C. The transmission probability $T_{EC} = |t_{QD} + t_{sl}|^2$ is a coherent sum of all path amplitudes from E to C. Here t_{QD} and t_{sl} are the transmission coefficients from E to C respectively through the path containing the QD and the path without it (represented as 'sl' in the Fig. 2.3). The open circuit ($I_C = 0$) collector voltage V_{CB} ($= \frac{V_{EB}}{T_C} T_{EC}$) is proportional to T_{EC} . They investigated the voltage drop V_{CB} for fixed voltage V_{EB} between the emitter E and the base. For fixed magnetic field they observed pronounced resonance peaks (peaks in V_{CB}) and minima as a function of the plunger gate voltage V_P in the Coulomb blockade regime. The phase of the AB signal V_{CB} showed

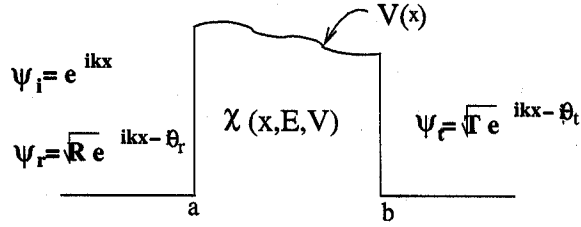


FIGURE 2.4: Schematic diagram of a one dimensional scatterer of arbitrary shape with strength $V(x)$. The barrier is confined in the interval $a \leq x \leq b$. ψ_i , ψ_r and ψ_t are respectively the incident, reflected and transmitted waves. $\chi(x, E, V)$ is the evanescent wave inside the barrier region.

monotonic rise to π over the width of the resonance and jumps to zero at the minima over a very small energy scale. The resonance-zero line-shape in the conductance as a function of Fermi-energy and the phase behaviour described above have been assigned to Fano resonance at energies where the scattering state of non-resonant free path gets degenerate with resonant state of the path containing the QD[124]. This ‘Fano’ resonance which is characterized by zero-pole structure in complex energy is a very general feature of conductance in quasi-one-dimensional (Q1D) conductors. This would be clearly seen as we proceed for the next two chapters. In the appendix of Chapter 3 we shall study ‘Fano resonance’ in details. On the other hand, in the Schuster et al.’s experiment, when the magnetic field is changed the collector voltage shows AB oscillations with the expected period $\Delta B = \phi_0/A$ where A is the area of the AB-ring and ϕ_0 is the flux quanta.

2.5 Phase time for tunneling particle

The ‘phase time’ or ‘delay time’ is defined as the energy derivative of scattering phase-shift and is interpreted as the time spent by the particle (electron) in the scattering region. This was proposed by Wigner in 1955 [33] and is often called ‘Wigner delay time’. We consider an one-dimensional time-independent barrier $V(x)$ localized on the interval $a \leq x \leq b$ as in Fig. 2.4. Let a wave packet with wave vectors distributed sharply around k (quasi-monochromatic) is incident on the scatterer and it has the form

$$\psi_i = \int f(k) \exp(ikx - iEt/\hbar) dk, \quad (2.23)$$

where E is the energy of the electron with wave vector k . After scattering, the transmitted wave packet can be represented as

$$\begin{aligned} \psi_t &= \int t(k) f(k) \exp(ikx - iEt/\hbar) dk \\ &= \int \sqrt{T} \exp(i\theta_t + ikx - iEt/\hbar) dk, \end{aligned} \quad (2.24)$$

where $T (= t^* t)$ is transmission amplitude and θ_t is the phase of the transmission coefficient t . Let $x = x_p$ be the peak of the wavepacket. In stationary phase approximation,

$$\frac{d\theta_t}{dk} + x_p(t) - \frac{1}{\hbar} \frac{dE}{dk} t = 0. \quad (2.25)$$

Thus due to tunneling through the barrier a spatial displacement $\delta x (= \frac{d\theta_t}{dk})$ occurs in the peak of the transmitted wave. The corresponding temporal delay is

$$\begin{aligned} \tau_t &= \frac{1}{v(k)} \frac{d\theta_t}{dk} \\ &= \hbar \frac{d\theta_t}{dE}, \end{aligned} \quad (2.26)$$

where $v(k)$ is the group velocity of the free wave packet. In what follows this temporal delay in transmission will be referred to as ‘transmission phase time’. Similarly, the ‘reflection phase time’ is defined as the energy derivative of the reflection phase, $\tau_r = \hbar \frac{d\theta_r}{dE}$. It would be worth mentioning that for a symmetric barrier the reflection and transmission phase times are equal. The tunneling through an 1D static barrier, as shown in Fig. 2.4, conserves time-reversal symmetry and hence the scattering matrix S can be written as

$$S = \begin{pmatrix} r & t \\ t & r' \end{pmatrix}, \quad (2.27)$$

where r and r' are reflection amplitudes for particle (electron) coming from the left and from the right, respectively. The unitarity of scattering matrix ($S^\dagger S = I$) implies that $|t|^2 + |r|^2 = |t|^2 + |r'|^2 = 1$ (probability conservation) and $t^* r' + t r^* = 0$. From the former relation we get $|r| = |r'|$ and then substituting it in the later, we obtain a relation between the phases of the reflection and transmission amplitudes as

$$\theta_t + \frac{\pi}{2} = \frac{1}{2} (\theta_r + \theta_r'), \quad (2.28)$$

where θ_r' is the phase corresponding to reflection amplitude r' . For a symmetric barrier, $\theta_r = \theta_r'$ (as $r = r'$), then Eq. (2.28) becomes

$$\theta_t + \frac{\pi}{2} = \theta_r. \quad (2.29)$$

Thus for a symmetric barrier $\tau_r = \tau_t$.

In chapter 5 we shall discuss the phase time in details for tunneling through different quantum systems and verify Hartman effect, independence of phase time on the width of an opaque barrier for tunneling particles, beyond one dimension.

2.6 Persistent Current

It is well-known that persistent current can flow in super-conducting systems in absence of magnetic flux. Büttiker, Imry and Landauer [34] in a seminal paper, suggested the existence

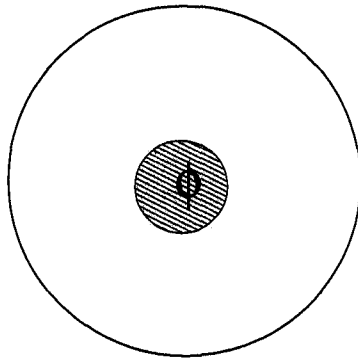


FIGURE 2.5: Schematic diagram of a closed circular loop with an enclosed Aharonov-Bohm flux ϕ .

of persistent currents even in a normal metal closed loop (e.g. ring) but in the presence of Aharonov-Bohm (AB)-flux. The persistent current is an equilibrium property of the ring and is given by the flux derivative of the Free Energy of the ring. These currents are the consequence of the sensitivity of the eigen-states to the boundary condition. Due to the enclosed magnetic field, the time reversal symmetry in the ring system is broken. As a consequence, the degeneracy between the states carrying current in clockwise and anti-clockwise directions is lifted. For a perfect one-dimensional ring of circumference L (see Fig. 2.5), the periodic boundary conditions lead to the quantization of energy levels, namely, $E_n = \frac{\hbar^2}{2m} \left(\frac{2\pi n}{L}\right)^2$, where, $n = 0, \pm 1, \pm 2, \dots$. Thus we see, the ground state $n = 0$ is non-degenerate and each of the excited states are doubly degenerate. In presence of AB-flux, the degeneracy of these levels is lifted. The modified periodic boundary condition of the wave-function in presence of AB-flux is $\psi(x + L) = \psi(x) \exp(i2\pi\phi/\phi_0)$, where ϕ_0 is the flux quantum. As a result the eigen-states and eigen-energies and hence all the equilibrium physical properties of the ring are periodic in AB-flux ϕ with a period ϕ_0 . Again, in general, $\psi(x + L) = \psi(x) \exp(ikL)$ for Bloch-like states. This condition implies the identification

$$kL = 2n\pi + \frac{2\pi\phi}{\phi_0} \quad (2.30)$$

The current carried by n -th single-particle level in the ring at $T = 0$ is,

$$I_n = -\frac{ev_n}{L}, \quad v_n = \frac{1}{\hbar} \frac{\partial E_n}{\partial k_n} \quad (2.31)$$

which gives, using the analogy in Eq. (2.30),

$$I_n = -c \frac{\partial E_n}{\partial \phi} = -\frac{eh}{mL^2} \left(n + \frac{\phi}{\phi_0} \right) \quad (2.32)$$

where, energy eigenvalues

$$E_n = \frac{\hbar^2}{2m} \left[\frac{2\pi}{L} \left(n + \frac{\phi}{\phi_0} \right) \right]^2, \quad (2.33)$$

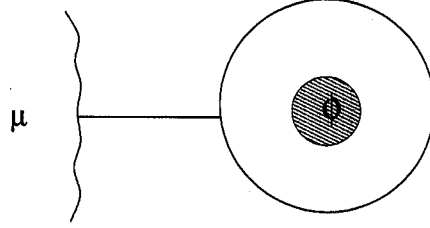


FIGURE 2.6: Schematic diagram of a circular loop connected to a reservoir of chemical potential μ by a lead. An Aharonov-Bohm flux ϕ is enclosed in the ring.

with $n = 0, \pm 1, \pm 2, \dots$. Thus one can readily see from Eq. (2.32) that for the ground state, the current is diamagnetic in nature and for the 1st excited state ($n = -1$) it is paramagnetic. As we go from one energy eigenstate to next the current changes sign. This is related to the ‘parity effect’[125]. The total current in the ring for N number of spinless electrons is the sum over the individual contribution from each state, weighted with the appropriate occupation number. At finite temperature, instead of the sum, one can calculate the current from the thermodynamic potential *i.e.* Free Energy F of the system [35],

$$I(\phi) = -c \frac{\partial F}{\partial \phi}. \quad (2.34)$$

This is the persistent current flowing in a closed 1D ring at equilibrium. As a grand canonical realization of the system one can couple it with a Landauer reservoir (see Fig. 2.6) of chemical potential μ by a lead. The persistent current of such open system is given by [36]

$$I(\mu) = -c \int_{E_s}^{\mu} \frac{\partial}{\partial \phi} \frac{1}{2i} \log \text{Det} [S(E)] dE, \quad (2.35)$$

where, E_s is the bottom of the conductance band. The integrand gives the differential current

$$\begin{aligned} \frac{dI}{dE} &= -\frac{\partial}{\partial \phi} \frac{1}{2i} \log \text{Det} [S(E)] \\ &= -\frac{\partial \eta}{\partial E} \frac{\partial E}{\partial \phi}, \end{aligned} \quad (2.36)$$

where $\eta = \frac{1}{2i} \log \text{Det} [S(E)]$ is the scattering phase shift and $\frac{\partial \eta}{\partial E}$ approximately gives the relevant density of states (DOS). Thus the differential current for an open ring at finite temperature is the closed ring persistent current times the DOS. Persistent currents in mesoscopic rings have been detected in several experiments [37, 38]. The typical magnitude of persistent current at $T = 0$ with L between 1 and 3 μm and for a Fermi wavevector k_f between 10^{10}m^{-1} (metallic rings) and 10^8m^{-1} (semiconducting rings), varies between 1 and $5nA$. However, there is a discrepancy of upto two orders of magnitude between experimental and theoretical results.

2.7 Current magnification

Persistent current in isolated (closed) rings are generated in presence of embedded AB-flux and it is an equilibrium phenomenon. Whereas, in open system (*eg.* ring connected with electron-reservoirs) without having any threaded AB-flux, the circulating current arises in presence of inter-reservoirs transport current. This is a non-equilibrium phenomenon. Unlike the persistent current which is due to the broken time reversal symmetry in presence of AB-flux, the circulating current generates when the two arms of the ring are asymmetric. The current I injected by the reservoir into one of the leads splits into I_U and I_L in the upper and the lower arms of the ring (see Fig. 2.7) such that the total current is conserved (Kirchoff's law : $I = I_U + I_L$). When the two arms are identical in all respects then the injected current is divided exactly into two equal halves *i.e.* $I_U = I_L = I/2$ while flowing in the ring before combining at other junction with the lead. Here I gives the total inter-reservoir current or the transport current. For classical ring when the two arms are not identical then we have the condition $I_U/I_L = R_U/R_L$ and $I = I_U + I_L$, which automatically implies $0 < I_U < I$ and $0 < I_L < I$. Here R_U and R_L are the resistances of the two arms of the ring. Thus both I_U and I_L are positive and flow along the applied bias. But for mesoscopic ring, the circumference being smaller than the phase coherence length, the electrons in two arms in general pick up different phases and their quantum mechanical superposition gives rise to two distinct possibilities. The first being, for some values of Fermi energy the currents in the two arms I_U and I_L are individually less than the total current I , *i.e.*, the current in both arms flow along the direction of the applied field. The other possibility is that for some values of Fermi energy, I_U (or I_L) can be greater than the total current I . In this case current conservation dictates I_L (or I_U) to be negative such that $I = I_L + I_U$. The phenomenon that the current in one of the arms is larger than the transport current is referred to as '**current magnification**' [39–41]. This has been already established theoretically for 1D ring system. Such a phenomenon occurs at the vicinity of resonances in the ring and is purely quantum mechanical in origin. Magnitude of this negative current is that of the 'circulating current' associated with current magnification. This circulating current can lead to a large magnetic moment in absence of magnetic field but in presence of transport current. Classically, when a parallel resonant circuit (capacitance C connected in parallel with a series combination of inductance L and resistance R) is driven by an external e.m.f., circulating current arises in the circuit at resonant frequency [42]. However, the current magnification effect is absent in a circuit with two parallel resistors in the presence of dc current in the classical regime. In a mesoscopic ring the intrinsic wave nature of electrons and their phase coherence gives rise to this effect even in presence of dc driving voltage.

In Chapter 4 we shall investigate this phenomenon for a multi-channel Q1D mesoscopic ring with static impurities in it [24].

2.8 Scattering matrix for Q1D systems

When an electron scatters elastically from an impurity *eg.* potential barrier or well in free space, it scatters into a propagating wave (characterized by real wave-vector) which travels

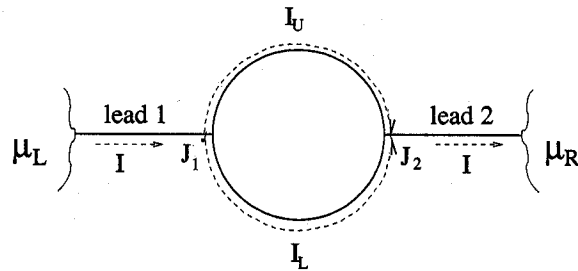


FIGURE 2.7: Schematic diagram of an open one dimensional mesoscopic ring connected with two reservoirs ϕ .

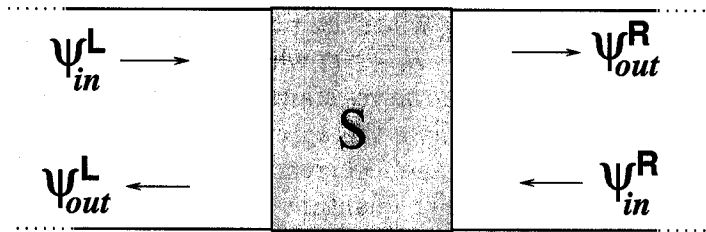


FIGURE 2.8: Mesoscopic sample connected to two semi-infinite leads of width W .

away from the impurity. But when an electron is restricted in the Q1D wire, several transverse (perpendicular to the direction of propagation) modes or sub-bands are formed due to the confinement. Depending upon the energy of the incident electron, among these transverse modes few are propagating and the rest are evanescent (not propagating; characterized by imaginary wave-vector). In such wire, the incident electron can, as well, elastically scatter into the evanescent modes present in the wire. Thus for a steady current flow, a localized state is formed even around a repulsive impurity[60]. Even for non-interacting electrons, the boundary conditions for scattering events change due to built up evanescent modes near the impurity. In Fig. 2.8, we have shown such a mesoscopic quasi-one-dimensional wire connected to two semi-infinite ideal leads. For simplicity we assume that both the leads and the sample are of same width W . We consider non-interacting spinless electrons that are described by the following Schrödinger equation

$$\left[-\frac{\hbar^2}{2m_e} \left(\frac{\partial^2}{\partial x^2} + \frac{\partial^2}{\partial y^2} \right) + V_c(y) + V_d(x, y) \right] \psi(x, y) = E\psi(x, y), \quad (2.37)$$

where the coordinates x and y represent the longitudinal and transverse directions respectively. The electrons are confined along the transverse (y)-direction but free to move along the longitudinal (x)-direction. m_e is the effective mass of the carrier (electron) in the system considered above. $V_c(y)$ is the confinement potential along the transverse direction, $V_d(x, y)$ is the potential due to impurities present in the wire. In the regions where no impurity

potential is present, one can solve an one-dimensional problem along the y-direction,

$$\left[-\frac{\hbar^2}{2m_e} \frac{\partial^2}{\partial y^2} + V_c(y) \right] \chi_n(y) = E_n \chi_n(y). \quad (2.38)$$

where n is the transverse mode index, E_n is the corresponding energy of the n -th transverse mode and $\chi_n(y)$ are the normal modes. One can expand the solutions of Eq. (3.63a) on the basis of $\chi_n(y)$ as

$$\psi(x, y) = \sum_n c_n(x) \chi_n(y), \quad (2.39)$$

where $c_n(x)$ are the Fourier coefficients. Along the transverse direction, the boundary conditions are such that the wavefunction vanishes outside the sample and the leads. This can be realized by considering a hard-wall type confinement potential

$$V_c(y) = \begin{cases} \infty & y \geq \left| \frac{W}{2} \right| \\ 0 & y < \left| \frac{W}{2} \right| \end{cases} \quad (2.40)$$

Then $\chi_n(y) \propto \sin\left(\frac{n\pi}{2} + k_y y\right)$ with $k_y = n\pi/W$ where $n = 1, 2, \dots, \infty$. depending on the incident energy $E = \hbar^2 k_x^2 + \hbar^2 k_y^2$ of the electron, finite number of modes are propagating ($k_x^2 \geq 0$), rest are evanescent ($k_x^2 < 0$). In Fig. 2.8, $\psi_{in}^L, \psi_{out}^L$ represent respectively the incoming wave towards the sample (scatterer) and outgoing wave from the sample in the left lead and $\psi_{in}^R, \psi_{out}^R$ represent the same in the right lead. Inside the sample and the leads, every solution of Eq. (3.63a) can be written as a sum of incoming and outgoing 'propagating' waves as well as 'evanescent' waves. Far away from the impurity 'evanescent' wave plays no role and thus,

$$\psi(x, y) = \sum_{n=1}^P [A_n^L \psi_{in_n}^L + B_n^L \psi_{out_n}^L] \text{ for } x \rightarrow -\infty \quad (2.41)$$

$$\psi(x, y) = \sum_{n=1}^P [A_n^R \psi_{in_n}^R + B_n^R \psi_{out_n}^R] \text{ for } x \rightarrow +\infty, \quad (2.42)$$

where $\psi_{in_n}^L$ and $\psi_{out_n}^L$ constitute $c_n(x) \chi_n(y)$ in the left lead and $\psi_{in_n}^R$ and $\psi_{out_n}^R$ constitute $c_n(x) \chi_n(y)$ in the right lead. P represents the maximum number of propagating modes. The coefficients of incoming and outgoing coefficients are related by a linear transformation,

$$\begin{pmatrix} B^L \\ B^R \end{pmatrix} = S(E) \begin{pmatrix} A^L \\ A^R \end{pmatrix}, \quad (2.43)$$

where A^L, A^R, B^L, B^R , are the column vector of the coefficients $A_n^L, A_n^R, B_n^L, B_n^R$ respectively and $S(E)$ is the scattering matrix of dimension $2P \times 2P$. The scattering matrix S can be decomposed into $P \times P$ submatrices, the reflection matrices \tilde{R} and \tilde{R}' , and the transmission matrices \tilde{T} and \tilde{T}' as

$$S = \begin{pmatrix} \tilde{R} & \tilde{T}' \\ \tilde{T} & \tilde{R}' \end{pmatrix}. \quad (2.44)$$

For a wave approaching the sample through the left lead, the reflection matrix \tilde{R} represents the reflected wave emitting through the left lead, and the transmission matrix \tilde{T} represents wave transmitted through the right lead. Similarly, \tilde{R}' and \tilde{T}' represent reflected and transmitted waves coming from the right lead. For a time-reversal invariant system, S equals its

transpose S' i.e. $\tilde{R} = \tilde{R}^T$, $\tilde{R}' = \tilde{R}'^T$, and $\tilde{T} = \tilde{T}'^T$. Time-reversal symmetry is easily broken for an electronic system in presence of magnetic field. Flux conservation dictates that the S -matrix is unitary

$$S S^\dagger = \mathbb{I}. \quad (2.45)$$

This implies additional relations between reflection and transmission matrices. The different symmetry properties of S -matrix and the scattering coefficients through the Landauer-Büttiker formula (see section 2.3) enable us to explain different aspects of electron transport in mesoscopic systems. In chapter 3 we shall use the S -matrix in the context of Friedel-sum-rule for an open multi-channel mesoscopic wire. In chapter 4 with the help of the Landauer-Büttiker approach we shall calculate the 'circulating current', generated in an open multi-channel mesoscopic ring, from the different elements of the S -matrix.

Chapter 3

Friedel-Sum-Rule in Quasi-one-dimensional Quantum Wire

3.1 Introduction

Scattering processes are characterized by the scattering amplitude. While the scattering intensity is directly related to the square modulus of the scattering amplitude, the scattering phase shifts are also very important physical quantities. One can now probe scattering phase shift directly in an experiment [31, 32, 43]. The density of states in a mesoscopic sample and its relation to the scattering matrix is very important for the understanding of mesoscopic transport phenomena. It has been shown by several workers [44–46] that the transport across a mesoscopic sample, connected to leads, can be formulated in terms of the scattering matrix. The DOS gives an idea about the distribution of energies of a system. DOS plays an important role in determining thermodynamic properties (eg. persistent current [36]), electrical conduction phenomena (eg. capacitance [47], charge relaxation resistances [48] etc.). The Friedel-sum-rule (FSR) relates the DOS of a system to the phase of the eigenvalues of the scattering matrix [49, 50]. For large system size, FSR can be stated as [49]

$$\theta_f(E_2) - \theta_f(E_1) = \pi N(E_2, E_1), \quad (3.1)$$

which is also valid for ‘isolated’ (‘closed’) mesoscopic conductor [51]. Here $N(E_2, E_1)$ is the number of particles (electrons) in the energy interval $[E_1, E_2]$ and $\theta_f(E)$ is the ‘Friedel phase’ at energy E . This ‘Friedel phase’ can be expressed in terms of the phase of the eigenvalues of the scattering matrix as,

$$\theta_f(E) = \frac{1}{2} \sum_j \xi_j = \frac{1}{2i} \ln(\text{Det}[\hat{S}]), \quad (3.2)$$

where \hat{S} is the scattering matrix. For the conservation of the probability current the scattering matrix must satisfy unitarity (as we have seen in section 2.7). Furthermore, unitarity implies that the eigenvalues of the scattering matrix must lie on the unit circle in the complex plane. Therefore, one can express the eigenvalues as $\lambda_j = \exp(2i\xi_j)$ with a real quantity ξ_j and j takes values $1, 2, \dots, N$ for \hat{S} -matrix of order $N \times N$.

3.1.1 FSR for isolated mesoscopic conductor

From Eq. (2.3) in the section 2.2 of Chapter 2 we have already seen that the DOS of a system can be expressed in terms of the Green's function. Now we show how one can obtain DOS from the scattering matrix.

The retarded (advanced) Green's function for the isolated (closed) conductor in presence of scatterer can be written as

$$\hat{G}_c^{r(a)} = [(E \pm i\epsilon)\hat{\mathbb{I}} - \hat{H}_0 - \hat{V}]^{-1} \quad (3.3)$$

$$= \hat{G}_0^{r(a)} + \hat{G}_0^{r(a)} \hat{T} \hat{G}_0^{r(a)}, \quad (3.4)$$

where the transfer matrix \hat{T} is dependent on potential responsible for scattering through the relation, $\hat{T} = \hat{V} \sum_{n=0}^{\infty} (\hat{G}_0^{r(a)}(E) \hat{V})^n$. Here, \hat{V} is the impurity potential (scatterer) present in the system and \hat{H}_0 is the free Hamiltonian of the isolated conductor. The total Hamiltonian of the isolated conductor is $\hat{H}_c = \hat{H}_0 + \hat{V}$. $\hat{G}_0^{r(a)}$ is the retarded (advanced) Green's function of the isolated conductor in absence of the scatterer. Now from Eq. (3.4) and Eq. (2.3) we get

$$\rho(E) - \rho_0(E) = -\frac{1}{\pi} \text{Im} \left[\text{Tr}[\hat{G}_0^r \hat{T} \hat{G}_0^r] \right] \quad (3.5)$$

$$= -\frac{1}{\pi} \frac{\partial}{\partial E} \text{Im} \text{Tr} \left[\ln \left(\hat{\mathbb{I}} - \hat{G}_0^r \hat{V} \right) \right] \quad (3.6)$$

$$= \frac{1}{2i\pi} \frac{\partial}{\partial E} \text{Tr} \left[\ln[\hat{\mathbb{I}} + (\hat{G}_0^r - \hat{G}_0^a) \hat{T}] \right] \quad (3.7)$$

$$= \frac{1}{2i\pi} \frac{\partial}{\partial E} \text{Tr} \left[\ln[\hat{\mathbb{I}} - 2i\pi\delta(E\hat{\mathbb{I}} - \hat{H}_0)\hat{T}] \right] \quad (3.8)$$

$$= \frac{1}{2i\pi} \frac{\partial}{\partial E} \text{Tr} \left[\ln[\hat{S}] \right] \quad (3.9)$$

$$= \frac{1}{2i\pi} \frac{\partial}{\partial E} \ln \left[\text{Det}[\hat{S}] \right], \quad (3.10)$$

where $\rho_0(E)$ ($= -\frac{1}{\pi} \text{Im} \left[\text{Tr}[\hat{G}_0^r] \right]$) is the DOS of the isolated conductor without any impurity. Thus from Eq. (3.10) and Eq. (3.2) we get

$$\rho(E) - \rho_0(E) = \frac{1}{\pi} \frac{\partial \theta_f(E)}{\partial E}, \quad (3.11)$$

which is the differential form of the FSR in its canonical form(Eq. (3.1)). Thus for an isolated conductor the canonical FSR is exact as it is for a thermodynamically large system.

3.2 FSR for open mesoscopic conductor

In section 2.2 of Chapter 2 we have already shown that for an open system *i.e.* for a conductor connected with leads, the DOS is affected by the environment. Here we want to see how the FSR is modified for an open mesoscopic conductor.

From Eq. (3.2), for a system having no other scatterer than the system-lead junctions, we can write (for details see Ref. [51])

$$\begin{aligned}\theta_f(E) &= \frac{1}{2i} \ln(\text{Det}[\hat{S}]), \\ &= \text{Im} \ln \text{Det} \left[E\hat{\mathbb{1}} - \hat{H}_c - \Sigma^a \right],\end{aligned}\quad (3.12)$$

where $\left[E\hat{\mathbb{1}} - \hat{H}_c - \Sigma^a \right]^{-1} = \hat{G}_{op}^a$, advanced Green's function for the open system (see section 2.2), Σ^a being the advanced self energy due to the conductor-lead coupling.

From Eq. (3.12), differentiating both sides with respect to energy, we obtain

$$\frac{\partial}{\partial E} \theta_f(E) = \text{Im} \text{Tr} \left[\hat{G}_{op}^a \left(1 - \frac{\partial \hat{\Sigma}^a}{\partial E} \right) \right] \quad (3.13)$$

Then using Eq. (2.9) in Eq. (3.13) we see

$$\begin{aligned}\frac{\partial}{\partial E} \theta_f(E) + \text{Im} \text{Tr} \hat{G}_{op}^a \frac{\partial \hat{\Sigma}^a}{\partial E} &= \text{Im} \text{Tr} \hat{G}_{op}^a \\ &= \pi \rho(E)\end{aligned}\quad (3.14)$$

Eq. (3.14) is the modified FSR for the open mesoscopic system. Note that for open systems (Eq. (3.14)) DOS does not equate to the energy slope of the Friedel phase, there remains another term in the R.H.S. depending on Green's function and energy derivative of self energy incorporating the effect of environment. Introduction of a scatterer inside the system will change the DOS by changing \hat{G}_{op}^a . To get back the canonical form of FSR (Eq. (3.1)), we have to neglect $\frac{\partial \hat{\Sigma}^a}{\partial E}$ i.e. the energy dependence of the self energy in Eq. (3.14). This can be done for 'non-polarizable' leads *i.e.* leads having a large DOS, which can screen away any deviation from charge neutrality in presence of impurity. This approximation is also true in large energy regimes (the so called WKB regime) where usually transport occurs. From section 2.2, the energy-derivative of the self-energy term becomes

$$\frac{\partial}{\partial E} \hat{\Sigma}^a = \frac{\partial}{\partial E} \left[\tau_l^\dagger g_l^a \tau_l \right]. \quad (3.15)$$

Thus we can see that the 2nd term on r.h.s. of Eq. (3.14) is non-zero when either or both of the two terms, the system-lead coupling term $\hat{\tau}_l$ and Green's function of isolated lead \hat{g}_l^a , are energy dependent.

In section 3.4 we shall discuss the importance of this extra term in modified FSR (Eq. (3.14)) for a Q1D quantum wire with one propagating channel (mode) [21]. In section 3.5 we shall extend the study for a multichannel Q1D quantum wire [22].

3.3 Scattering in one-dimension and negative values of $d\theta_f/dE$

Before going to study the FSR for Q1D quantum wire here we recall the FSR in the context of scattering in one dimension. In Fig. 3.1 we consider a scattering problem that is described

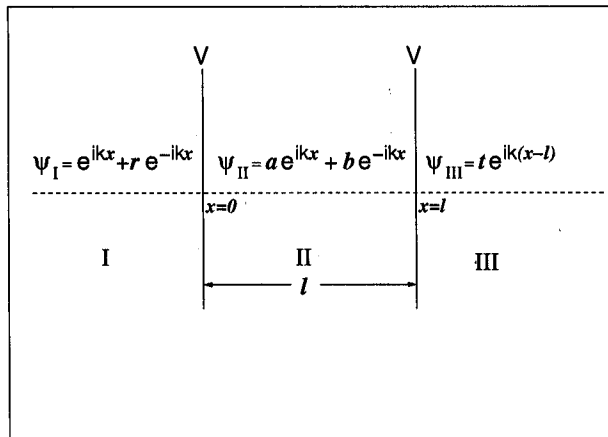


FIGURE 3.1: Two identical delta function potentials separated by a length l . Strength of each potential is V . The thick vertical lines denote the positions of the potentials and the thin horizontal line is the direction of propagation. A plane wave of unit amplitude is incident from the left and wave function in different regions (marked as I, II and III) is written down in the figure. r and t are the reflection and transmission amplitudes, respectively, of the entire system and $k = \sqrt{E}$ is the incident wave vector. The origin of coordinates is shown in the figure.

in details in the figure caption. The quantum mechanical wave function or the solution to the Schrödinger equation in different regions is also shown and explained in the figure and its caption. We shall always normalize the incoming wave-function such that its amplitude is 1. Griffith's boundary conditions for this system gives the following equations [52, 53] (we use $2m = 1$ and $\hbar = 1$).

$$1 + r = a + b, \quad (3.16)$$

$$ae^{ikl} + be^{-ikl} = t, \quad (3.17)$$

$$ik(1 - r) - ik(a - b) = -V(1 + r) \quad \text{and} \quad (3.18)$$

$$ik(ae^{ikl} - be^{-ikl}) - ikt = -V(ae^{ikl} + be^{-ikl}). \quad (3.19)$$

We shall first analyze this system in detail and generalize the results of Refs. [54, 55] further by considering realistic energy dependent r and t , that will later help us to accentuate the new features that can be observed in a Q1D quantum wire in presence of scatterer.

First of all let us calculate the local DOS and global DOS to see how much it agrees with $d\theta_f/dE$. Although the basic facts discussed in this section is known in the Greens function formalism, to the best of our knowledge, quantitative disagreement (or agreement) has not been shown so far. Using quantum mechanical expression for the local DOS integrated over the region II (assuming leads to be unpolarizable) in Fig. 3.1, i.e.,

$$\rho_R = \frac{2}{\hbar v} \int_0^l |ae^{ikx} + be^{-ikx}|^2 dx,$$

it is easy to show from Eq. (3.11) that (the equation below is consistent with Ref. [55] and some hints on its derivation is given in Ref. [56])

$$\frac{d\theta_f}{d(kl)} \approx \bar{\rho} + \frac{\rho_q}{l} = \rho' \text{ (say)}, \quad (3.20)$$

$$\text{where } \bar{\rho} = |a|^2 + |b|^2 \text{ and} \quad (3.21)$$

$$\rho_q = \int_0^l (ab^* e^{2ikx} + ba^* e^{-2ikx}) dx \quad (3.22)$$

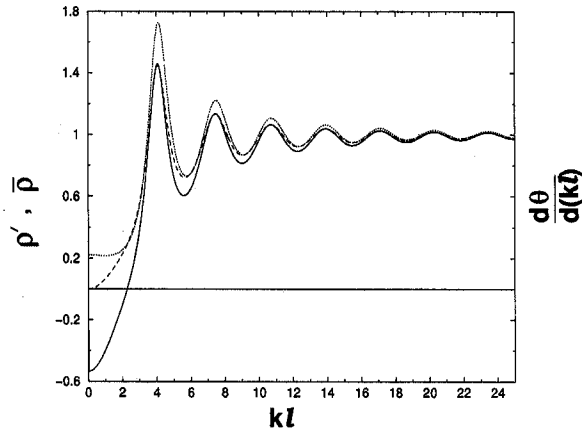


FIGURE 3.2: The solid, dashed and dotted curves denote the exact $d\theta_f/d(kl)$, the ρ' and the $\bar{\rho}$ respectively. All three quantities are plotted as a function of kl . Different system parameters are $Vl^2 = -5$, $\hbar = 1$, $2m = 1$.

Here $\frac{\rho_q}{l}$ is a term that arises because of quantum mechanical interference and it can be seen that the integrand in Eq. (3.22) oscillates with x . For $|\frac{E}{V}| > 1$ (this is the WKB regime when the electron does not feel the potential strongly and is almost entirely transmitted) $\frac{\rho_q}{l}$ is negligibly small. This is shown in Fig. 3.2, where we plot ρ' (the dashed curve) and $\bar{\rho}$ (the dotted curve). The two curves are almost the same for $|\frac{E}{V}| > 1$, which means $\frac{\rho_q}{l}$, being the difference between the dashed and dotted curves is vanishingly small above this energy. It is known that to get the equality between the LHS and RHS of Eq. (3.20), it is necessary to drop the term $\frac{\rho_q}{l}$ [68]. It is also known that this deviation arises because we are considering the local DOS rather than the global DOS,

$$\rho(E) = \frac{2}{\hbar v} \int_{-\infty}^{\infty} \psi^*(x) \psi(x) dx.$$

To get an equality it is necessary to neglect the energy dependence of self energy $\Sigma^{r(a)}$. We shall soon see that in this particular case whenever reflection and transmission amplitudes become energy independent, *i.e.* non-dispersive, $\Sigma^{r(a)}$ becomes non-dispersive and the FSR

in its canonical form (Eq. (3.1)) holds. The ρ_q/l term or the interference term inside the scatterer does not arise in the case when $l \rightarrow 0$ as in the cases to be considered in the following sections 3.4, 3.5.2. All the deviation from Eq. (3.1) to be observed there is due to this dispersive behaviour of self energy.

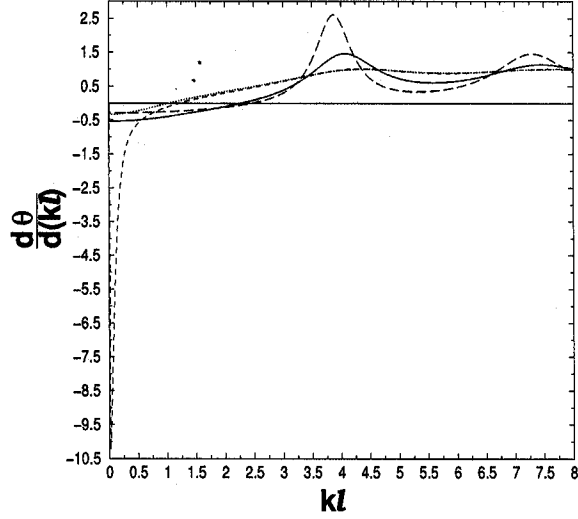


FIGURE 3.3: The quantity $d\theta_f/d(kl)$ is plotted as a function of kl for the different values of Vl^2 . The dotted, dashed, solid and long dashed curves are for $Vl^2 = -2, -2.1, -5$ and -8 respectively. We use $\hbar = 1, 2m = 1$.

One can prove that

$$\bar{\rho} = |a|^2 + |b|^2 = \frac{1 - |r'|^4}{|1 - r'^2 \tau^2|^2},$$

for any energy dependent reflection amplitude r' of one of the two identical scatterers in Fig. 3.1, where, $\tau = e^{ikl}$. Hence as indicated by Eq. (3.20), it would be interesting if we can obtain a good estimate of $\bar{\rho}$ or ρ' from θ_f . In the Appendix C it is explained that if $\frac{dr'}{dE} = \frac{dt'}{dE} \rightarrow 0$ (which means the scatterers are non-dispersive and that only happens at high energy in 1D, 2D and 3D) then, $\frac{d\theta_f}{d(kl)}$ reduces to the expression $\frac{1 - |r'|^4}{|1 - r'^2 \tau^2|^2}$, and then therefore, $\frac{d\theta_f}{d(kl)} = \bar{\rho}$. It is shown in section III of Ref. [51] (see Eq. 6 and 7 therein), that to relate $\frac{d\theta_f}{dE}$ to the global DOS, one has to neglect the energy dependence of the self energy, that depends on the coupling of the system to the leads, i.e., r' and t' . Thus our results are consistent with that. The exact $\frac{d\theta_f}{d(kl)}$ is shown in Fig. 3.2 by the solid curve. Note that in the relevant energy regime ($|\frac{E}{V}| > 1$) (in 1D this is WKB regime), the solid curve is very close to the dashed and dotted curves, which means FSR works very well for the local DOS integrated over a finite region of interest as well as for the global DOS. But for $|\frac{E}{V}| < 1$, $\frac{d\theta_f}{d(kl)}$ deviates from $\bar{\rho}$. But since transport effects in weak localization or diffusive or ballistic regime occur at Fermi energies, that is normally higher in semiconductors as well as metals in comparison

to the energy where the two curves deviate substantially from each other, Friedel sum rule is often useful in condensed matter to obtain a good estimate of local DOS integrated over a finite region of interest as well as global DOS.

$d\theta_f/dE$ is also well known as average Wigner delay time [57, 58]. In the stationary phase approximation, it gives the time spent by the scattered particle at the impurity site. In the low energy regime, where dispersion becomes significant, the stationary phase approximation is not valid. $d\theta_f/dE$ can become negative and does not give a meaningful particle delay time. In this regime $d\theta_f/dE$ becomes negative as the phase velocity becomes larger than the group velocity and even larger than the velocity of light, and although such super-luminous particles can be detected experimentally they cannot carry any signal or information. In Fig. 3.3 we show the negative behavior of $d\theta_f/d(kl)$. We find that as the strength of the impurities is varied, $d\theta_f/d(kl)$ can become more or less negative (see Fig. 3.3), maximizing at $Vl^2 = -2.1$ for the symmetric delta potentials. The energy regime, where $d\theta_f/d(kl)$ can be negative remains the same for all V and always $|\frac{E}{V}| < 1$. We have checked for all these values of V that apart from this insignificant energy range ($|\frac{E}{V}| < 1$), FSR works very well. FSR has a close counterpart in quantum mechanics called Levinson's theorem.

3.4 FSR for single channel Q1D quantum wire

Refs. [54] and [55] parameterize the S -matrix in a particular way (there are in fact many different ways of parameterizing the S -matrix) in which the scattering matrix elements become independent of energy. In the previous section 3.3 we have generalized the work of Refs. [54] and [55] for real energy dependent 2×2 scattering matrices in 1D. In this section we intend to study the FSR for a single channel Q1D quantum wire with a delta-function impurity [21]. In the single channel regime, the Q1D system can be described by a 2×2 scattering matrix. Here we will show that the energy dependence of scattering elements, that are not important in 1D play a very crucial role in Q1D. We will further extend the study for a multi-channel Q1D quantum wire in sections 3.5.1 and 3.5.2.

Metallic or semiconducting conductors are modelled with many point impurities [59]. Hence we will restrict our analysis to delta function potential impurities. The single channel case being the most important because it is in this regime that one can really control the quantum interference effects and use them to build mesoscopic devices [5]. In a single channel quantum wire, in the presence of a single attractive impurity, taken as a negative delta-function potential, the transmission probability can go to zero [60] for some finite energy of the incident electron. At the corresponding energy, the scattering phase-shift shows a discontinuous jump (slip) by π [61, 62]. It was shown that in the single channel case the Friedel phase θ_f or charge transfer is not affected by the discontinuous phase drops [54, 55, 62]. Besides, to study the transport across a quantum dot connected to two ideal leads on two sides, most theoretical studies model the dot by a single bound state at the site of the dot as in the single particle description, the Coulomb blockade makes the other levels of the dot to be insignificant. As an attractive delta potential is capable of creating such a single bound state, it was used in Ref. [62] to explain the Fano resonances in quantum dots and the unusual features of the scattering phase shift observed across the quantum dot. Besides, the present study provides a basis for general understanding, and so that we can comprehend

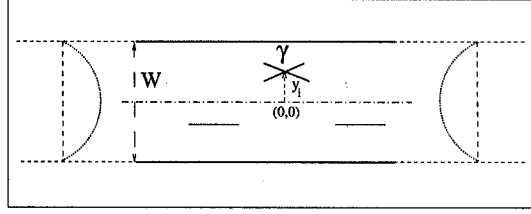


FIGURE 3.4: This is a schematic diagram of a Q1D quantum wire of width W (much less than its length). The dash-dotted curve is a line through the middle of the quantum wire, and it is also taken to be the x -axis. The origin of the coordinates is shown in the figure. An impurity delta function potential $V_a(x, y) = \gamma\delta(x)\delta(y - y_i)$ is situated at $x = 0$ and $y = y_i$ and marked as \times . We consider scattering effects when the incident electron is from the left with an energy E . In the energy range $\frac{\pi^2\hbar^2}{2m_eW^2} < E < \frac{4\pi^2\hbar^2}{2m_eW^2}$, there is only one transverse mode that propagates and the rest of the modes are evanescent. The impurity at \times mixes the different modes to give scattering matrix elements. The transverse wave function in the incident and transmitted channels is shown by dotted lines.

the system and the results of Ref. [55] better.

3.4.1 First principle calculation of scattering matrix and DOS in Q1D quantum wire

In the similar fashion, as we have done in the section 2.7 for non-interacting spinless electrons confined in a Q1D quantum wire (shown in Fig.(3.4)), the Schrödinger equation can be written as

$$\left[-\frac{\hbar^2}{2m_e} \left(\frac{\partial^2}{\partial x^2} + \frac{\partial^2}{\partial y^2} \right) + V_c(y) + V_a(x, y) \right] \psi(x, y) = E\psi(x, y). \quad (3.23)$$

Here all the parameters carry the same meaning as they did in the section 2.7. Using mode rescaling procedure (described in Appendix A) for a static (time independent) Dirac delta function type impurity potential in the Q1D quantum wire, shown in Fig. 3.4, the scattering matrix S becomes

$$S = \begin{pmatrix} \tilde{r}_{11} & \tilde{t}_{11} \\ \tilde{t}_{11} & \tilde{r}_{11} \end{pmatrix} \quad (3.24)$$

when only one channel (mode) is propagating *i.e.* energy of the incident electron lies in the range $E_1 (= \pi^2 \hbar^2 / 2 m_e W^2) < E < E_2 (= 4 \pi^2 \hbar^2 / 2 m_e W^2)$. As we consider single propagating channel, we have only one transmission amplitude \tilde{t}_{11} and one reflection amplitude \tilde{r}_{11} . Bagwell [60] has obtained (see Eq. (A.18) and Eq. (A.29) in Appendix A)

$$\tilde{t}_{11} = 1 + \tilde{r}_{11} = 1 + \frac{-i \frac{\Gamma_{11}}{2k_1}}{1 + \sum_{j>1}^e \frac{\Gamma_{jj}}{2\kappa_j} + i \frac{\Gamma_{11}}{2k_1}} \quad (3.25)$$

$$\text{where } \Gamma_{jj} = (2m_e \gamma / \hbar^2) \sin^2 \left[j \frac{\pi}{W} (y_i + W/2) \right]$$

(see Eq. (A.2) in Appendix A), with γ being the strength of the Dirac delta potential placed at a distance y_i from the centre of the quantum wire of width W (see Fig. 3.4). These scattering matrix elements define the scattering properties of the impurity potential completely. When the impurity potential is positive it can only support scattering states. However when the impurity potential is negative, it can also support some bound states, apart from the scattering states. From Eq.(A.3) we see that for each n we get a sub-band of scattering states (E as a function of k_n). Similarly we get a bound state for each n , that are solutions to (see Ref. ([60]))

$$1 + \sum_{j=n}^{\infty} \frac{\Gamma_{jj}}{2\kappa_j} = 0 \quad (3.26)$$

For $n = 1$ we get a true bound state. The bound state for $n = 2$ may or may not be a true bound state. If the impurity potential is such that the solution to the Eq.(3.26) lie in the energy range where $n = 1$ channel is propagating, then this bound state for $n = 2$, is degenerate with $n = 1$ scattering state and it becomes a quasi-bound state. The scattering matrix is expected to contain all informations of this quasi-bound state, and solving the scattering problem is sufficient.

We calculate the change in DOS due to the impurity potential that can be written as (see Appendix B)

$$\rho(E) - \rho_0(E) = \frac{2|\tilde{r}_{11}|}{\hbar v_1} \int_{-\infty}^{\infty} dx \cos(2k_1 x + \theta_1) + \frac{2}{\hbar v_1} \sum_j^e \frac{|t_{1j}|^2}{\kappa_j}, \quad (3.27)$$

with $v_1 = \hbar k_1 / m_e$, the longitudinal velocity of electron in the propagating mode and θ_1 is the phase of the reflection amplitude \tilde{r}_{11} . Here \sum_j^e denotes sum over all evanescent modes. In Eq. (3.27), t_{1j} is the transition amplitude from the propagating mode to the j -th evanescent mode. We find it in terms of mode coupling constant and wave vectors as (see Appendix A)

$$t_{1j} = \frac{-\frac{\Gamma_{1j}}{2\kappa_j}}{1 + \sum_{j>1} \frac{\Gamma_{jj}}{2\kappa_j} + i\frac{\Gamma_{11}}{2k_1}} \quad (3.28)$$

The 1st term on the r.h.s. of Eq. (3.27) is basically due to the change in the LDOS in the leads. Since the delta function potential is a point impurity, the integrated LDOS in the leads extends from $-\infty$ to ∞ . One can do the integration to find $\int_{-\infty}^{\infty} dx \cos(2k_1 x + \theta_1) = \pi \cos(\theta_1) \delta(k_1)$. So it is zero unless the quasi-bound state coincides with $k_1 = 0$. In the case of extended impurities one can see that this term gives an unimportant small contribution that does not change with energy. Also the carrier concentration in the leads is normally large enough to screen away a small oscillatory LDOS completely. So the relevant quantity that appears in FSR is

$$\rho_{\mathbf{R}}(E) - \rho_{0\mathbf{R}}(E) = \frac{2}{\hbar v_1} \sum_e \frac{|t_{1e}|^2}{\kappa_e}, \quad (3.29)$$

This is actually the integrated local DOS around the impurity site and decaying away from the impurity site all the way up to $\pm\infty$. Here e can take values $2, 3, \dots, \infty$. Thus we can

independently calculate both the change in DOS ($\rho(E) - \rho_0(E)$) and the scattering matrix ($\frac{1}{2i} \frac{\partial}{\partial E} \ln(\det[S])$) starting from 1st principles, where we do not have to throw away dispersive behavior or energy dependence of self energy.

3.4.2 Results and Discussion

We first present below a discussion and definition of the WKB regime for a Q1D system, because it is an interesting subject on its own. It is to be noted that we do not employ WKB approximation anywhere and our calculations are exact. When the incident electron propagates in a potential where the wave-function changes very slowly in space then very little reflected wave is generated and that is taken to be the WKB regime [63]. So a delta function potential in one-dimension (1D) has a WKB regime at higher energies, when the reflection probability is very small. In the inset of Fig. 3.5, where we plot $|\tilde{r}_{11}|^2$ versus incident energy we find that there are three regimes. One is to the left of point P_1 where $|\tilde{r}_{11}|^2$ is large and also strongly energy dependent. The other is between the points P_1 and Q_1 where $\frac{\hbar^2 k_1^2}{2m_e} \gg \gamma$. These two regimes can be seen in 1D scattering (e.g., a delta function potential in 1D) and are the non-WKB and WKB regimes, respectively. The third regime is to the right of the point Q_1 , where again $|\tilde{r}_{11}|^2$ is very small and is hence a WKB regime, but the energy dependence of $|\tilde{r}_{11}|^2$ is very large. Such a regime cannot be seen in 1D and is a specialty of Q1D. So the energies that lie to the left of P_1 is the non-WKB regime, where the electron feels the potential very strongly and is almost entirely reflected back. Energies to the right of the point P_1 correspond to the WKB limit. Although, the system considered here is a Q1D system, corresponding to a scatterer in Q1D, there is an energy dependent scatterer in 1D [61, 64, 65]. The bound states and scattering states of these two potentials are identical and this is an exact correspondence, valid in all regimes, quantum or semi-classical. And so when the reflection probability is small in Q1D, it is also small in the corresponding 1D potential. Then all the notions and results of WKB regime that we are familiar with in 1D are also true in Q1D. In Fig. 3.5 we find a large deviation of $\pi[\rho(E) - \rho_0(E)]$ (dotted curve) from $\frac{d\theta_f}{dE}$ (solid curve) at energies in the non-WKB regime (left of P_1). This is similar to what is seen in 1D, 2D or 3D. In the WKB regime, that is to the right of the point P_1 , although $|\tilde{r}_{11}|^2$ is very small, its energy dependence is not as negligible as that of a potential in 1D (eg, a delta function potential in 1D or a square well in 1D). Energy dependence of $|\tilde{r}_{11}|^2$ automatically implies energy dependence of τ_p (or $\hat{\Sigma}^a$), i.e., dispersive behavior. So there is an appreciable difference between $\pi[\rho(E) - \rho_0(E)]$ and $\frac{d\theta_f}{dE}$. Thus FSR in its canonical form is not very good in the WKB regime and this is counterintuitive.

Let us now analyze the curves (solid and dashed) to the right of Q_1 , analytically. In this region $\kappa_2 \rightarrow 0$. From Eq.(3.29) we find that only the 1st term in the series is relevant. That is

$$\pi[\rho(E) - \rho_0(E)]_{\kappa_2 \rightarrow 0} \text{ diverges as } \left[\frac{2\pi}{\hbar v_1} \frac{\Gamma_{11}}{\Gamma_{22}} \frac{1}{\kappa_2} \right]_{\kappa_2 \rightarrow 0} \quad (3.30)$$

Thus the strong energy dependence in the energy beyond Q_1 is due to the rapid population of the second sub-band through evanescent modes, as it approaches its propagating threshold. Hence, unlike the Fano resonance, this is not a quantum interference effect. This is like the

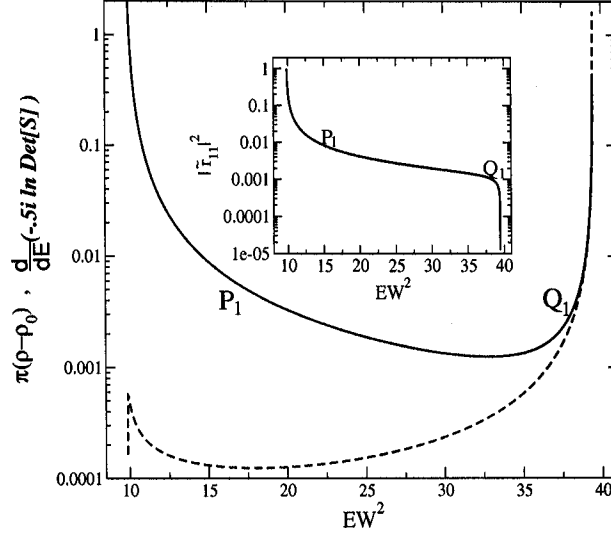


FIGURE 3.5: The dashed curve denotes $\pi(\rho - \rho_0)$ and the solid curve gives $\frac{d}{dE}(-.5i \ln \text{Det}[S])$. Both the quantities are plotted as a function of EW^2 using $x_i = 0$, $y_i = .21W$ and $\gamma = 1$ in linear-log scale. In the inset the corresponding $|\tilde{r}_{11}|^2$ is plotted in linear-log scale. 500 evanescent modes are considered in this calculation.

Van Hove singularity at the band edge. Similarly one can find

$$\left[\frac{d\theta_f}{dE} \right]_{\kappa_2 \rightarrow 0} = \left[\frac{d}{dE} \text{arg}(\tilde{t}_{11}) \right]_{\kappa_2 \rightarrow 0} \quad (3.31)$$

diverges identically. Note that although $\text{arg}(\tilde{t}_{11})$ can have a discontinuity, the derivative exists at all energies. Essentially the right derivative and left derivative is the same at the discontinuity. Hence we prove FSR is exact as $\kappa_2 \rightarrow 0$. This is understood when we note that when $\kappa_2 \rightarrow 0$, $|\tilde{r}_{11}|^2$ goes to zero at the band edge [60]. Also it is known that when $\tilde{r}_{11} = 0$ then τ_p maximizes [5], and energy dependence of g_p^a being negligible, $\frac{d\tilde{\Sigma}^a}{dE} = 0$. Thus all the deviating terms being zero, the FSR is valid around the diverging DOS at the band edge. Fig. 3.6 shows similar things for a stronger impurity.

For strong negative potentials (Fig. 3.7), such that the bound state for $n = 2$ is below the propagating threshold of $n = 1$, the curves look similar to that in Fig. 3.5. For the negative δ function potential with the bound state for $n = 2$, in the propagating regime of $n = 1$, we have plotted the energy derivative of Friedel phase and change in global DOS in Fig. 3.8. $|\tilde{t}_{11}|^2$ is shown in the inset. Note that $|\tilde{t}_{11}|^2$ shows that at the point P the system is in extreme non-WKB regime where $|\tilde{t}_{11}|^2$ goes to zero. At this energy there is a quasi-bound state and there is strong energy dependence of scattering matrix elements as well as self energy. According to earlier stated results [45], there should be violation of FSR here.

The peak in $\pi[\rho(E) - \rho_0(E)]$ at P occurs due to the quasi-bound state. We also see that at this very point P there is an exact agreement between L.H.S. & R.H.S. of Eq.(3.11). This can be even verified analytically. Substituting the bound state condition given in Eq.(3.26)

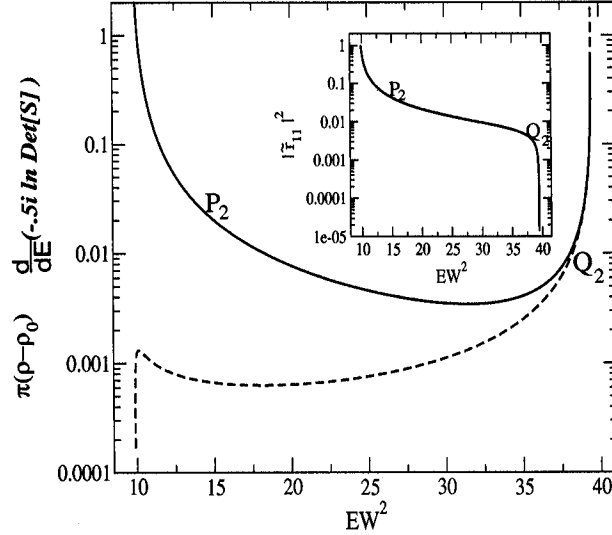


FIGURE 3.6: The dashed curve and solid curve denote $\pi(\rho - \rho_0)$ and $\frac{d}{dE}(-.5i \ln \text{Det}[S])$, respectively. Both the quantities are plotted as a function of EW^2 using $x_i = 0$, $y_i = .21W$ and $\gamma = 10$ in linear-log scale. In the inset the corresponding $|\tilde{r}_{11}|^2$ is plotted in linear-log scale. 1000 evanescent modes have been considered to perform this calculation.

into $\frac{d\theta_f}{dE}$ as well as in $\pi[\rho(E) - \rho_0(E)]$ separately, we get

$$\frac{d\theta_f}{dE} = \frac{m_e k_1}{\hbar^2} \frac{1}{\Gamma_{11}} \sum_{n>1} \frac{\Gamma_{nm}}{\kappa_n^3} = \pi[\rho(E) - \rho_0(E)] \quad (3.32)$$

This agreement between $\frac{d\theta_f}{dE}$ and $\pi[\rho(E) - \rho_0(E)]$ was argued to be equal for the case of a stub in ref [55], at the transmission zero where the $\frac{\partial \hat{\Sigma}^a}{\partial E}$ term in Eq.(3.14) was dropped from the very beginning [55]. Dropping the energy dependence of $\hat{\Sigma}^a$ in non-WKB regime and verifying the validity of FSR is rather meaningless, as the violations do come from the energy dependence of $\hat{\Sigma}^a$. Even after including these terms we get exact agreement at the transmission zero for the negative δ function potential in a quantum wire, although it is in extreme non-WKB regime. The reasons are as follows. At the transmission zero, since there is a quasi-bound state, $\hat{\Sigma}^a$ becomes minimum and $\frac{\partial \hat{\Sigma}^a}{\partial E} = 0$. All these arguments are also true for the stub.

3.5 Phase shifts, phase times and FSR in multi-channel Q1D quantum wire

In this section we extend the study of the scattering problem in the Q1D quantum wire system with a Dirac delta function impurity but in the regime where incident energy of the electron is such that in addition to the lowest mode, higher modes are also propagating [22].

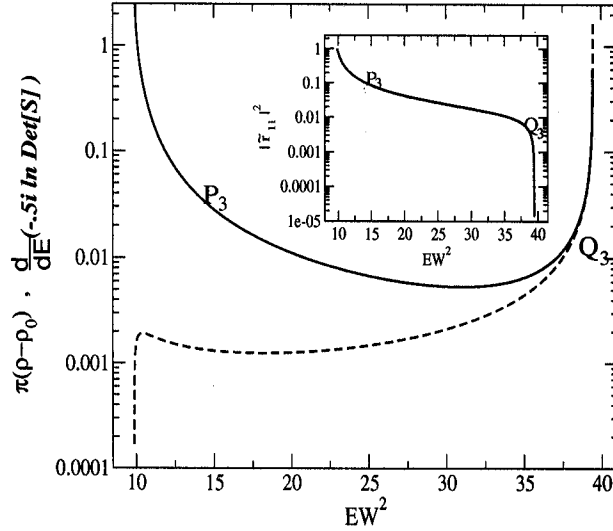


FIGURE 3.7: The dashed curve and solid curve denote $\pi(\rho - \rho_0)$ and $\frac{d}{dE}(-.5i \ln \text{Det}[S])$, respectively. Both the quantities are plotted as a function of EW^2 using $x_i = 0$, $y_i = .21W$ and $\gamma = -10$ in linear-log scale. In the inset the corresponding $|\tilde{r}_{11}|^2$ is plotted in linear-log scale. 1000 evanescent modes have been considered.

In this multichannel case since the unitarity of a particular channel is absent and the electron can escape to a different channel, the scattering scenario differs from that we have seen for the single channel case (section 3.4). Here the transmission zeroes are replaced by minima and the associated discontinuous phase slip by π are replaced by continuous and less than π phase drops [22]. We shall see that in the multi channel case too the Friedel phase θ_f is not affected by these continuous phase drops [22].

For a static symmetric scatterer in a strictly 1D system when transmission and reflection amplitudes are denoted by $\tilde{\mathcal{T}}$ and $\tilde{\mathcal{R}}$, respectively,

$$S = \begin{pmatrix} \tilde{\mathcal{R}} & \tilde{\mathcal{T}} \\ \tilde{\mathcal{T}} & \tilde{\mathcal{R}} \end{pmatrix}$$

In this case, one can show [55]

$$\frac{\partial \theta_f}{\partial E} = \frac{\partial \theta_t}{\partial E}, \quad (3.33)$$

where θ_t corresponds to the transmission phase.

For systems, that are not strictly one dimensional, however, has a 2×2 scattering matrix (single channel Q1D system)

$$\frac{\partial \theta_f}{\partial E} \neq \frac{\partial \theta_t}{\partial E}, \quad (3.34)$$

because unlike a strictly one dimensional system, in them the transmission zero is associated with a phase jump (by a value π). Thus when we go from 1D (with 2×2 S-matrix) to Q1D (also with 2×2 S-matrix) then Eq. (3.33) does not hold, *i.e.* in general, energy derivative of Friedel phase can not be obtained from any transmission phase time. This analysis was

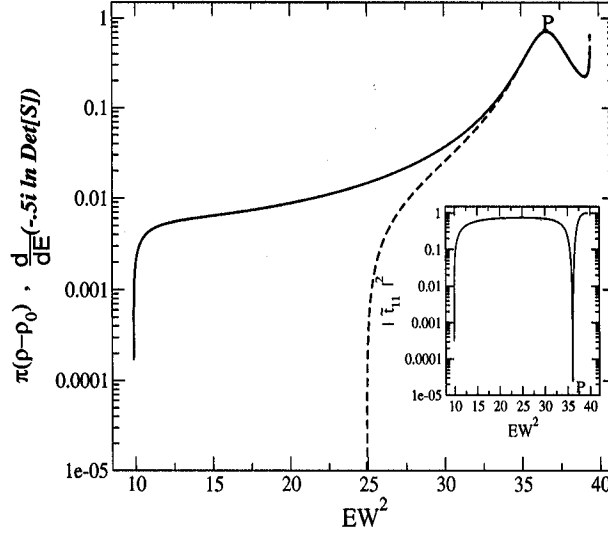


FIGURE 3.8: The solid curve and the dashed curve denote $\pi(\rho - \rho_0)$ and $\frac{d}{dE}(-.5i \ln \text{Det}[S])$, respectively. Both the quantities are plotted as a function of EW^2 using $x_i = 0$, $y_i = .21W$ and $\gamma = -1.5$ in linear-log scale. For this value of γ there is a quasi-bound state at $EW^2 = 36.1022$. In the inset the corresponding $|\tilde{t}_{11}|^2$ is plotted in linear-log scale. 500 evanescent modes have been considered.

presented by Lee [54] and by Büttiker and Taniguchi [55]. We shall show that $\partial\theta_f/\partial E$ can be related to the Wigner delay time of any one of the reflection amplitudes. In section 3.5.3 we will show some novel phase shifts at critical energies where S matrix changes dimensions. Then we present some concluding remarks.

3.5.1 Wigner delay time in quasi-one-dimensions

In Fig. 3.9 we consider a quasi-one-dimensional quantum wire with an attractive impurity at $(0, y_i)$, having electrons confined along the y -direction but free to move along the x -direction. While the states far away from the impurity are good momentum states, the impurity can mix the different modes and in this region of mode mixing, the wave function is $\psi(x, y) = \sum_n c_n(x) \chi_n(y)$, where $\chi_n(y)$ are the transverse wave functions in the absence of the impurity and $c_n(x)$ are position dependent coefficients that has to be determined by mode matching. The confining potential in the y -direction or the transverse direction is taken to be hard wall. Thus the transverse wave-function is of the form $\chi_n(y) = \sin \frac{n\pi}{W}(y + \frac{W}{2})$. For a given width W of the quantum wire one can choose the energy range of the incident electron such that only two modes are propagating, although, all the other modes (infinite in number, showing that the internal wave function can have infinite degrees of freedom, which makes it difficult to calculate the exact local DOS from the internal wave function) will be present but as evanescent modes. For example, if the energy of the electron be E then for propagation in the n -th transverse mode (in short we will refer this as n -th mode)

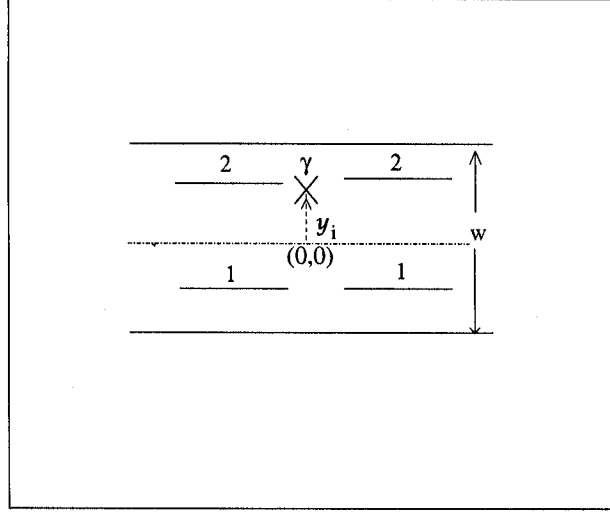


FIGURE 3.9: Schematic diagram of a quantum wire of width W with an impurity $V(x, y) = \gamma \delta(x) \delta(y - y_i)$ at \times . The dash-dotted curve is a line through the middle of the quantum wire, and it is also taken to be the x-axis. The origin of the coordinates is shown in the figure. We consider scattering effects when the incident electron is from the left. The sub-bands marked as 1 on the left and right of the impurity denote the first mode (i.e., its wave function can be obtained by putting $n=1$ in Eq. (3.35) with appropriate sign for k_n). Similarly, sub-bands marked as 2 on the left and right of the impurity denote the second mode (i.e., its wave function can be obtained by putting $n=2$ in Eq. (3.35) with appropriate sign for k_n).

the wave-function is of the form

$$\sin \left[\frac{n\pi}{W} \left(y + \frac{W}{2} \right) \right] e^{ik_n x} \quad (3.35)$$

where $k_n = \sqrt{E - E_n}$, E_n being $\frac{n^2 \pi^2}{W^2}$ and $n = 1, 2, 3, \dots, \infty$. Here we have used $\hbar = 2m = 1$. To have the n -th mode to be propagating it is necessary that $k_n^2 > 0$ or

$$n < \frac{W}{\pi} \sqrt{E}. \quad (3.36)$$

Thus we can choose the energy range where there will be two propagating modes, i.e., $n = 1$ and $n = 2$ satisfy condition (3.36). The rest of the modes ($n > \frac{W}{\pi} \sqrt{E}$) will be evanescent, whose wave functions are of the form

$$\sin \frac{n\pi}{W} \left(y + \frac{W}{2} \right) e^{-\kappa_n x} \quad (3.37)$$

where $\kappa_n = \sqrt{E_n - E}$. These evanescent modes just renormalize the scattering matrix elements and drop out of the problem.

In this case the scattering matrix S can be written as

$$S = \begin{bmatrix} \mathbb{R} & \mathbb{T} \\ \mathbb{T}' & \mathbb{R}' \end{bmatrix} \quad (3.38)$$

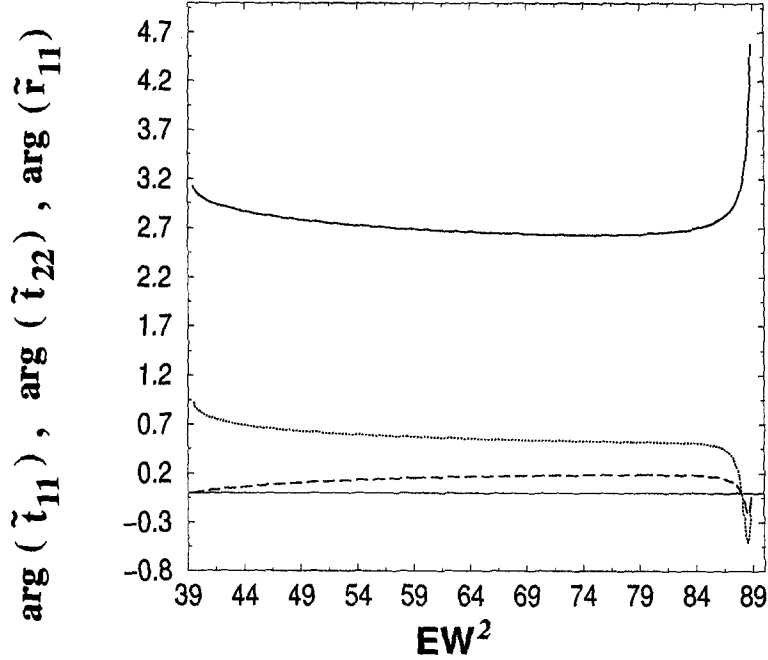


FIGURE 3.10: The argument of various reflection and transmission amplitudes (in radians), from incident channel m to propagating channel n , are plotted as a function of EW^2 . The solid, long dashed and dotted curves denote $arg(\tilde{r}_{11})$, $arg(\tilde{t}_{11})$ and $arg(\tilde{t}_{22})$ respectively. The different system parameters are $\gamma = -10$, $y_i = .21W$ and $x_i = 0$.

where \mathbb{R} , \mathbb{R}' consist of all the reflection amplitudes and \mathbb{T} , \mathbb{T}' consist of all the transmission amplitudes present in the two channel propagating regime. As our system obeys time reversal symmetry, we obtain $\mathbb{T} = \mathbb{T}'$. Further for a symmetric scatterer, as that considered here, $\mathbb{R} = \mathbb{R}'$. Thus the scattering matrix becomes

$$S = \begin{bmatrix} \mathbb{R} & \mathbb{T} \\ \mathbb{T} & \mathbb{R} \end{bmatrix}, \quad (3.39)$$

$$\text{with } \mathbb{R} = \begin{bmatrix} \tilde{r}_{11} & \tilde{r}_{12} \\ \tilde{r}_{21} & \tilde{r}_{22} \end{bmatrix} \quad (3.40)$$

$$\text{and } \mathbb{T} = \begin{bmatrix} \tilde{t}_{11} & \tilde{t}_{12} \\ \tilde{t}_{21} & \tilde{t}_{22} \end{bmatrix} \quad (3.41)$$

The elements of \mathbb{R} are related through [60]

$$\tilde{r}_{mn} = -\frac{i\Gamma_{mn}}{2d\sqrt{k_m k_n}}, \quad (3.42)$$

$$\text{where } d = 1 + \sum^e \frac{\Gamma_{\alpha\alpha}}{2\kappa_\alpha} + i \sum^p \frac{\Gamma_{nn}}{2k_n}. \quad (3.43)$$

Here \sum^e denotes the sum over all evanescent modes and \sum^p denotes the sum over all propagating modes. Here $m, n = 1, 2$. Eq. (3.42) also holds for inter-sub-band transmission

amplitudes *i.e.* \tilde{t}_{12} and \tilde{t}_{21} . The intra-sub-band transmission amplitudes \tilde{t}_{11} and \tilde{t}_{22} are given by

$$\tilde{t}_{mm} = 1 + \tilde{r}_{mm}. \quad (3.44)$$

Here $\Gamma_{\alpha\beta}$ is the strength of coupling between the α -th mode and the β -th mode. If we take the impurity to be a delta function potential *i.e.*, $V(x, y) = \gamma\delta(x)\delta(y - y_i)$, and the confining potential in the y -direction to be hard wall ($V = \infty$ for $-\frac{W}{2} \geq y \geq \frac{W}{2}$, and 0 everywhere else except the impurity site \times) (see Fig. 3.9) then

$$\Gamma_{\alpha\beta} = \gamma \sin \frac{\alpha\pi}{W} \left(y_i + \frac{W}{2}\right) \sin \frac{\beta\pi}{W} \left(y_i + \frac{W}{2}\right).$$

Apart from the two propagating modes we consider two evanescent modes and truncate the infinite series of evanescent modes (note that although the series is strongly converging, the reason for truncating is different, stronger and explained in more detail after Fig. 3.14) in Eq. (3.43) and so Eq. (3.42) becomes

$$1 + \frac{\Gamma_{33}}{2\kappa_3} + \frac{\Gamma_{44}}{2\kappa_4} + i \left(\frac{\Gamma_{11}}{2k_1} + \frac{\Gamma_{22}}{2k_2} \right) = d_2 \text{ (say)}. \quad (3.45)$$

The lowest evanescent mode (putting $n=3$ in Eq. (3.37) gives its wave function) has even parity in the transverse direction. For a negative impurity potential *i.e.*, $\gamma < 0$, it also has a quasi bound state at $E = E_{3b}$, where E_{3b} is given by the solution of

$$1 + \frac{\Gamma_{33}}{2\kappa_3} + \frac{\Gamma_{44}}{2\kappa_4} = 0. \quad (3.46)$$

Since $E_{3b} < \frac{9\pi^2}{W^2}$, E_{3b} can be degenerate with scattering states. The higher evanescent mode (putting $n=4$ in Eq. (3.37) gives its wave function) has odd parity in the transverse direction and this too has a quasi bound state at $E = E_{4b}$, where E_{4b} is given by the solution of

$$1 + \frac{\Gamma_{44}}{2\kappa_4} = 0. \quad (3.47)$$

Once again depending on γ , E_{4b} can be degenerate with the scattering states. The effect of including more evanescent modes is just to renormalize the strength of the impurity potential and does not give anything new [60].

Due to micro-reversibility $\tilde{r}_{12} = \tilde{r}_{21}$. Also $\tilde{r}_{12} = \tilde{t}_{12}$ because in both \tilde{r}_{12} and \tilde{t}_{12} ($= \tilde{t}_{21}$) the density of states in the input as well as the output channel is the same, and also the incident channel momenta and the outgoing channel momenta are the same in the transverse as well as in the propagating direction. Thus in Eq. (3.39) only 5 elements are distinct. They are \tilde{r}_{11} , \tilde{r}_{12} , \tilde{r}_{22} , \tilde{t}_{11} and \tilde{t}_{22} .

From Eq. (3.42) and (3.44),

$$\tilde{r}_{11} = -\frac{i\Gamma_{11}}{2d_2k_1}, \quad (3.48)$$

$$\tilde{r}_{12} = -\frac{i\Gamma_{12}}{2d_2\sqrt{k_1k_2}}, \quad (3.49)$$

$$\tilde{r}_{22} = -\frac{i\Gamma_{22}}{2d_2k_2}, \quad (3.50)$$

$$\tilde{t}_{11} = \frac{1 + \frac{\Gamma_{33}}{2\kappa_3} + \frac{\Gamma_{44}}{2\kappa_4} + i\frac{\Gamma_{22}}{2k_2}}{d_2} \quad \text{and} \quad (3.51)$$

$$\tilde{t}_{22} = \frac{1 + \frac{\Gamma_{33}}{2\kappa_3} + \frac{\Gamma_{44}}{2\kappa_4} + i\frac{\Gamma_{11}}{2k_1}}{d_2} \quad (3.52)$$

Knowing these matrix elements, the scattering matrix is completely known and θ_f can also be calculated.

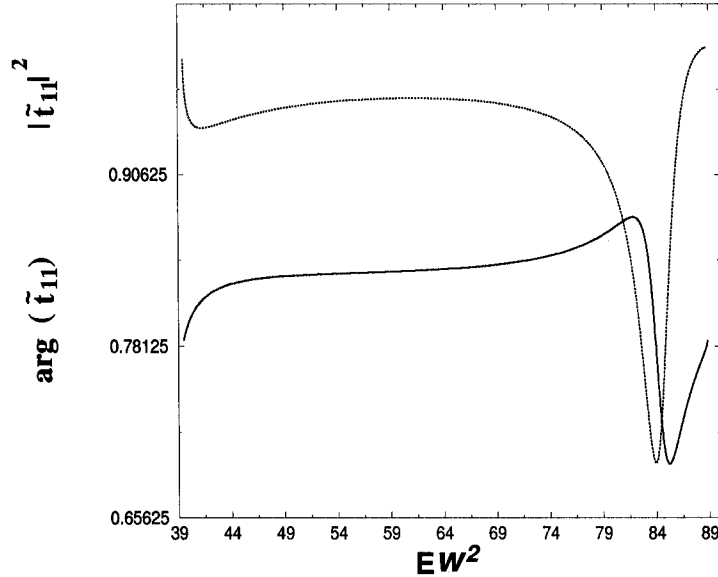


FIGURE 3.11: The solid curve denotes $arg(\tilde{t}_{11})$ in radians shifted by $\frac{\pi}{4}$ radians in the y-direction while the dotted curve denotes $|\tilde{t}_{11}|^2$. Both the quantities are plotted as a function of EW^2 . The different system parameters are $x_i = 0$, $y_i = .45W$ and $\gamma = -15$.

We find some further relationships between the scattering phase shifts as follows. First of all

$$arg(\tilde{r}_{11}) = arg(\tilde{r}_{22}) = \tan^{-1} \frac{Re(d)}{Im(d)}. \quad (3.53)$$

Secondly, when $\frac{4\pi^2}{W^2} < E_{3b} < \frac{9\pi^2}{W^2}$, i.e., the quasi bound state of the 3rd sub-band lies in the energy range where one can have two propagating sub-bands, then the quasi bound state E_{3b}

drastically changes the scattering matrix elements in that energy range. So in this energy range $\frac{4\pi^2}{W^2}$ to $\frac{9\pi^2}{W^2}$ we find

$$\arg(\tilde{r}_{12}) \mp \frac{\pi}{2} = \theta_f + \pi. \quad (3.54)$$

Here negative sign is to be taken when E_{3b} lies in this energy range. Otherwise the positive sign has to be taken. θ_f is to be calculated from Eq. (2) using Eq. (3.39). Thirdly we find

$$\arg(\tilde{r}_{11}) \pm \pi = \arg(\tilde{r}_{12}). \quad (3.55)$$

Note that in contrast to Eq. (3.54) here the choice of \pm sign is arbitrary. However consistent with this choice is the following

$$\arg(\tilde{r}_{11}) \pm \frac{\pi}{2} = \theta_f + \pi, \quad (3.56)$$

where once again $+$ sign is to be taken when E_{3b} is present in this energy range and $-$ sign is to be taken when absent.

We thus find very simple analytical expressions for θ_f in the sense that one need not calculate it from a 4×4 scattering matrix but can calculate it from the argument of a single matrix element like \tilde{r}_{11} or \tilde{r}_{12} or \tilde{r}_{22} . These relations are analogous to Eq. (3.33) in section 3.5 obtained for purely one dimensional case, i.e., one need not calculate θ_f from 2×2 matrix but one can find it from the argument of a single matrix element.

In Fig. 3.10, we plot only the distinct arguments of the scattering amplitudes versus energy of the incident electron. We find that all of them show negative slopes over a very large range of energy and as already discussed, such negative slopes give rise to fundamental questions in quantum mechanics [57, 58]. Now in Q1D we find that this negative slope is not restricted to low energy but can occur at any arbitrary energy. Notice for example, $\arg(\tilde{t}_{11})$ and $\arg(\tilde{t}_{22})$ show larger negative slopes at the highest possible energies for two channel propagation. The rest of this section will be devoted to understanding these negative slopes that at first sight looks very different in nature and character in the three curves in Fig. 3.10, and also to understanding what will happen when there are more than two propagating modes.

It is to be noted that among all these scattering matrix elements \tilde{r}_{11} and \tilde{t}_{11} exist in the single channel regime (i.e., $\pi^2 < EW^2 < 4\pi^2$) where \tilde{r}_{11} is the reflection amplitude and \tilde{t}_{11} is the transmission amplitude. The phase of \tilde{t}_{11} in the single channel regime is known to change discontinuously by π when \tilde{t}_{11} is 0, i.e., \tilde{t}_{11} has a zero in real energy. In the two channel regime if we write from simplifying Eq. (3.51)

$$\tilde{t}_{11} = \frac{k_2(2\kappa_3 + g_3) + i\kappa_3 g_2}{k_2(2\kappa_3 + g_3) + i\kappa_3(g_2 + \alpha g_1)}, \quad (3.57)$$

where $\alpha = \frac{k_2}{k_1}$ and $g_s = \frac{2\kappa_4}{\Gamma_{44} + 2\kappa_4} \Gamma_{ss}$; with $s=1,2,3$. then interestingly, we see that it has a zero in complex energy and not in real energy.

If we modify the Breit-Wigner line shape formula of 1D to include complex zeroes and write

$$t_{mbw}(E) = A \frac{E - E_0 + i\Gamma_0}{E - E_p + i\Gamma_p}, \quad (3.58)$$

where A is a normalization factor, then just as Γ_p gives the scale over which $\arg[t_{mbw}(E)]$ increase at $E = E_p$, Γ_0 gives a scale over which $\arg[t_{mbw}(E)]$ decrease at $E = E_0$ where $|t_{mbw}(E)|^2$ also shows a minimum at $E = E_0$ (but not zero). One can check this very easily (let us say, when $E_0=2$, $E_p=1$ and $\Gamma_0 = \Gamma_p = 0.5$) and so we do not demonstrate it here. Now from Eq. (3.57) we see that at an energy which satisfies the condition

$$2\kappa_3 + g_3 = 0, \quad (3.59)$$

the real part of the numerator in Eq. (3.57) is zero. Condition (3.59) is the same as the condition (3.46) for a quasi bound state E_{3b} coming from the 3rd sub-band that is degenerate with scattering states. So, around this energy where Eq. (3.59) is satisfied (lets say at $E = E_{3b} \equiv E_0$) $\arg(\tilde{t}_{11})$ will undergo a drop over an energy scale determined by the imaginary part, $\kappa_3 g_2$, i.e., $\Gamma_0 \equiv \kappa_3 g_2$.

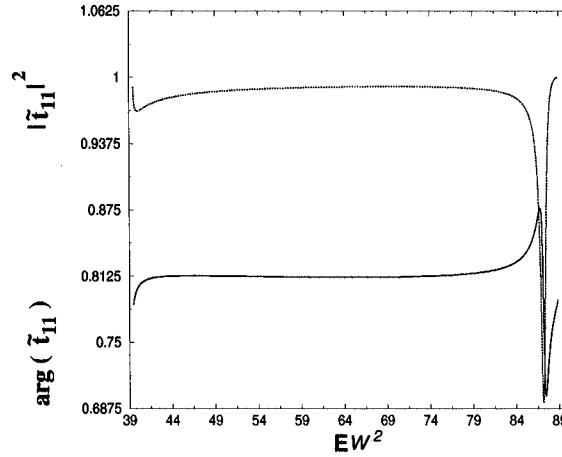


FIGURE 3.12: The solid curve denotes $\arg(\tilde{t}_{11})$ in radians shifted by $\frac{\pi}{4}$ radians in the y-direction while the dotted curve denotes $|\tilde{t}_{11}|^2$. Both the quantities are plotted as a function of EW^2 . The different system parameters are $x_i = 0$, $y_i = .45W$ and $\gamma = -10$.

It can be seen in Fig. 3.11 that $|\tilde{t}_{11}|^2$ (dotted curve) shows a narrow minimum around an energy $EW^2 \simeq 84$ (which is the solution of Eq. (3.59) or Eq. (3.46)) and at this energy $\arg(\tilde{t}_{11})$ shows a very sharp drop over a narrow energy range determined by $\kappa_3 g_2$. Hence by decreasing/increasing this quantity $\kappa_3 g_2$ we can make the phase drop sharper/broader. g_2 can be made smaller in two ways, first by decreasing γ and second by taking the impurity closer to a node in the transverse wave function. The plot for a decreased value of γ is shown in Fig. 3.12 and it confirms this.

Note that the quantity $\kappa_3 g_2$ is actually energy dependent. But in Fig. 3.11 and Fig. 3.12 $\kappa_3 g_2$ is so small that the drop occurs over a scale in which $\kappa_3 g_2$ is roughly constant. For larger values of $\kappa_3 g_2$, the phase drop will be determined by a complex competition between κ_3 and g_2 . This is shown in Fig. 3.13. First of all the scale of the phase drop becomes so large that any sensitivity to the position of the quasi bound state can not be seen. Secondly, $\kappa_3 g_2$ can not be taken to be a constant over this large scale and the enhancement of the

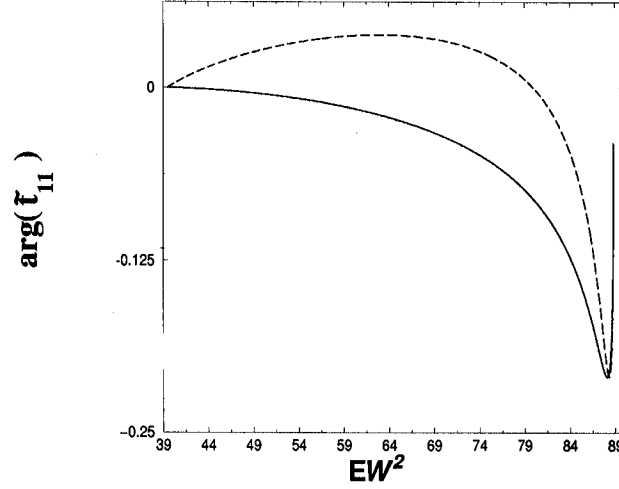


FIGURE 3.13: The phase of the transmission amplitude $arg(\tilde{t}_{11})$ is plotted as a function of EW^2 for different values of γ . The solid and dashed curves are for $\gamma = -47.1371$ and -25.197 respectively. For both cases the quantity $arg(\tilde{t}_{11})$ is shifted by 2π radians in the negative y-direction. Other system parameters are $x_i = 0$ and $y_i = .21W$.

negative slope for $EW^2 > 79$ is a signature of the fact that here $\kappa_3 \rightarrow 0$ and so $\kappa_3 g_2 \rightarrow 0$ as EW^2 increases.

Similarly if we rewrite Eq.(28) as

$$\tilde{t}_{22} = \frac{k_1(2\kappa_3 + g_3) + i\kappa_3 g_1}{k_1(2\kappa_3 + g_3) + i\kappa_3(g_1 + \beta g_2)},$$

where $\beta = \frac{k_1}{k_2}$; then it is clear that the behavior of $arg(\tilde{t}_{22})$ will be qualitatively the same. It is indeed found in Fig. 3.10 that the behavior of $arg(\tilde{t}_{22})$ is similar to that of $arg(\tilde{t}_{11})$.

$\theta_f = \frac{1}{2i} \ln[\det[S]]$ is shown in Fig. 3.14 as a function of energy, for different values of γ . The minimum in θ_f follows the E_{3b} and so the energy range where the slope of θ_f versus E is negative is determined by the E_{3b} . Note that when E_{3b} goes out of this energy range the θ_f versus E has a positive slope everywhere. So in Fig. 3.14, the negative slope arises whenever a quasi bound state E_{3b} is degenerate with the scattering states ($n=1$ and $n=2$), and scatter and disperse the scattering states in a non-monotonic manner. For weaker impurities in Q1D, the negative slope occur at higher energies and also are steeper as demonstrated in Fig. 3.14. This is in contrast to what happens in 1D and demonstrated in Fig. 3.3, that the energy where the negative slopes occur is always for $E/V < 1$.

We have used two evanescent modes in our calculations because one can include as many evanescent modes without changing the nature of the negative slopes as long as the positions of the quasi bound states E_{3b} and E_{4b} remain the same. One can check this that with four evanescent modes and $\gamma = -6.46584$, the negative slopes are the same as in Fig. 3.10, which means that the third and the fourth evanescent modes just renormalizes γ from -6.46584 to -10 . The exact renormalization takes place according to a formula $\gamma^{(h)} = \gamma^{(n)}/d$, where $\gamma^{(h)}$ is the γ value used here and $\gamma^{(n)}$ is the renormalized value of γ when we use

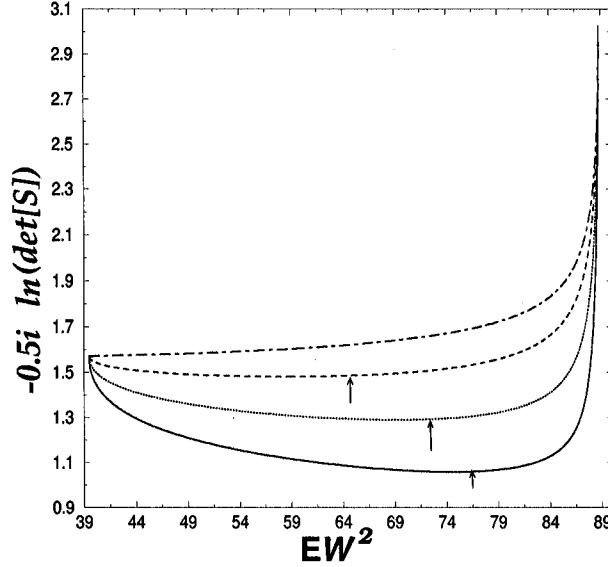


FIGURE 3.14: The Friedel phase θ_f is plotted as a function of EW^2 for different γ . The solid, dotted and dashed curves are for $\gamma = -10, -15$ and -25.197 respectively and the corresponding E_{3b} are at $EW^2 = 87.982, 86.606$ and 80 respectively. The dot-dashed curve is shifted by π radians in y -direction for $\gamma = -47.1371$, corresponding E_{3b} is at $EW^2 = 35$ which is less than the propagating threshold $EW^2 \simeq 39$ of the second transverse mode. The dashed curve is for $\gamma = -25.197$, corresponding E_{3b} is at $EW^2 = 80$. The dotted curve is for $\gamma = -15$, corresponding E_{3b} is at $EW^2 = 86.606$. The solid curve is for $\gamma = -10$, corresponding E_{3b} is at $EW^2 = 87.982$. We use $y_i = .21W$ and $x_i = 0$. The arrows accentuate the positions of the minima that shift towards higher energies for weaker impurities.

m evanescent modes instead of two. $d = (1 + \Gamma_{55}^{(n)}/(2\kappa_5) + \Gamma_{66}^{(n)}/(2\kappa_6) \dots \Gamma_{mm}^{(n)}/(2\kappa_m))$, where $\Gamma_{mm}^{(n)} = \gamma^{(n)} \sin \frac{m\pi}{W}(y_i + \frac{W}{2})^2$. Solving this one can find the renormalized value of γ i.e., $\gamma^{(n)}$ that keep the minimum of any of the curves for the scattering phase shifts considered here unchanged. It is worthwhile mentioning that at the band edges (i.e., $E \approx 39$ and 89 , in the figures considered in this section), the value of any curve is independent of the number of evanescent modes, as all the modes get decoupled there. In other words, number of evanescent modes considered does not change the nature of the negative slopes. Only the positions of the quasi bound states are important.

We find from Eqs. (3.53), (3.54), (3.55) and (3.56)

$$\frac{d}{dE} \arg(\tilde{r}_{mn}) = \frac{d}{dE} \left(\frac{1}{2i} \ln[\det[S]] \right) \quad (3.60)$$

We find the above relation to be true for any number of propagating modes. So m and n can take any integer value less than or equal to p , where p is the total number of propagating modes. For two propagating modes $p=2$, for three propagating modes $p=3$ and so on. So Eq. (3.60) is analogous to the 1D case given in Eq. (3.33). That is when the dimension of the matrix S becomes very large, then it is sufficient to consider the argument of a single

matrix element in order to calculate the complicated quantity on the RHS of Eq. 41. In the energy regime where there are two propagating channels, the negative slopes in θ_f versus incident energy curves are determined by E_{3b} , and when there are 3 propagating channels then the negative slopes are determined by E_{4b} and so on.

The scattering phase shifts of transmission channels i.e. $\arg(\tilde{t}_{mn})$, where again m and n can take all possible integer values less than or equal to p , show sharp or gentle phase drops when the scattering states are degenerate with a quasi bound state, depending on the value of the imaginary part in the numerator of \tilde{t}_{mn} . In the single channel regime the imaginary part in the numerator is zero and phase drops take the limiting value when the phase drops are absolutely discontinuous by π . Just as the discontinuous phase drop in single channel case do not affect θ_f in any way, the phase drops of the $\arg(\tilde{t}_{mn})$ also do not affect θ_f in any way and θ_f behaves similarly as $\arg(\tilde{r}_{mn})$.

3.5.2 Density of States and Friedel sum rule in quasi-one-dimension

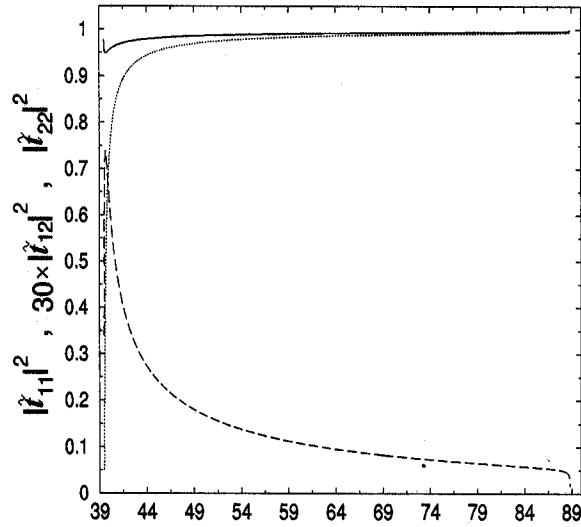


FIGURE 3.15: The system under consideration is shown in Fig. 3.9 with $\gamma = 1$. The Fig. shows some important scattering probabilities. The solid curve gives $|\tilde{t}_{11}|^2$ and it shows that for $EW^2 > 50$, a particle incident in the first propagating mode does not feel the scatterer at all, and is almost entirely transmitted intra-channel, $|\tilde{t}_{11}|^2$ being close to unity. The dotted curve gives $|\tilde{t}_{22}|^2$ and once again for $EW^2 > 50$, it is close to unity signifying that a particle incident in the second propagating channel is almost entirely transmitted intra-channel. So $EW^2 > 50$ is the WKB regime where the potential scatters the incident electron very weakly. The dashed curve gives 30 times $|\tilde{t}_{12}|^2 (= |\tilde{r}_{12}|^2)$ and shows strong energy dependence not only for $EW^2 < 50$ but also around the highest energy ($EW^2 \approx 89$) or in the extreme WKB limit, its absolute value being extremely small there signifying extremely low inter-channel transmission i.e., the incoming particle does not feel the scatterer.

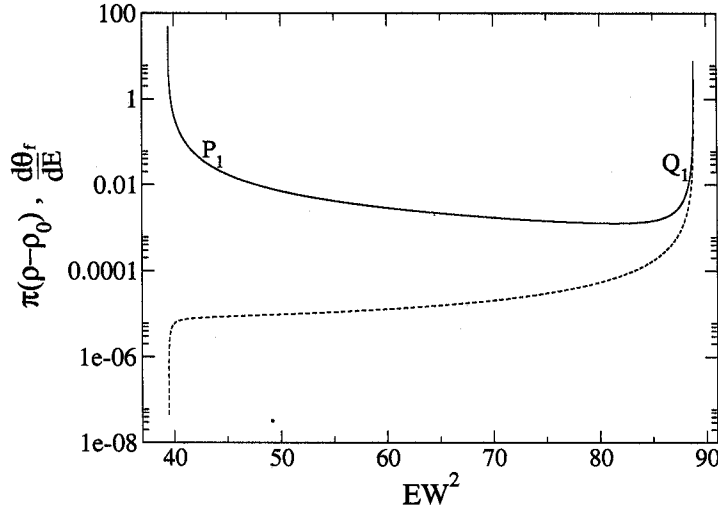


FIGURE 3.16: The system under consideration is shown in Fig. 3.9 with $\gamma = 1$. The solid and dashed curves denotes $\frac{d\theta_f}{dE}$ and $\pi(\rho(E) - \rho_0(E))$ respectively. The two curves deviate from each other, where ever the curves in Fig. 3.15 are strongly energy dependent. Otherwise they agree.

The local DOS integrated over the region of interest R is given by the following expression [60]

$$\rho_R = \int_R dx \int_{-\frac{W}{2}}^{\frac{W}{2}} dy \sum_{m, k_m} \delta(E - E_{m, k_m}) |\psi_{m, k_m}(x, y)|^2 \quad (3.61)$$

Here E is the incident energy and R is the integration region where modes are mixed. m and k_m are the two quantum numbers that define an incident electron wave-function, $A_m e^{ik_m x} \sin \frac{m\pi}{W}(y + \frac{W}{2})$ whose energy is E_{m, k_m} , where we have taken that the electron is incident from the left i.e., $x < 0$. $\psi_{m, k_m}(x, y)$ is the wave-function in the region of mode mixing and $\psi_{m, k_m}(x, y) = \sum_n c_n^{(m)}(x, k_n) \sin \frac{n\pi}{W}(y + \frac{W}{2})$. Here $c_n^{(m)}(x, k_n) = C_n e^{ik_n x}$ for $n = 1$ and $n = 2$ and $c_n^{(m)}(x, k_n) = C_n e^{-\kappa_n x}$ for $n > 2$; x being greater than or equal to 0. The coefficients C_n can be determined by using the mode matching technique. The mode matching has been done in details by Bagwell [60]. Here the delta function potential is taken to be extending from $-\epsilon$ to $+\epsilon$ which has to be set to be tending to 0 in the end. ρ_{0R} can be determined by replacing $\psi_{n, k_n}(x, y)$ by the plane wave states in absence of the scatterer and doing the integration again.

Extending Eq.(3.29) to multichannel propagation, we find that for any non-zero incident energy

$$(\rho(E) - \rho_0(E))_R = \sum_p \frac{2}{\hbar v_p} \sum_e \frac{|t_{pe}|^2}{\kappa_e}. \quad (3.62)$$

Here $v_p = \frac{\hbar k_p}{m}$ with v_p corresponding to the velocity of electron in p -th propagating mode. \sum_p and \sum_e denote sum over all propagating and evanescent modes respectively.

Note that if we calculate the global DOS by taking the integration region to be from $-\infty$ to ∞ instead of just the region R where the modes are mixed then Eq. (3.62) remain the same. One will get some extra integrals that are indefinite integrals but using the current conservation condition it can be analytically proved (see Appendix B) that they cancel each other. ρ_q/l like terms are zero for δ function potential. Thus in this case (the proof is given in Appendix B)

$$\rho(E) - \rho_0(E) = (\rho - \rho_0)_R$$

and both of them deviate identically from $\frac{1}{\pi} \frac{d\theta_f}{dE}$ due to strong dispersion, at any arbitrary energy. As can be seen in Fig. 3.14 that $\frac{d\theta_f}{dE}$ is negative over a very large energy range while $(\rho - \rho_0) = (\rho - \rho_0)_R$ as given by Eq.3.62 is positive. This can be understood easily if one recalls Eq.(3.14) and remembers that the positive contribution of $\partial\Sigma^a/\partial E$ term can make $\frac{d\theta_f}{dE}$ negative even when $(\rho - \rho_0)_R$ is positive.

Since the negative slopes are due to the quasi bound states supported by the negative delta function potential, one may ask what happens for a positive delta function potential that does not support any quasi bound state. This situation is discussed below and it also elaborates the uniqueness of the Q1D, with respect to the importance of $\partial\Sigma^a/\partial E$ in Friedel sum rule and shows that the contribution from self energy can be large even in the WKB limit. Note that Σ^a depends on scattering probabilities. Fig. 3.15 shows the energy dependence of some important scattering probabilities. The figure is similar to Fig. 3.5 analyzing FSR for single propagating channel in Q1D. In Fig. 3.16 in the left of P_1 , the non-WKB regime, there is large deviation of $\pi(\rho - \rho_0)$ from $d\theta_f/dE$, similar to 1D, 2D and 3D. In the right of P_1 though $|\tilde{t}_{11}|^2 \rightarrow 1$ (Fig. 3.15) indicating WKB regime, the dispersive behaviour of the transmission and reflection amplitudes remain strong enough implying energy dependence of Σ^a , so canonical form of FSR is not very good in this regime. Whereas in the region to the right of Q_1 , $\kappa_3 \rightarrow 0$ thus the two terms diverging as $1/\kappa_3$ match at this band edge.

3.5.3 Phase Behavior at Critical Energies

Very interesting phase behaviors can be seen at energies where the S -matrix changes dimension. For example for $E \leq \frac{4\pi^2}{W^2}$ there is only one propagating mode and the S -matrix is 2×2 . But for $E > \frac{4\pi^2}{W^2}$, there are two propagating modes and the S -matrix is 4×4 . The matrix element \tilde{r}_{11} exists on either side of the energy $\frac{4\pi^2}{W^2}$ and in Fig. 3.17 we show the behavior of $\arg(\tilde{r}_{11})$ in the energy range that includes $EW^2 = 4\pi^2$. Note that it exhibits a discontinuous phase drop by $\frac{\pi}{2}$ at $EW^2 = 4\pi^2$. So far only discontinuous phase drops of π has been observed but never $\frac{\pi}{2}$. From the properties of a 2×2 S -matrix it follows that if there is a discontinuous phase change then it can only be of π [54, 55]. So had the S -matrix been 2×2 on either side of $EW^2 = 4\pi^2$ the phase drop would have been π . But since the S -matrix is 2×2 only on one side, including $EW^2 = 4\pi^2$, i.e., $E \leq \frac{4\pi^2}{W^2}$, the phase drop is also one half of π . $|\tilde{r}_{11}|^2$ also has a zero at $EW^2 = 4\pi^2$ for all possible choice of parameters [60], and this zero is associated with a $\frac{\pi}{2}$ phase jump instead of a π phase jump.

Next we take a repulsive δ function potential. It is known [60] that at critical energies like $EW^2 = 4\pi^2$, $|\tilde{t}_{11}|^2$ shows discontinuities. Here $|\tilde{t}_{11}|^2$ does not have a zero but exhibits a discontinuous jump. At these points $\arg(\tilde{t}_{11})$ also shows non-analytic behavior as demonstrated

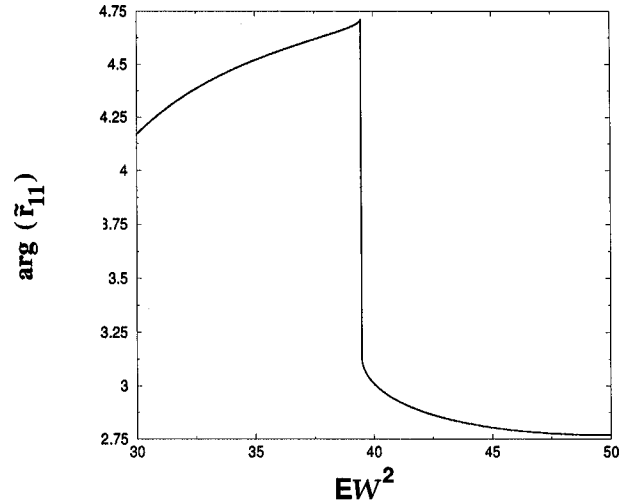


FIGURE 3.17: The system under consideration is shown in the Fig. 3.9. The plot is of $\arg(\tilde{r}_{11})$ in radians versus EW^2 . This plot is for $\gamma = -25.197$, $x_i = 0$ and $y_i = .45W$.

in Fig. 3.18. In this case $\frac{d}{dE}\arg(\tilde{t}_{11})$ is discontinuous.

3.6 Fano resonance

We have seen in the previous sections (section 3.4 and section 3.5) that the mixing (degenerate) between the continuum states (scattering states) and quasi-bound discrete state gives rise to asymmetric lineshape in transmission amplitudes (see Eq. (3.25), Eq. (3.57)) as a function of energy of the incident electron. This asymmetric lineshape characterized by zero-pole structure in complex energy plane is named after its inventor and is called ‘Fano resonance’. In this section we shall discuss the subtle aspects of the Fano resonance through a simple toy model [23].

The electronic states of atoms and molecules are characterized in the lowest level of approximation (the mean field or Hartree-Fock description) in terms of the electron occupancy of the single particle states corresponding to motion in an average potential. Thus, for example, the ground state of the Helium atom is described as $(1s)^2\ ^1S_0$, that is, two electrons in the spin singlet state in the lowest single particle orbital (in conformity with the Pauli exclusion principle). The first excited state is that of the excited configuration expressed in the standard spectroscopic notation as $(1s\ 2s)\ ^3S_1$. Various excited states of the Helium atom may be excited from the ground state by the scattering of electrons or photons and show up as peaks (or Breit-Wigner resonances) in the elastic scattering cross-section and also in the excitation spectrum for the inelastic processes. This description in terms of single particle states is only approximate, and the true state can be found by considering the effect of perturbations due to the interactions beyond mean field resulting in the mixing of configurations.

A qualitatively different situation arises, however, when we consider the excitation of

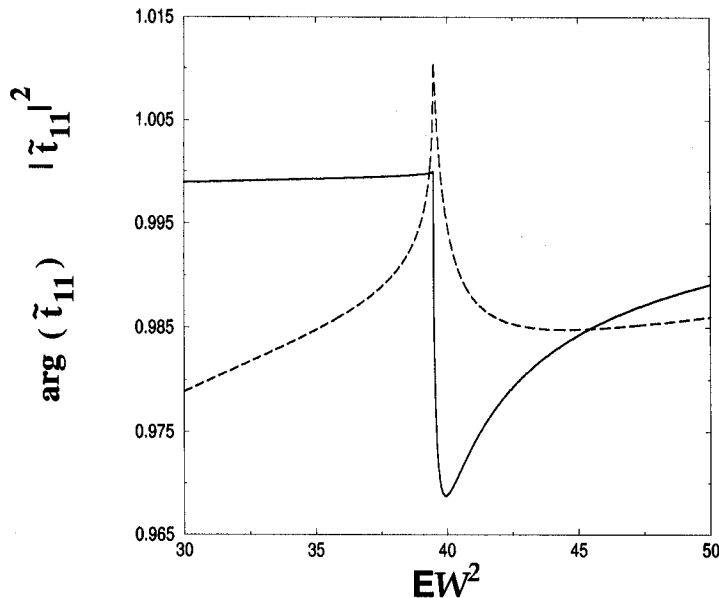


FIGURE 3.18: The solid curve denotes $|\tilde{t}_{11}|^2$. The dashed curve is plotted after subtracting 5.27183 radians from $\arg(\tilde{t}_{11})$ in radians. Both the quantities are plotted as a function of EW^2 . We use $\gamma = +25.197$, $x_i = 0$ and $y_i = .45W$.

a sufficiently high-energy configuration, for example, the $(2s2p)^1P_1$ state of the Helium atom which possesses an energy above the lowest ionization threshold. If excited, such a state would be auto-ionizing, decaying into $\text{He}^+ + e^-$, and would manifest itself as a highly asymmetric peak in the excitation spectrum. A qualitative understanding of the origin of such peaks (known as Fano resonances) was provided by Rice [69] and by Fano, [70] and a quantitative treatment, rendered subtle by the fact that it involves the mixing between a discrete state and one belonging to a continuum (with the attendant degeneracy in energy), had to await almost a quarter of a century [71].

There has been renewed interest in the Fano resonance in recent years in connection with interference effects in quantum dots [72] and in the Aharonov-Bohm ring with a quantum dot embedded in one arm [73]. Hence, it is desirable to clarify the essence of the mechanism underlying the Fano resonance by considering exactly soluble models that avoid the calculational complications needed for realistic systems. To obtain a simple realization of such a resonance, consider the elastic scattering of a particle by a target system describable in terms of a potential V_g . The subscript g states that the target is in its ground state. Suppose that the target has an excited state of energy Δ above its ground state. When the projectile energy E is above the threshold Δ , an inelastic process is possible in addition to elastic scattering. This scattering is described in terms of two channels, the elastic and the inelastic. The latter channel corresponds to the scattering of the projectile of energy $E > \Delta$ from the excited state of the system through a potential V_e ; the two channels are coupled to each other via a

potential V_c . The system is governed by the coupled Schrödinger equations

$$(T + V_g)|\psi\rangle + V_c|\phi\rangle = E|\psi\rangle, \quad (3.63a)$$

$$(T + V_e)|\phi\rangle + V_c|\psi\rangle = (E - \Delta)|\phi\rangle, \quad (3.63b)$$

where $|\psi\rangle$ and $|\phi\rangle$ denote the states in the elastic and inelastic channels respectively and T is the kinetic energy operator for the projectile. If the projectile and target, which interact via the potential V_e , has a bound state with energy less than Δ , the would-be bound state of the excited channel lies in the continuum of the elastic channel, the two channels being coupled by the potential V_c .

We shall consider two solvable examples and show that the probability for the excitation of the quasi-bound auto-ionizing state exhibits a resonance at an energy $E_p < \Delta$ with a finite width Γ corresponding to a complex pole of the corresponding amplitude of the form $(E - E_p + i\Gamma/2)^{-1}$, similar to what occurs in Breit-Wigner resonance. The amplitude also possesses a concomitant zero at a real energy $E = E_0$ near the resonance energy E_p . The juxtaposition of a complex pole at $E_p - i\Gamma/2$ and a real zero of the excitation probability in the energy plane gives rise to a highly asymmetric peak as the energy passes through the value corresponding to the energy of the auto-ionizing state (the bound state in the continuum). The generic pole-zero structure of the amplitude can be written in the form $a(E) = (E - E_0)/(E - E_p + i\Gamma/2) = (\epsilon + q_F)/(\epsilon + i)$, where ϵ measures the separation of the incident energy from the resonance position in units of $\Gamma/2$, that is, $\epsilon = (E - E_p)/(\Gamma/2)$ and the asymmetry in lineshape is described by the Fano parameter $q_F = (E_p - E_0)/(\Gamma/2)$. Thus the excitation lineshapes in the neighborhood of the Fano resonance are given by

$$f(\epsilon) = |a(E)|^2 = \frac{(q_F + \epsilon)^2}{1 + \epsilon^2}, \quad (3.64)$$

where other weakly varying factors have been appropriately factored out to emphasize the main features. These lineshapes[71] for different values of the asymmetry parameter q_F are shown in Fig. 3.19. The asymmetry parameter q_F may be positive or negative depending on the sign of $E_p - E_0$ that is, the relative location of the zero, E_0 , and the pole, E_p . The curves for negative values of q_F may be obtained by letting $\epsilon \rightarrow -\epsilon$.

3.6.1 Dirac Delta model for the Fano resonance

A solvable realization of the two channel problem is provided by a particle of mass m moving in one dimension where the potentials in Eq. (3.63) are taken to be Dirac delta functions. We make a further simplification by taking $V_g(x) = 0$, which results in the elastic channel corresponding to a free particle except for the coupling potential $V_c(x)$. Thus the bound state from the inelastic channel is embedded in a free particle continuum, creating the simplest scenario for the Fano resonance. We take $V_g(x) = 0$, $V_c(x) = -\lambda_c\delta(x)$, and $V_e(x) = -\lambda\delta(x)$ with $\lambda > 0$ and define $\tilde{\lambda} \equiv 2m\lambda/\hbar^2$, $\tilde{\lambda}_c \equiv 2m\lambda_c/\hbar^2$, $k^2 \equiv 2mE/\hbar^2$ and $q^2 \equiv 2m(E - \Delta)/\hbar^2$, so that Eq. (3.63) becomes

$$\frac{d^2}{dx^2}\psi(x) + \tilde{\lambda}_c\delta(x)\phi(x) = -k^2\psi(x), \quad (3.65a)$$

$$\frac{d^2}{dx^2}\phi(x) + \tilde{\lambda}\delta(x)\phi(x) + \tilde{\lambda}_c\delta(x)\psi(x) = -q^2\phi(x). \quad (3.65b)$$

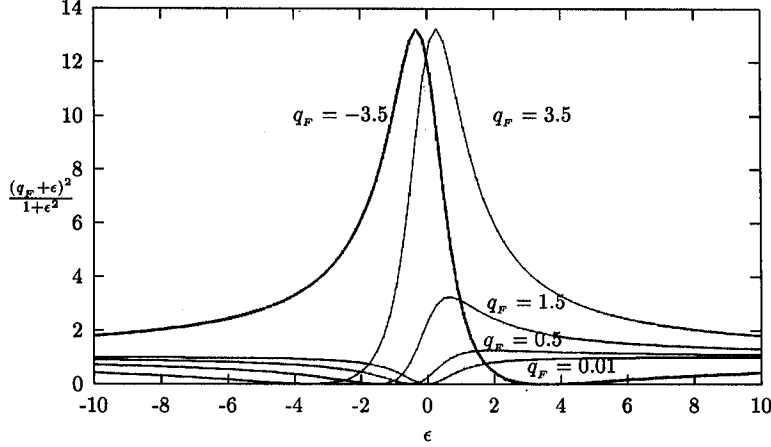


FIGURE 3.19: Fano line shape for different values of the Fano parameter q .

We begin by discussing the region above the inelastic threshold where $E > \Delta$. Because Ref. [71] discusses the problem using partial wave phase shifts, we will cast the one-dimensional transmission and reflection solutions in terms of eigenchannels[74] (analogous to angular momentum partial waves for central potentials; see Appendix A). Because Eq. (3.65) is symmetric under the parity operation $x \rightarrow -x$, the solutions ψ and ϕ may be classified as even or odd under the transformation. For an attractive delta function potential in one dimension, there is always one and only one bound state that has symmetric parity. Also the odd (or anti-symmetric) function vanishes at $x = 0$ and hence a delta function potential $\delta(x)$ makes no contribution (because $\delta(x)\psi(x)$ and $\delta(x)\phi(x)$ vanish if $\psi(x = 0) = 0$ and $\phi(x = 0) = 0$). Therefore, the only nontrivial solutions are the ones that are even under $x \rightarrow -x$. We observe that for $\lambda_c = 0$ (when the elastic and inelastic channels are uncoupled), the elastic channel corresponds to a free particle and has only plane wave solutions, while in the inelastic channel there are continuum solutions (taken to be box normalized) described by

$$\phi_0(x) = \frac{1}{\sqrt{L}}[e^{-iqx} + a_0 e^{iqx}], \quad (3.66a)$$

and a bound state solution

$$\phi_0(x) = \sqrt{\beta_0} e^{-\beta_0|x|}, \quad (3.66b)$$

with

$$a_0 = \frac{q + i\tilde{\lambda}/2}{q - i\tilde{\lambda}/2} \quad \text{and} \quad \beta_0 = \frac{\tilde{\lambda}}{2}. \quad (3.67)$$

We consider only the nontrivial solutions which are even under $x \rightarrow -x$. The bound state occurs at $E = \Delta - \frac{\hbar^2 \tilde{\lambda}^2}{2m \cdot 4}$. If $\Delta > \frac{\hbar^2 \tilde{\lambda}^2}{2m \cdot 4}$, the bound state in the inelastic channel (lying below its threshold $E < \Delta$) is in the energy regime where the only process taking place is elastic scattering. Note that the bound state corresponds to a pole of $a_0(q)$ at $q = i\tilde{\lambda}/2$. (For an excellent description of the connection between bound states and poles of the scattering amplitude the reader is referred to the text book of Gottfried.[75])

Now let us consider the effect of coupling between the two channels. For particles incident in the elastic channel we must solve Eq. (3.65) and search for solutions of the form:

$$\psi(x) = \frac{1}{\sqrt{4\pi}} [e^{-ik|x|} + Ae^{ik|x|}] \quad (3.68a)$$

$$\phi(x) = \frac{a}{\sqrt{2\pi}} e^{iq|x|}, \quad (3.68b)$$

because in the inelastic channel described by $\phi(x)$ we have only outgoing waves. We obtain

$$A = \frac{q - i\frac{\tilde{\lambda}}{2} - \frac{\tilde{\lambda}_c^2}{4k}}{q - i\frac{\tilde{\lambda}}{2} + \frac{\tilde{\lambda}_c^2}{4k}} \quad (3.69a)$$

$$a = \frac{i\tilde{\lambda}_c}{\sqrt{2}(q - i\frac{\tilde{\lambda}}{2} + \frac{\tilde{\lambda}_c^2}{4k})}, \quad (3.69b)$$

and $|A|^2 + 2|a|^2 \frac{q}{k} = 1$, which follows directly from Eq. (3.69) and is a consequence of unitarity (probability current conservation), which means that the incident probability current equals the sum of the final probability currents in the elastic and inelastic channels. The factor of q/k arises from the ratio of the currents in the inelastic and elastic channels and the factor of 2 represents particles in the inelastic channel emerging to the left and to the right. Note that the pole of A has shifted compared to that of a_0 which is an effect of the coupling of strength λ_c . Also note that as $\lambda_c \rightarrow 0$, $A \rightarrow 1$ as it should because we have taken $V_g = 0$.

To find the pole's location, we solve a fourth order equation in k . Instead of obtaining numerical results, we solve for the pole position, k_p , for small λ_c . We readily find (see Appendix B) that

$$k_p \cong [\tilde{\Delta} - \frac{\tilde{\lambda}^2}{4}]^{1/2} + \tilde{\lambda}_c^4 \frac{(2\tilde{\Delta} + \tilde{\lambda}^2)}{64(\tilde{\Delta} - \frac{\tilde{\lambda}^2}{4})^{5/2}} - i\tilde{\lambda}_c^2 \frac{\tilde{\lambda}}{8(\tilde{\Delta} - \frac{\tilde{\lambda}^2}{4})}. \quad (3.70)$$

For small λ_c the pole moves away from the real axis in the k -plane and sits in the fourth quadrant close to the real axis.

It is useful to study the analytic properties of a scattering amplitude as a function of energy considered as a complex variable. Bound states appear as poles of the scattering amplitude at real negative values of the energy (scattering corresponds of course to positive energy), and resonances are associated with poles at complex values of the energy $E = E_r - i\Gamma/2$, where E_r and Γ define the location and width respectively (see Ref. [75]).

The amplitudes have so far been expressed as a function of k . To study their nature with respect to the energy, we note that $E = \hbar^2 k^2 / 2m$ and we need to calculate a mapping from the k -plane to the k^2 -plane. From Eq. (3.69a) we see that $A(-k) = A^{-1}(k)$ because the points k and $-k$ are mapped onto the same point in the k^2 -plane, the function $A(k)$ is not single valued in k^2 unless we introduce a branch cut from $k^2 = 0$ to ∞ along the real axis. This is known as the unitarity cut. The upper half complex k -plane is mapped onto the first Riemann sheet and the lower half k -plane onto the second Riemann sheet. (See Ref. [76] for a discussion of general aspects of the underlying mathematics.) We map the pole at k_p in

the k -plane (as in Eq. (3.70)) onto the k^2 -plane as

$$E_p - i\frac{\Gamma}{2} \cong \Delta - \frac{\hbar^2}{2m} \left[\frac{\tilde{\lambda}^2}{4} - \tilde{\lambda}_c^4 \frac{(\tilde{\Delta} + \frac{\tilde{\lambda}^2}{4})}{16(\tilde{\Delta} - \frac{\tilde{\lambda}^2}{4})^2} \right] - i\frac{\hbar^2}{2m} \tilde{\lambda}_c^2 \frac{\tilde{\lambda}}{4(\tilde{\Delta} - \frac{\tilde{\lambda}^2}{4})^{1/2}}. \quad (3.71)$$

To obtain a physical understanding of the width, Γ , of the resonance, we recognize that this ‘‘bound state in a continuum’’ or the ‘‘auto-ionizing’’ state with an unperturbed energy $E = \Delta - \frac{\hbar^2}{2m} \frac{\tilde{\lambda}^2}{4}$ decays into the continuum states of the elastic channel caused by the interaction $H_{\text{int}} = -\lambda_c \delta(x)$. To obtain the rate of the decay for small $\tilde{\lambda}_c$, it is sufficient to use time-dependent perturbation theory or Fermi’s golden rule, so that the decay rate = $\frac{2\pi}{\hbar} |\langle f | H_{\text{int}} | i \rangle|^2 \frac{d\rho}{dE}$, where the initial state is the unperturbed bound state described by the wave-function $\langle x | i \rangle = \sqrt{\frac{\tilde{\lambda}}{2}} e^{-\frac{\tilde{\lambda}}{2}|x|}$, the final unperturbed state is $\langle x | f \rangle = \frac{1}{\sqrt{L}} e^{ik|x|}$, and the number of states of a free particle between p and $p + dp$ is $d\rho = \frac{Ldp}{h}$, which gives $\frac{d\rho}{dE} = \frac{L}{h} \frac{d(\hbar k)}{dE} = \frac{L}{2\pi} \left(\frac{d}{dE} \sqrt{\frac{2mE}{\hbar^2}} \right)_{E=\Delta - \frac{\hbar^2}{2m} \frac{\tilde{\lambda}^2}{4}} = \frac{L}{4\pi} \sqrt{\frac{2m}{\hbar^2}} \frac{1}{\sqrt{\Delta - \frac{\hbar^2}{2m} \frac{\tilde{\lambda}^2}{4}}}$. Accordingly, the decay rate for the auto-ionizing state to go into the continuum is given by

$$\begin{aligned} \frac{\Gamma}{\hbar} &= \frac{2\pi}{\hbar} \left| \int_{-\infty}^{\infty} \frac{1}{\sqrt{L}} e^{-ik|x|} (-\lambda_c) \delta(x) \left(\frac{\tilde{\lambda}}{2} \right)^{1/2} e^{-\frac{\tilde{\lambda}}{2}|x|} dx \right|^2 \frac{L}{4\pi} \sqrt{\frac{2m}{\hbar^2}} \frac{1}{\sqrt{\Delta - \frac{\hbar^2}{2m} \frac{\tilde{\lambda}^2}{4}}} \\ &= \frac{\hbar}{2m} \frac{\tilde{\lambda}_c^2 \tilde{\lambda}}{4 \sqrt{\tilde{\Delta} - \frac{\tilde{\lambda}^2}{4}}}, \end{aligned} \quad (3.72)$$

in agreement with our earlier result (expressed by Eq. (3.71)) describing the excursion of the pole into the complex plane. We may use perturbation theory to verify that the shift in the real part of energy to order $\tilde{\lambda}_c^2$ is zero.

To understand the origin of the Fano zero, we must examine the elastic scattering amplitude A at energies below the onset of the inelastic channel $E < \Delta$. In this region Eq. (3.65) becomes,

$$\frac{d^2}{dx^2} \psi(x) + \tilde{\lambda}_c \delta(x) \phi(x) = -k^2 \psi(x), \quad (3.73a)$$

$$\frac{d^2}{dx^2} \phi(x) + \tilde{\lambda} \delta(x) \phi(x) + \tilde{\lambda}_c \delta(x) \psi(x) = \beta^2 \phi(x), \quad (3.73b)$$

where $\beta^2 = \frac{2m}{\hbar^2} (\Delta - E) > 0$. Note that β is not an eigenvalue to be determined, but is determined by the energy E of the incident beam. The open channel solutions $\psi(x)$ correspond to continuum states, while the closed or evanescent channel function $\phi(x)$ is exponentially damped. However, because we are concerned with the mixing between $\psi(x)$ and $\phi(x)$, we need to adopt a normalization for the two functions. Bayman and Mehoke [74] proposed a method where the open channels are normalized to unit flux and the closed channels are normalized with an analogous factor (which would result from analytic continuation). We

write the solutions of Eq. (3.73) as

$$\psi_k(x) = \xi_k \frac{1}{\sqrt{4\pi}} \frac{1}{\sqrt{k}} (e^{-ik|x|} + A e^{ik|x|}), \quad (3.74a)$$

$$\phi(x) = \sqrt{1 - |\xi_k|^2} \frac{1}{\sqrt{i\beta}} \frac{1}{\sqrt{(1 - e^{-\beta L})}} e^{-\beta|x|}, \quad (3.74b)$$

where the probability amplitudes, ξ_k and $\sqrt{1 - |\xi_k|^2}$, are to be determined. If these solutions are substituted into Eq. (3.73), we obtain

$$A = \frac{\tilde{\lambda} - 2\beta - i\frac{\tilde{\lambda}_c^2}{2k}}{\tilde{\lambda} - 2\beta + i\frac{\tilde{\lambda}_c^2}{2k}} \quad (3.75a)$$

$$\frac{\xi_k}{\sqrt{1 - |\xi_k|^2}} = \frac{\sqrt{\pi k}}{\sqrt{\beta}} \frac{1}{\tilde{\lambda}_c} e^{i\frac{\pi}{4}} (2\beta - \tilde{\lambda} + \frac{\tilde{\lambda}_c^2}{2ik}), \quad (3.75b)$$

where $|A| = 1$ due to unitarity because the inelastic channel is closed. Note that in the limit $\lambda_c \rightarrow 0$, we have $|\xi_k| \rightarrow 1$, which means that the bound state decouples from the continuum, and the probability of being in the elastic channel is unity.

To determine the probability for transition from the bound state to the continuum through elastic scattering (or other processes), we note that the probability for exciting the ‘‘auto-ionizing’’ state via scattering is proportional to the square modulus of the overlap integral between ϕ and ψ_k ,

$$\left| \int_{-\infty}^{\infty} \phi^*(x) \psi_k(x) dx \right|^2 = 2 \frac{(1 - |\xi|^2)^2}{\beta^2 + k^2} \left[\frac{2\beta - \tilde{\lambda}}{\tilde{\lambda}_c} - \frac{\tilde{\lambda}_c}{2\beta} \right]^2, \quad (3.76)$$

which vanishes when

$$\beta(\tilde{\lambda} - 2\beta) + \frac{\tilde{\lambda}_c^2}{2} = 0, \quad (3.77)$$

that is, when $\beta = [\tilde{\lambda} + \sqrt{\tilde{\lambda}^2 + 4\tilde{\lambda}_c^2}]/4$. This solution is the Fano zero with the experimental signature that the lineshape for excitation of the auto-ionizing state vanishes at the energy E_0 . Therefore, the transmission amplitude, $A + 1$ (see Appendix A) has a zero at $\tilde{\lambda} = 2\beta$.

The location of this zero for small λ_c is given by $E_0 \simeq \Delta - \frac{\hbar^2}{2m} \left[\frac{\tilde{\lambda}^2}{4} + \tilde{\lambda}_c^4 \frac{(\tilde{\Delta} + \frac{\tilde{\lambda}^2}{4})}{16(\tilde{\Delta} - \frac{\tilde{\lambda}^2}{4})^2} \right]$ as compared

to the resonance energy $E_p = \Delta - \frac{\hbar^2}{2m} \left[\frac{\tilde{\lambda}^2}{4} - \tilde{\lambda}_c^4 \frac{(\tilde{\Delta} + \frac{\tilde{\lambda}^2}{4})}{16(\tilde{\Delta} - \frac{\tilde{\lambda}^2}{4})^2} \right]$ and the width $\Gamma = \frac{\hbar^2}{2m} \frac{\tilde{\lambda}\tilde{\lambda}_c^2}{2\sqrt{\tilde{\Delta} - \frac{\tilde{\lambda}^2}{4}}}$. Thus

we find that the Fano parameter $q_F > 0$, and the asymmetric lineshape described generically in Eq. (3.64) emerges in this case.

It is evident from this discussion that the essence of the Fano zero lies in the mixing between the continuum states of the elastic channel and the quasi-bound discrete state of the inelastic channel. The effect of mixing is well expressed by Ugo Fano [77]: ‘‘Repulsion (of levels) is familiar in discrete spectra, when a level of one configuration happens to lie in the midst of a series of levels of other configurations; configuration interaction causes the levels of the second series to be shifted away from the perturbing level. In our situation,

where a discrete level of one series lies in the continuum of another channel, the levels of this continuum are also repelled, but in the sense that their oscillator strength (level densities) is thinned out in the proximity of the perturbing level.” (The phrase in parentheses was added by the authors for increased clarity.) To make this remark more concrete, we write down the effect of the coupling on the density of states of the elastic channel. Note that from Eq. (3.74a) that mixing modifies the plane wave solution by altering the normalization by a factor ξ_k . Hence, the changed density of states due to the auto-ionizing state is given by the multiplicative factor

$$|\xi_k|^2 = 1 - \frac{\frac{\beta\tilde{\lambda}_c^2}{\pi k}}{(2\beta - \tilde{\lambda})^2 + \frac{\tilde{\lambda}_c^2}{4k^2} + \beta\frac{\tilde{\lambda}_c^2}{\pi k}} \leq 1, \quad (3.78)$$

thus reducing the density of states via “level repulsion,” and it is this feature and the Fermi golden rule that leads to the asymmetric lineshape.

3.6.2 Discussion and results :

We have explained the origin of the Fano resonance by a soluble model: the one-dimensional Dirac delta potential. To make the results more transparent, we have taken the elastic channel to correspond to a free particle if it were not coupled to the inelastic channel. Thus nontrivial scattering in the elastic channel occurs only because of the bound state of the inelastic channel, which manifests itself through the typical Fano pole-zero structure. We could have included a direct potential in the elastic channel as well, but this potential would only complicate the algebra without adding anything to the understanding of the relevant mechanism. We also clarified how the amplitudes generate a pole in the fourth quadrant of the second Riemann sheet of the complex energy plane in the elastic unitary cut, and how the excitation function for the auto-ionizing quasi-bound state from the elastic channel develops a zero at some real energy near the resonance. The generic reason for the occurrence of this zero was explained by Fano as arising from the fact that the wave function in the elastic channel has the form $\exp(-ikr) - \exp(2i\delta)\exp(ikr)$, which is $\sin(kr + \delta)$ modulo an over-all phase and irrelevant factors. To find the excitation probability of the quasi-bound state, we have to determine the overlap of this form with a smooth function $g(k, r)$ which varies slowly with respect to k . This overlap is given by $\int \sin(kr + \delta)g(k, r)dr = \cos(\delta)\int \sin(kr)g(k, r)dr + \sin(\delta)\int \cos(kr)g(k, r)dr$. As the energy crosses the Fano resonance, δ changes from $-\pi/2$ to $\pi/2$, and the overlap integral must pass through zero. To make the one-dimensional model also conform to this generic description in terms of phase-shifts, we have adopted the formalism of eigenchannels. We also have demonstrated the modification in the density of states due to the bound state in the continuum. We have argued that the reason for the zero in the elastic amplitude lies with the repulsion of levels due to the bound state of the inelastic channel intruding into the region of purely elastic scattering and the concomitant vanishing of the overlap with this auto-ionizing state. It is necessary to add a word of caution. It may sometimes be very difficult to discriminate between a Fano-resonance and interference effects between a Breit Wigner resonance and a slowly varying background. Consider the latter situation described by an amplitude $f = B(\Gamma/2)/(E - E_r + i\Gamma/2)$ and note that $|f|^2 = B^2 + \frac{\frac{\Gamma^2}{4} + B\Gamma(E - E_r)}{(E - E_r)^2 + \frac{\Gamma^2}{4}}$. The interference term between the resonance

and the background could very well be parametrized by the Fano form with the asymmetry parameter $q = \frac{E_p - E_0}{\frac{\Gamma}{2}} = \frac{1}{B}$. Thus particular attention should be paid to the underlying physical situation vis a vis inelastic channels and bound states in the continuum.

3.6.3 Conclusions

Thus the purpose of this work was to verify FSR in single channel as well as multi-channel Q1D quantum wires in the presence or absence of Fano resonances. Fano resonance is a very general feature of Q1D quantum wires. At the Fano resonance all the quantities are strongly wave vector dependent as it is a purely quantum interference effect. Never the less, FSR is exact at the Fano resonance. This is contrary to the known fact that FSR is valid in semi-classical regimes where there is no strong dependence on wave vector. The exact agreement of the FSR in spite of the strong wave vector dependence is due to the fact that at the Fano resonance there is a quasi bound state that leads to a minimum in the self energy. Away from this quasi bound state there are strong violations. These are true for any negative potential in Q1D and the potential considered here and the associated calculations make this clear. For positive as well as negative delta function potentials, there is also strong wave vector dependence, close to the upper band edge of single channel propagation. This is due to the rapid population of the first evanescent mode at its propagation threshold and does not depend on the existence of Fano resonance. $d\Sigma^a/dE=0$ here because of the perfect transmission at the band edge, and hence the agreement in FSR. So the former case of agreement in the peak is an agreement in purely quantum regime, while that in the case of the latter peak is in the semi-classical regime. Away from the peaks there is always violation. It may be interesting to work out some extended potentials in Q1D [66, 67].

In a multichannel quantum wire with attractive impurities, negative slopes in the scattering phase shift versus incident energy curves can occur at all possible energies. For weaker defects it happens at higher energies and the negative slopes are more pronounced. Such negative slopes mean super luminescence [57, 58] that can be observed experimentally. Although such a super luminescent particle will not give any information about the particle delay or information delay, they are of interest because they demonstrate fundamental principles in quantum mechanics. Hence Eq. (3.60) derived in this paper may be of use to experimentalists and theoreticians. The energy dependence of self energy can be strong except for at band edges or quasi-bound states. Thus energy derivative of Friedel phase does not, in general, give the change in DOS. Unlike 1D, 2D, 3D in Q1D the presence of quasi-bound states play crucial roles even in quantum transports through a simple wires. The FSR in its canonical form (Eq. (3.1)) becomes exact at band edges as well as at strongly quantum regimes such as at quasi-bound states, where Fano resonances occur. The self energy term can be important for fairly large energies (except for at band edges), the so called WKB regimes, making the canonical identity of Eq. (3.1) inexact. In mesoscopic conductors the $\partial\Sigma^a/\partial E$ dependent term in FSR (Eq. (3.14)), in general, is important. We also show that the discontinuous phase drops in the single channel case have a counterpart in the multichannel case wherein the drops can be continuous and we propose a line shape formula for them in Eq. (3.58). When there is a third channel of escape for the electron, apart from the channel along which it is incident and the channel where its scattering phase shift is measured, the phase drop

becomes continuous. However, these phase drops do not affect $\frac{1}{2i} \ln \text{Det}[S]$ and hence Friedel sum rule. Finally, we discuss some novel scattering phase shifts at energies where the S matrix changes dimension.

Chapter 4

Quantum current magnification in a multi-channel mesoscopic ring

In this chapter we study the nonequilibrium effect of quantum current magnification in a Q1D ring connected to reservoirs through leads [24]. So far all studies on current magnification have been restricted to the case of one dimensional (single channel) systems only. Studies on current magnification effect in mesoscopic open rings have been extended to thermal currents [78] and to spin currents in presence of Aharonov-Casher flux [79]. This effect has been studied in the presence of a spin-flip scatterer which causes dephasing of electronic motion [80, 81]. The predicted magnitude of the circulating current densities can indeed be very large [40] and has been termed as ‘giant persistent currents’ [82, 83]. Recently the current magnification effect has been shown to occur in mesoscopic hybrid system at equilibrium in the presence of a magnetic flux and in the absence of transport current [84, 85]. In this chapter we discuss the current magnification in a Quasi-1-dimensional (Q1D) mesoscopic ring. Thus we go beyond the single channel regime to a multi-channel one.

Multi-channel systems are a closer realization to the experimental systems [43, 86] due to their finite width in the transverse direction of propagation of currents. Specifically, we consider a Q1D ring of perimeter L and width W with $L \gg W$ as shown in Fig. 5.10. The two leads that connect this system to the electron reservoirs have the same width as that of the ring. The length of the lower arm of the ring is l_3 while that of the upper arm is $l_1 + l_2$. An impurity δ function potential $V\delta(x - l_1)\delta(y - y_i)$ is embedded in the upper arm. The electrons can propagate freely along the length of the ring and the leads but their motion is confined along the transverse direction. We consider hard wall confinement potential along the transverse direction. Due to this confinement, infinite number of transverse modes are generated in the system. If the energy of the electrons is such that the corresponding wave number is real then the mode is termed as propagating, on the other hand, if the wave number is imaginary it is termed as evanescent. The widths of the ring and the leads being equal, the number of propagating and evanescent modes are same in these two.

We consider non-interacting electrons in the system. The system size is taken to be smaller than the phase coherence length l_ϕ and the phase randomizing inelastic scattering is considered only inside the reservoir. Scattering inside the system maintains the phase

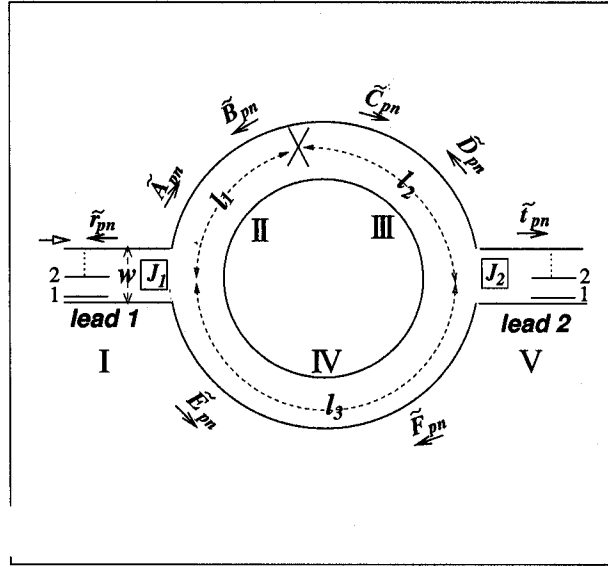


FIGURE 4.1: Schematic diagram of an open multi-channel mesoscopic ring of perimeter $L = l_1 + l_2 + l_3$ connected through the leads 1 and 2 to electron reservoirs (not shown in figure). Both the ring and the leads have the same width W . Several transverse modes are shown by horizontal lines in the leads. A delta function type static scatterer $V_d(x, y) = V(x - l_1)(y - y_i)$ of strength V is shown in the upper arm at \times . ϵ denotes the coupling strength between the leads and the ring.

coherence. This necessitates only static scatterers in the system which in our case are a delta-function potential and junction scatterers at J_1 and J_2 . We neglect all phase randomizing scattering like-phonon interaction inside the system. The left reservoir (S_L) and the right reservoir (S_R) have chemical potentials μ_L and μ_R respectively. When $\mu_L > \mu_R$ current flows from S_L to S_R and vice-versa. We are interested in the linear response regime where currents are related to the transmission across the system at the Fermi energy (Landauer-Büttiker formula, [5]). We consider that the electrons enter the system through the left lead and come out through the right lead. Due to mirror symmetry, results remain the same if the flow of electrons is reversed with the direction of circulating current getting reversed. This ensures absence of circulating current in equilibrium at zero magnetic field.

For no loss of generality we have considered the situation wherein no mode mixing between different transverse modes occur at the junctions. The ring and the lead are connected via junction scattering matrices at J_1 and J_2 . The junction scattering matrices are same for both the junctions J_1 and J_2 . The coupling between either sides of the junction for the modes with same transverse quantum number is given by [87]

$$S_J = \begin{pmatrix} -(a+b) & \sqrt{\epsilon} & \sqrt{\epsilon} \\ \sqrt{\epsilon} & a & b \\ \sqrt{\epsilon} & b & a \end{pmatrix} \quad (4.1)$$

where $a = \frac{1}{2}(\sqrt{1-2\epsilon} - 1)$ and $b = \frac{1}{2}(\sqrt{1-2\epsilon} + 1)$. ϵ is a coupling parameter with values $0 \leq \epsilon \leq 0.5$. When $\epsilon \rightarrow 0$ the system and the reservoir are decoupled while for $\epsilon \rightarrow 0.5$

these two are strongly coupled. This S -matrix satisfies the conservation of current [88]. The above S -matrix is independent of the incident energy and the index of the transverse modes. The presence of the elastic scatterer, namely, δ function potential in the upper arm mixes different propagating and evanescent modes and gives rise to extra phase shift in each mode.

When electrons are injected in the p -th propagating mode, the total wave function in the left lead (region I) is given by

$$\psi|_{\text{I}} = \sqrt{N}e^{ik_p x} \chi_p(y) + \sum_n r_{pn} e^{-ik_n x} \chi_n(y), \quad (4.2)$$

where k_p is the longitudinal wave-vector corresponding to p -th mode along the direction of propagation. Here r_{pn} describes reflection amplitude from p -th to n -th mode, $\chi_n(y)$ represents the n -th transverse mode where y is the coordinate along the transverse direction and \sum_n denotes summation over n including p . The normalization factor \sqrt{N} is determined by noting that the current density injected by the reservoir in a small energy interval dE in the p -th propagating mode is

$$dj_{p_{in}} = ev_p \frac{dn_p}{dE} f(E) dE \quad (4.3)$$

where $f(E)$ is the Fermi distribution function, $\frac{dn_p}{dE} = \frac{2}{\hbar v_p}$ is the density of states (DOS) in the perfect wire and $v_p = \frac{\hbar k_p}{m_e}$. For our zero temperature calculations $f(E) = 1$ for occupied states. The wave function $\psi_p|_{\text{I}}$ gives the incident current density $dj_{p_{in}} = \frac{2e}{\hbar} dE$, which in turn is independent of the propagating mode in which the electron is incident if $N = \frac{2e}{\hbar v_p} dE$. Here dE denotes an energy interval around Fermi energy and hence change in incident energy would mean a change in the Fermi energy of electrons emanating from the reservoirs.

The wave functions in all other regions are

$$\psi|_{\text{II}} = \sum_n (A_{pn} e^{ik_n x} + B_{pn} e^{-ik_n x}) \chi_n(y) \quad (4.4)$$

$$\psi|_{\text{III}} = \sum_n (C_{pn} e^{ik_n x} + D_{pn} e^{-ik_n x}) \chi_n(y) \quad (4.5)$$

$$\psi|_{\text{IV}} = \sum_n (E_{pn} e^{ik_n x} + F_{pn} e^{-ik_n x}) \chi_n(y) \quad (4.6)$$

$$\psi|_{\text{V}} = \sum_n t_{pn} e^{ik_n x} \chi_n(y) \quad (4.7)$$

where n stands for all available propagating modes including p .

S_J connects the incoming and outgoing amplitudes of the p -th mode at J_1 via

$$\begin{pmatrix} r'_{pp} \\ A'_{pp} \\ E'_{pp} \end{pmatrix} = S_J \begin{pmatrix} 1 \\ B'_{pp} \\ F'_{pp} \end{pmatrix} \quad (4.8)$$

where any new amplitude A'_{pn} is connected to its earlier definition A_{pn} by

$$A'_{pn} = \sqrt{v_p} \sqrt{\frac{\hbar}{2e}} (\sqrt{dE})^{-1} A_{pn}$$

In further calculations all the amplitudes with primes carry the same meaning as above. S_J connects the incoming and outgoing amplitudes of all the other propagating modes m ($m \neq p$) at J_1 via

$$\begin{pmatrix} r'_{pm} \\ A'_{pm} \\ E'_{pm} \end{pmatrix} = S_J \begin{pmatrix} 0 \\ B'_{pm} \\ F'_{pm} \end{pmatrix} \quad (4.9)$$

Similarly, the incoming amplitudes $(0, C'_{pn}, E'_{pn})$ and outgoing amplitudes $(t'_{pn}, D'_{pn}, F'_{pn})$ at the junction J_2 are connected via the same scattering matrix S_J .

The elastic scattering at the impurity is described by

$$\begin{pmatrix} B'_{p1} e^{-ik_1 l_1} \\ B'_{p2} e^{-ik_2 l_1} \\ \dots \\ \dots \\ B'_{pP} e^{-ik_P l_1} \\ C'_{p1} \\ C'_{p2} \\ \dots \\ \dots \\ C'_{pP} \end{pmatrix} = \tilde{S} \begin{pmatrix} A'_{p1} e^{ik_1 l_1} \\ A'_{p2} e^{ik_2 l_1} \\ \dots \\ \dots \\ A'_{pP} e^{ik_P l_1} \\ D'_{p1} \\ D'_{p2} \\ \dots \\ \dots \\ D'_{pP} \end{pmatrix} \quad (4.10)$$

$$\text{where } \tilde{S} = \begin{pmatrix} \tilde{R} & \tilde{T} \\ \tilde{T} & \tilde{R} \end{pmatrix}$$

and both \tilde{R} and \tilde{T} are matrices of order $P \times P$, P being the maximum number of propagating modes in the system depending on a given Fermi energy. These matrices \tilde{R} and \tilde{T} can be expressed in terms of matrix elements \tilde{r}_{mn} and \tilde{t}_{mn} respectively, where

$$\tilde{r}_{mn} = \frac{-i \frac{\Gamma_{mn}}{2\sqrt{k_m k_n}}}{1 + \sum_j^e \frac{\Gamma_{jj}}{2\kappa_j} + i \sum_j^p \frac{\Gamma_{jj}}{2k_j}}$$

with $1 \leq m, n \leq P$. The indices m and n denote propagating modes. \sum^e represents a sum over all the evanescent modes and \sum^p represents a sum over all the propagating modes. The inter-mode (i.e. $m \neq n$) transmission amplitudes are $\tilde{t}_{mn} = \tilde{r}_{mn}$ and intra-mode transmission amplitudes are $\tilde{t}_{nn} = 1 + \tilde{r}_{nn}$. For details see Ref. [60]. Γ_{mn} can be calculated using

$$\Gamma_{mn} = \frac{2m_e V}{\hbar^2} \chi_n^*(y_i) \chi_m(y_i).$$

In Eq. 4.10, while writing A'_{pn}, B'_{pn} the origin is taken to be at the junction J_1 whereas in writing C'_{pn}, D'_{pn} the origin is taken to be at the scatterer. For details of the S -matrix elements for a multi-channel scattering problem see Ref. [60]. Note that the different elements of the S -matrix contain informations about the propagating modes as well as all the infinite number of evanescent modes arising out of transverse confinement [60].

For any given incident electron in the p -th mode in the lead with energy E the current in the n -th mode in region II is given by

$$\begin{aligned} dj_{p,nLU} &= v_n (|A_{pn}|^2 - |B_{pn}|^2) \\ &= (|A'_{pn}|^2 - |B'_{pn}|^2) \frac{2e}{h} \end{aligned} \quad (4.11)$$

Currents in all the other portions of the ring can be calculated similarly. The partial current densities $dj_{p,nLU}$ are obtained after integrating the local currents along the transverse y -direction. If $dj_{p,n}$ is the current density in the n -th propagating mode in any segment of the system then the total current in that segment is given by

$$dj = \sum_{p=1}^P dj_p(s) = \sum_{p=1}^P \sum_{n=1}^P dj_{p,n} \quad (4.12)$$

where ‘ p ’ denotes the propagating mode in which the electrons are injected from the reservoir.

We use scattering matrices at the two junctions and at the scatterer site, \times , to calculate all the amplitudes and then find out the total current density (dj_T), the current density in the upper arm (dj_U) as well as that in the lower arm (dj_L). Thus

$$\begin{aligned} dj_T &= \sum_{p=1}^P \sum_{n=1}^P |\tilde{t}_{pn}|^2 \frac{2e}{h} \\ &= \sum_{p=1}^P \left(1 - \sum_{n=1}^P |\tilde{r}_{pn}|^2\right) \frac{2e}{h} \end{aligned} \quad (4.13)$$

We study these currents as a function of the incident electron energies.

4.1 results and discussions

The circulating current density dj_c is the magnitude of the negative part of dj_U or dj_L as mentioned earlier. When dj_U is negative the direction of circulating electron current is anticlockwise (negative) and when dj_L is negative then it is clockwise (positive). A circulating current in a loop gives rise to an orbital magnetic moment (Ampere’s law). By our convention, positive dj_c indicates an ‘up’ or positive magnetic moment whereas negative dj_c indicates a ‘down’ or negative one. We plot all the current densities in the units of incident current density $dj_{in} = \frac{2e}{h} dE$ and all the energies in the units of ground state energy of the transverse modes, $E_0 = \frac{\pi^2 \hbar^2}{2m_e W^2}$. In all our calculations we have considered 500 evanescent modes. Increasing the strength of the impurity potential causes the coupling of higher number of evanescent modes and hence for large impurity potential strengths one need to incorporate larger number of evanescent modes.

We first study the case for which the system is weakly coupled with the leads (Fig. 4.2). This coupling can be controlled by changing the values of ϵ appropriately. All the physical parameters are indicated in the figure caption. The upper and lower arms of the ring have

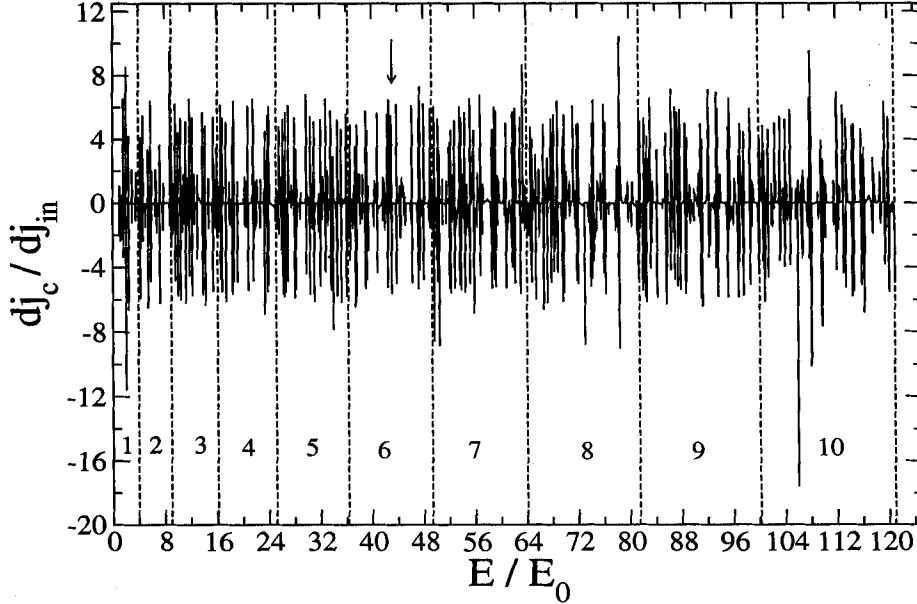


FIGURE 4.2: Plot of the circulating current density dj_c/dj_{in} in the ring as a function of E/E_0 of the electron. In the whole energy range, we have 1 to 10 propagating modes (corresponding energy-ranges are indicated by vertical dashed lines). The different system parameters are $l_1 = 3.5$, $l_2 = 2.5$, $l_3 = 4.0$, $W = 1$, $2m_e V/\hbar^2 = 1$, $y_i = 0.21W$, $\epsilon = 0.2$.

different lengths. From the plot of the circulating current density vs. energy (Fig. 4.2) we observe that there is current magnification of almost same magnitude with similar frequency of occurrence over the entire energy range. The total number of propagating modes in the lead incident on the ring vary throughout this energy scale from one to ten as indicated in Fig. 4.2.

Number of propagating modes in the lead and the ring are same. Between different propagating modes there are several resonances around which current magnification takes place [39, 40]. These resonances approximately occur around $E_r = \left(\frac{\hbar^2}{2m_e}\right)\left(\frac{2r\pi}{L}\right)^2$, where E_r are the energy eigenvalues of the isolated ring of length L . The small deviation of resonances from these values is due to multi-channel nature of our problem along with the impurity potential which causes mode mixing. When there are, say, ten propagating modes, to obtain total current in the upper arm we have to add hundred values of partial currents [Eq. 4.12] due to different modes. Though individual partial current density shows oscillatory behavior the magnitude of the total circulating current in multi-channel regime remains of the same order of magnitude as it is when only one mode is propagating in the system. This can be explicitly seen in Fig. 4.2 throughout the energy range with one to ten propagating modes. This clearly indicates that current magnification effect is robust even in multi-channel systems despite the contributions from several propagating modes and mode mixing. To see the mode mixing and the cancellation effects we have considered the case where there are four propagating modes in Fig. 4.3. Hence to obtain total current in the upper arm we have to calculate sixteen partial currents [Eq.4.12]. In Fig. 4.3, for simplicity instead of considering sixteen partial currents we

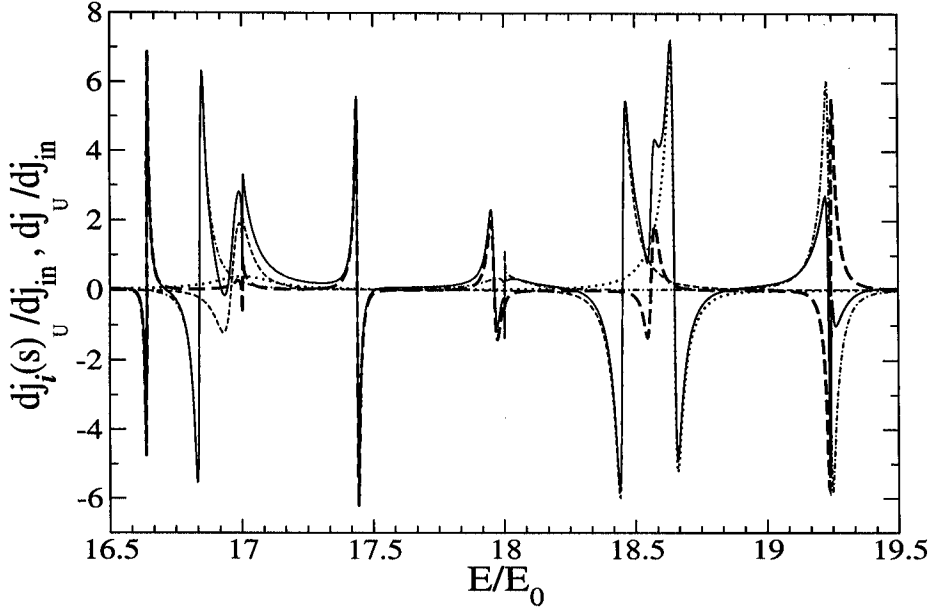


FIGURE 4.3: Plots of different partial current densities $dj_i(s)_U/dj_{in}$ and the total current in the upper arm of the ring as a function of E/E_0 . The dotted curve gives $dj_1(s)_U/dj_{in}$, the dashed curve gives $dj_2(s)_U/dj_{in}$, the dash-dotted curve gives $dj_3(s)_U/dj_{in}$, the long-dashed one is for $dj_4(s)_U/dj_{in}$ and the solid one is for dj_U/dj_{in} . In the above energy range we have 4 propagating modes. The different system parameters are $l_1 = 3.5$, $l_2 = 2.5$, $l_3 = 4.0$, $W = 1$, $2m_eV/\hbar^2 = 1$, $y_i = 0.21W$, $\epsilon = 0.2$.

have plotted four values of current densities $dj_1(s)_U$, $dj_2(s)_U$, $dj_3(s)_U$, $dj_4(s)_U$ and total current dj_U . Here $dj_i(s)_U = \sum_{n=1}^4 dj_{i,n}$, $i = 1, 2, 3, 4$. $dj_{i,n}$ is sum over partial current densities in the four propagating modes in the upper arm when electron is incident in the i -th propagating mode. Total current in the upper arm is given by $dj_U = dj_1(s)_U + dj_2(s)_U + dj_3(s)_U + dj_4(s)_U$. Negative currents in this graph represents the existence of circulating current in partial current densities. Each $dj_i(s)_U$ show oscillatory and complex pattern. The total current dj_U still exhibits negative part (current magnification) in spite of cancellation effects arising due to mode mixing.

To see in detail the nature of current magnification vis-a-vis total transport current in lead we consider a case where there is only one propagating mode (Fig. 4.4(a)) and separately another case wherein number of propagating modes are ten (Fig. 4.4(b)). In these figures we have plotted the total transport current and circulating currents as a function of Fermi energy with the other parameters as mentioned in figure caption. We see a current magnification whenever there is a partial minimum in the total current that flows through the system which in turn is measured at the leads. This phenomenon of current magnification at Fano type line-shapes of total current is consistent with earlier observations seen in the case of one dimensional system [39]. Though from a first look in the range $1.8E_0 < E < 2.2E_0$ in Fig. 4.4(a) it appears that we have current magnification near a total-current maximum, a closer scan reveals that there is indeed a very sharp Fano-type asymmetric

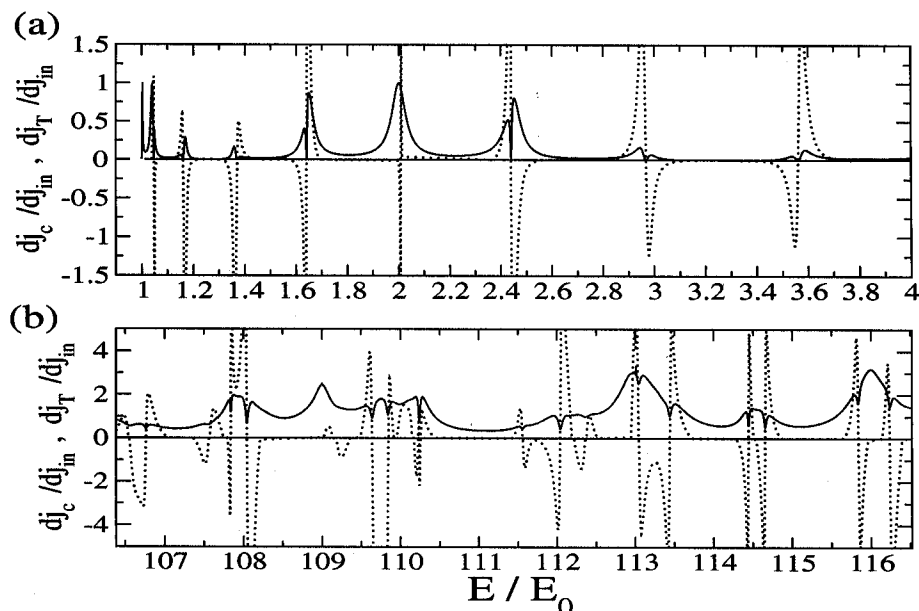


FIGURE 4.4: Plot of the circulating current dj_c/dj_{in} (dotted lines) and the total current dj_T/dj_{in} (solid lines). Both the functions are plotted versus E/E_0 . The different system parameters are $l_1 = 3.5$, $l_2 = 2.5$, $l_3 = 4.0$, $W = 1$, $2m_e V/\hbar^2 = 1$, $y_i = 0.21W$, $\epsilon = 0.2$.

maxima-minima line-shape at this point. When only one channel is propagating the total current is proportional to the transmission coefficient [5]. A closer look at these minima shows that we obtain current magnification of either sign around every maxima-minima pair in total current. In Ref. [39, 82, 83] the current magnification of a pure 1D quantum ring having no impurity has been related to Fano resonance (asymmetric zero-pole structure) in the transmission coefficient. In multi-channel transmission Fano zero-pole line shape gets replaced by an asymmetric maximum-minimum line-shape [22]. We found this Fano type asymmetric maxima-minima line-shape at each energy point of current magnification shown in Fig. 4.2. At current magnification the presence of a quasi-bound state of circulating current in the ring gives rise to this Fano-type line-shape to the total current. The circulating current changes sign more sharply and shows stronger current magnification where Fano line-shape is sharper and narrower. This feature is somewhat equivalent to the classical parallel LCR resonant circuit in which the higher Q -values indicate higher current magnification and sharper minimum at resonant frequencies. These features remain intact for the whole energy scale even if there are more than one propagating modes contributing (see Fig. 4.4(b)).

For a symmetric ring ($l_1 + l_2 = l_3$) we observe (Fig. 4.5) lesser occurrence-frequency of the current magnification throughout this same energy scale. This is understandable as in the absence of any impurity and magnetic field an asymmetric 1D ring shows current magnification [39], meaning that asymmetry in length ratios of a ring favors this effect. Pareek *et al.* [40] have shown that for a 1D ring one can have regions of incident energies where current magnification gets enhanced with the increase in the impurity potential strength. We investigate this effect for the case of our multi-channel ring. In order to compare with Ref. [40]

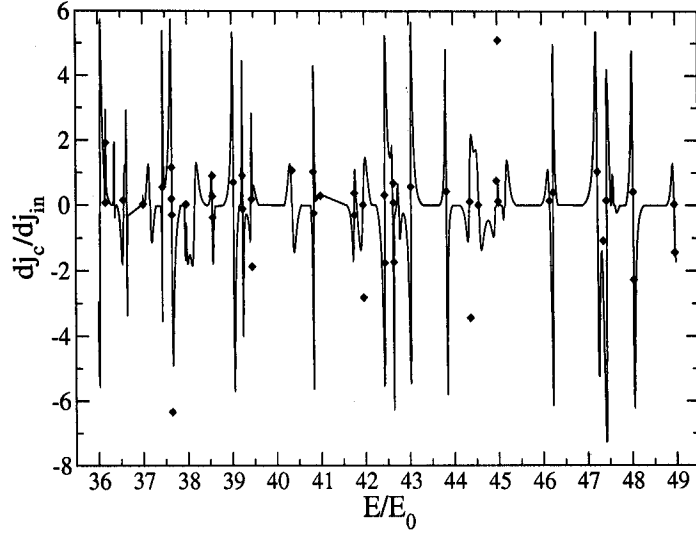


FIGURE 4.5: Plot of circulating current density dj_c/dj_{in} in the ring as a function of E/E_0 of the electron for 6 propagating modes. The solid curve is for $l_1 = 3.5$, $l_2 = 2.5$, $l_3 = 4.0$ while the diamond shaped points are for $l_1 = 3.5$, $l_2 = 1.5$, $l_3 = 5.0$. From figure it is clear that current magnification greatly reduces for ring with equal length of upper and lower arms. Other system parameters are $W = 1$, $y_i = 0.21W$, $2m_eV/\hbar^2 = 1$ and $\epsilon = 0.2$.

we have calculated the effects of potential using Griffith's boundary condition or coupling parameter $\epsilon = 4/9$ at the junctions. In Fig. 4.6 and Fig. 4.7 we have shown the variation of the current magnification for two different peaks in the appropriate energy ranges. Fig. 4.6 is for single channel case while Fig. 4.7 is for two channel. From Fig. 4.6(a) and Fig. 4.7(a) we notice that the current magnification effect get enhanced with the increase in strength of the impurity potential while the opposite is true for the case considered in Fig. 4.7(b). A closer look at Fig. 4.6(b) reveals that peak in the negative part of the circulating current density first increases and then decreases as we vary continuously the strength of the impurity potential. Thus impurities in the system can either enhance or decrease the current magnification effect. The enhancement of the circulating current densities is a counter-intuitive effect, in the light of the fact that impurity generally degrades the transport current in the system.

It might be interesting to note that a negative delta-function potential is capable of providing one bound state having energy $\sim m_eV^2/(2\hbar^2W^2)$. Our choice of V is such that $2m_eV/\hbar^2 \sim 1$. This corresponds to a binding energy $\sim 10^{-4}eV$ when $W \sim .2\mu m$ [89]. This binding energy or the ionization energy due to impurity, in general, should be much less than the free atomic binding energy ($\sim eV$) due to the dielectric screening and the smaller electron effective mass [91] than the free electron mass. This criterion is indeed held by our choice of potential indicating it's feasibility. Moreover our choice of the length ratios $(l_1+l_2) : l_3 : W$ are similar to that used in experimental situations [43, 89]. We have checked that the general feature of occurrences of very closely spaced regions of current magnification of similar magnitudes in the whole energy window (Fig. 4.2) does not alter with change in each of the quantities l_1/l_2 , $(l_1+l_2)/l_3$, y_i/W , W/L or $2m_eV/\hbar^2$ one at a time keeping rest

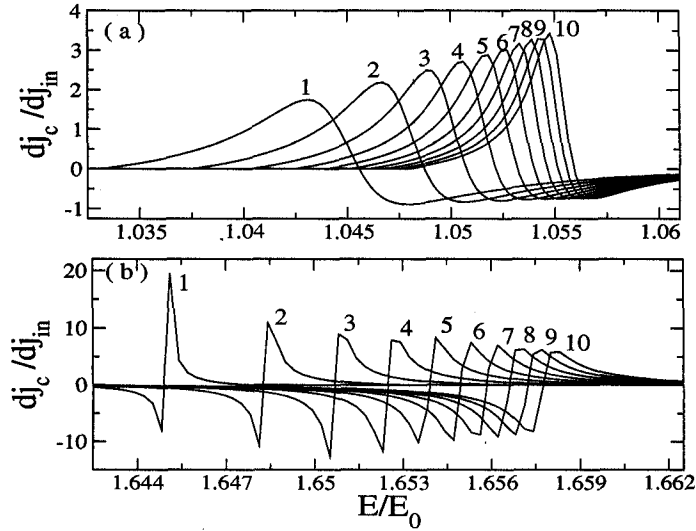


FIGURE 4.6: Plots of circulating current dj_c/dj_{in} versus incident energy E/E_0 in the range of single mode propagation. Curves 1, 2, 3, 4, \dots , 10 are for potential strengths $2m_eV/\hbar^2 = 0.5, 1.0, 1.5, 2.0, \dots, 5.0$ respectively. The other system parameters are $l_1 = 3.125$, $l_2 = 3.125$, $l_3 = 3.75$, $W = 1$, $y_i = 0.21W$, $\epsilon = 4/9$.

of the parameters fixed. In particular, the shift in position of the defect potential does not change the properties of current magnification. In Fig. 4.8 we shift the impurity along the upper arm of the ring keeping its y -coordinate fixed and in Fig. 4.9 we shift the impurity along the width of the ring keeping its x -coordinate fixed. It is clear from that Fig. 4.8 and Fig. 4.9 neither the magnitude nor the occurrence frequency of current magnification in energy scale depend on the position of impurity potential. But, as discussed earlier, the change in strength of the defect potential or the asymmetry of two arm-lengths may change the magnitudes and positions of current magnification in energy scale, keeping the general feature unaltered. As $(l_1 + l_2)/l_3 \rightarrow 1$ occurrence frequency of current magnification becomes smaller. For $2m_eV/\hbar^2 = 0$ or $y_i/W = \pm 1/2$ the mode coupling constant $\Gamma_{mn} = 0$ and the modes get decoupled and as expected, current magnification remaining robust becomes similar to single channel problem. Interestingly, staying within phase coherence length if we double the L/W ratio, the amplitude of dj_c does not decrease while occurrence frequency becomes larger as the resonance spacings $(\Delta E_r/E_0 \sim (W/L)^2)$ become smaller. This is shown in Fig. 4.10. Doubling the L naturally means quadrupling the magnetic moment as it scales with area. It would be worthy to mention that unlike current magnification, amplitude of persistent currents decreases as $1/L^2$.

Büttiker [87] has shown that when the ring is threaded by a magnetic flux Φ , as the coupling goes towards the strong coupling regime ($\epsilon \rightarrow 0.5$) the amplitude of persistent current reduces due to increased dephasing. This is a quantitative change in persistent current due to broadening of energy levels with increasing coupling strength. To examine the effect of system-reservoir coupling strength on current magnification in multi-channel ring in absence of Φ , we have calculated circulating current for $\epsilon = 0.48$. We observe that the

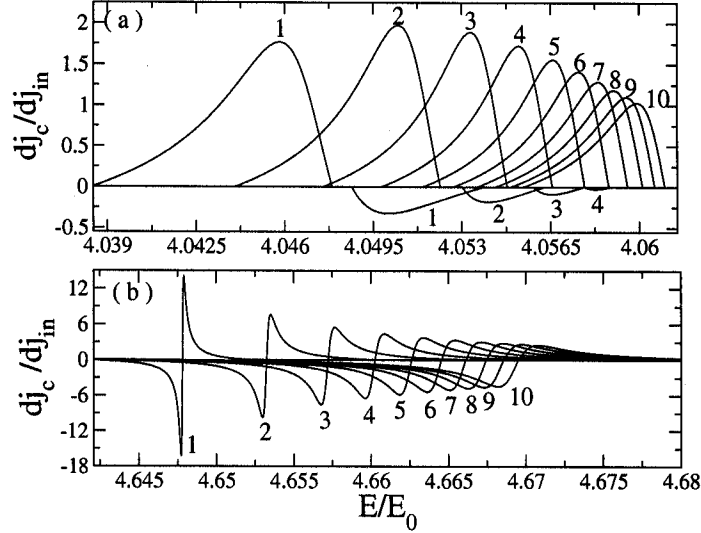


FIGURE 4.7: Plots of circulating current dj_c/dj_{in} versus incident energy E/E_0 in the range of two mode propagation. Curves 1, 2, 3, 4, \dots , 10 represent potential strengths $2m_eV/\hbar^2 = 0.5, 1.0, 1.5, 2.0, \dots, 5.0$ respectively. The other system parameters are $l_1 = 3.125$, $l_2 = 3.125$, $l_3 = 3.75$, $W = 1$, $y_i = 0.21W$, $\epsilon = 4/9$.

frequency of current magnification as well as the magnitude of circulating currents reduce significantly in the whole energy range (Fig. 4.11) compared to that observed in Fig. 4.2. This indicates that in Q1D coupling strength alters the nature of current magnification effect in a non-trivial manner. The total current magnification in the ring is due to a summation over current magnifications corresponding to each incident mode allowed for a given incident energy. As we increase the coupling strength ϵ , we observe that the contribution to current magnification from electrons injected in each incident mode goes from a narrower and stronger to a broader and weaker shape with respect to the corresponding energies (Fig 4.12). The broader they get, the more cancellation of current magnification occurs due to overlap of different incident modes. In Fig. 4.13 we have shown contributions from first and second incident modes in the upper arm of the ring when only two modes are propagating. In this energy range we observe current magnification for $\epsilon = 0.2$ (upper graph) but absence of current magnification for $\epsilon = 0.48$ (lower graph). From lower graph ($\epsilon = 0.48$) it is evident that though the contribution of current due to incident mode-1 (dashed line) is negative and thus should give rise to current magnification, the contribution from incident mode-2 (dotted line) cancels it off and we observe no net current magnification in this energy range. From the upper graph ($\epsilon = 0.2$) it is clear that in the energy range where contribution of current due to incident mode-1 (dashed line) is negative, the contribution from incident mode-2 (dotted line) is almost zero as the contribution to current magnification from each incident mode is very sharp for low ϵ -values. Hence we obtain a net current magnification in this energy range for $\epsilon = 0.2$ though current magnification is absent for $\epsilon = 0.48$ in the same energy range. Thus system-reservoir coupling strength alters current magnification effect in a multi-channel mesoscopic ring not only quantitatively, but it also has a strong qualitative

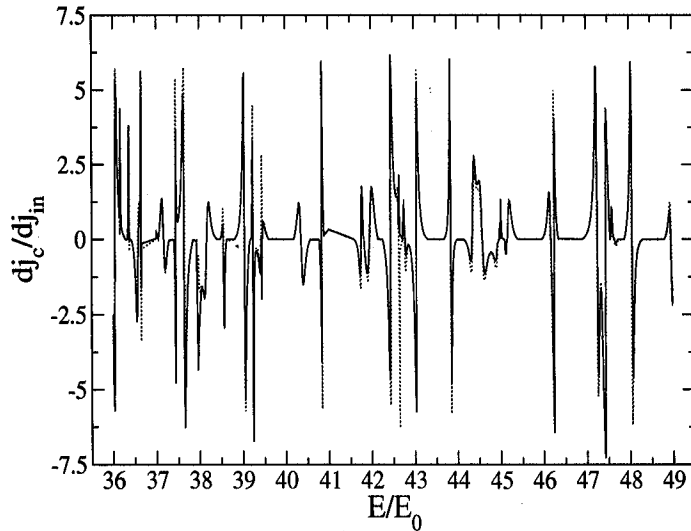


FIGURE 4.8: Plot of circulating current density dj_c/dj_{in} in the ring as a function of E/E_0 of the electron for 6 propagating modes. The dotted curve is for $l_1 = 3.5$, $l_2 = 2.5$ while the solid one is for $l_1 = 0.5$, $l_2 = 5.5$. Other system parameters are $l_3 = 4.0$, $W = 1$, $y_i = 0.21W$, $2m_eV/\hbar^2 = 1$ and $\epsilon = 0.2$.

effect. The stronger the coupling the weaker and lesser is the current magnification in any energy scale. As for energies where higher number of modes are propagating and number of cancellations of current magnification is also high we obtained even lesser current magnifications and their occurrence frequency in the energy axis are also reduced (Fig. 4.11). This effect is entirely due to the superposition of currents from all the different channels which is absent in purely 1D system. The non-trivial effect of system-reservoir coupling on the equilibrium currents in 1D quantum double ring system has been discussed recently in Ref. [90].

We now consider the case of an attractive δ function potential ($V < 0$). We see in Fig. 4.14 that in the stronger coupling regime ($\epsilon = 0.48$) the amplitude of current magnification for attractive potential is lesser in comparison to the repulsive one (Fig. 4.11). The magnitudes and the positions of the current peaks are very sensitive to the details of some of the system parameters and they can not be predicted a priori. Moreover, the current magnification effect is always absent at the quasi-bound state of the negative potential (Fig. 4.14). The energies of the quasi-bound states are marked by arrows in Fig. 4.14. These states are characterized by peaks in the density of states (DOS) and for further discussion on quasi-bound state see Ref. [21, 22, 60]. The presence of negative delta-function potential enhances DOS near this potential. This enhanced local DOS at the impurity site reduces the DOS of the propagating electrons, thereby reducing the current magnification.

In Fig. 4.15 we have considered a special case and plotted the total transport current density dj_T and circulating current density dj_c in the energy range $4.6E_0 < E < 5.4E_0$. In this energy range at the Fermi energy there are two propagating modes. The corresponding bound-state is at $5.1025E_0$. Around the bound-state there is an enhancement in scattering.

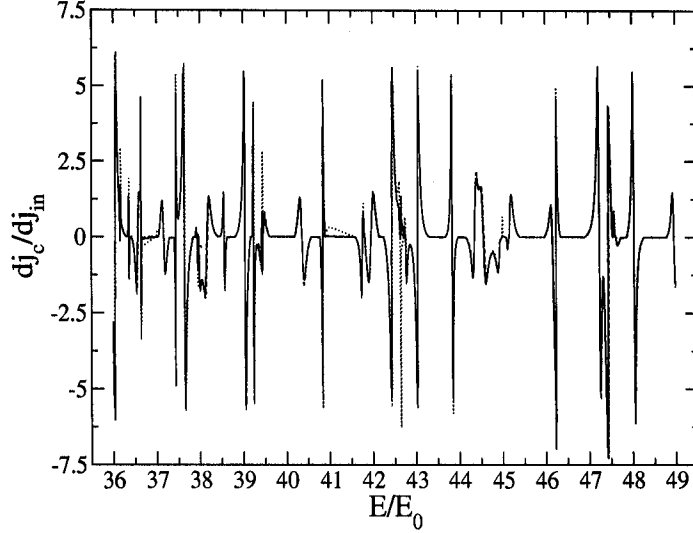


FIGURE 4.9: Plot of circulating current density dj_c/dj_{in} in the ring as a function of E/E_0 of the electron for 6 propagating modes. The solid, dotted and dashed curves are for $y_i = 0.5W$, $0.21W$, 0 respectively. Other system parameters are $l_1 = 3.5$, $l_2 = 2.5$, $l_3 = 4.0$, $W = 1$, $y_i = 0.21W$, $2m_eV/\hbar^2 = 1$ and $\epsilon = 0.2$.

The structure of the total transport current exhibits symmetric line shapes (like Breit-Wigner type symmetric resonances). Around these resonances we do observe current magnification. This special case shows that Fano type resonance structure in the total transport current is not a necessary criterion for the observation of current magnification effect.

4.2 Possible Experiment

We have seen that only for a certain but large number of parameter values, circulating currents appear in the ring. Such circulating currents will be associated with a magnetic moment that can be determined by a SQUID or a Hall magnetometer placed on above or below the ring. The magnetic moment will be $j_c A$, where A is the area enclosed by the ring. j_c will be related to dj_c by $\int_{\mu_R}^{\mu_L} dj_c(E)$. When there is no circulating current (current in the two arms flow in the same direction) there will be negligible magnetic moment. We have seen in Fig. 4.2 and Fig. 4.10, regions of current magnification occur very close to each other in an apparently random order and by tuning any one parameter (Fermi energy or defect strength) while keeping other parameters fixed there is a high probability of observing current magnification. The parameters to tune are μ_L , μ_R and the strength of the defect. Instead of tuning μ_L , μ_R one can fix them and chose any Fermi energy of the system by applying an electric field perpendicular to the geometry by using some overall gate. In an experimental situation the tip of an STM can be used to create a defect of any desired strength in one arm by depleting the electron gas under the tip. Alternatively, a defect of desired strength can be produced by fabricating a small gate on top of one of the arms of

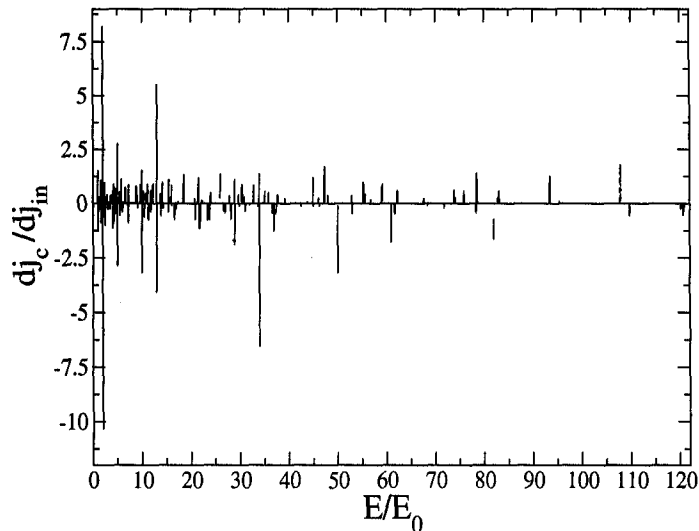


FIGURE 4.10: Plots of circulating current dj_c/dj_{in} versus incident energy E/E_0 . In this regime six modes are propagating. The dotted curve is for $L/W = 20$ while solid one is for $L/W = 10$. The other system parameters are $W = 1$, $l_1 : l_2 : l_3 = 7 : 5 : 8$, $y_i = 0.21W$, $2m_eV/\hbar^2 = 1.0$ and $\epsilon = 0.2$.

the ring, and applying a voltage on it perpendicular to the plane of the ring. We have taken some typical cases of rings fabricated in the laboratory in recent experiments such as that in ref. [43, 89]. These rings have L/W in between that considered in Fig. 4.2, Fig. 4.10. In experiments the rings that are mainly used are made of GaAs where effective electron mass is $0.067m^*$ [91], m^* being the electron mass. Using this the peaks in the circulating current j_c come out to be of the same order of magnitude as that of the zero temperature persistent current. For example, integrating dj_c over an interval of $\mu_L = 43.04E_0 < E < 43.32E_0 = \mu_R$ with $\mu_L - \mu_R = .28E_0 \sim 39 \times 10^{-6}eV$ ($\sim \Delta E_r$) at the marked (\downarrow) peak in Fig. 4.2 we find $j_c \sim 3.69nA$ for $W = .2\mu m$ [89] and the corresponding orbital magnetic moment is $\sim 127\mu_B$ where $\mu_B = \text{Bohr magneton}$. This magnetic moment remains of the same order of magnitude at all peaks of Fig. 4.2. So with present day detectors like SQUIDs and Hall magnetometers one can definitely detect the magnetic moments due to current magnification.

4.3 conclusion

In conclusion, we have shown that, even in the multi-channel case, for a system weakly coupled with the reservoirs the current magnification in the presence of transport current is a robust effect. The magnitude of the circulating current can be very large even in presence of several propagating modes despite mode mixing and cancellation effects as discussed in the text. The circulating currents are mostly associated with Fano resonances in total transport current. However, there are, sometimes, exception to this rule, namely, current magnification may occur around Breit-Wigner type symmetric resonances in the total current. Unlike

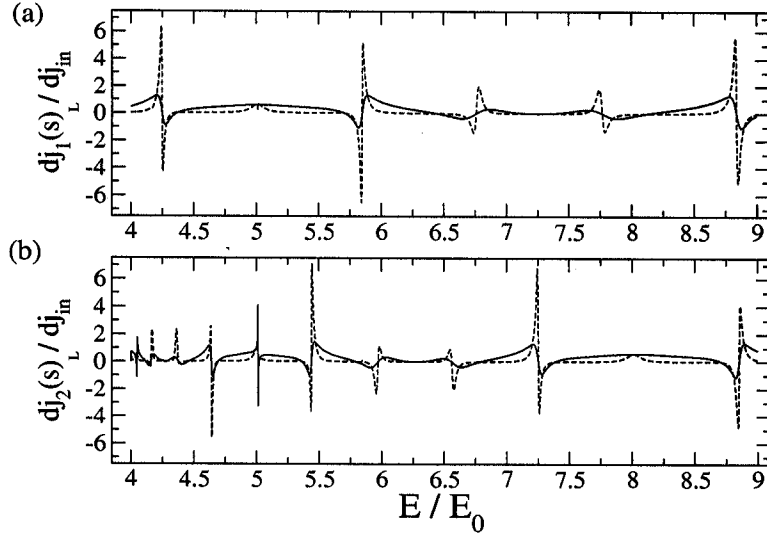


FIGURE 4.11: The circulating current dj_c/dj_{in} versus E/E_0 is plotted for repulsive potential $2m_eV/\hbar^2 = 1$ in strong coupling regime $\epsilon = 0.48$. The different system parameters are $l_1 = 3.5$, $l_2 = 2.5$, $l_3 = 4.0$, $W = 1$, $y_i = 0.21W$.

purely one dimensional systems Fano resonance does not exhibit zero in the total transmission, however, it is characterized by a sharp minimum along with asymmetric line shape in the total current. Impurity strength can enhance or suppress current magnification and is sensitively dependent on system parameters. We have established that the system-reservoir coupling strength controls the current magnification qualitatively. As the coupling becomes stronger the current magnification becomes weaker and its occurrence in the given energy range reduces. Thus system reservoir coupling parameter controls the transport properties in a very interesting manner. It is interesting to note that persistent currents in a ballistic mesoscopic ring in the presence of magnetic flux increases with the Fermi energy (or the number of channels) [34, 87, 92, 93]. In contrast the magnitude of the current magnification is independent of the total number of propagating channels. It may be emphasized that persistent currents and the circulating currents due to current magnification are two independent distinct phenomena [41, 94].

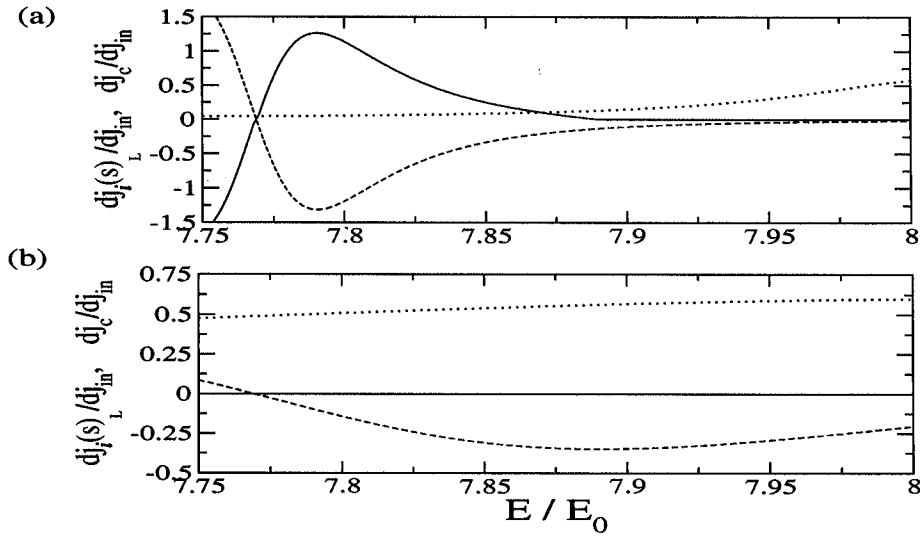


FIGURE 4.12: In (a) the partial current $dj_1(s)_L/dj_{in}$ and in (b) the partial current $dj_2(s)_L/dj_{in}$ in the lower arm of the ring are plotted as a function of E/E_0 . In both (a) and (b) dashed curves are for $\epsilon = 0.2$ and the solid curves are for $\epsilon = 0.48$. The other system parameters are $l_1 = 3.5$, $l_2 = 2.5$, $l_3 = 4.0$, $W = 1$, $2m_e V/\hbar^2 = 1$, $y_i = 0.21W$.

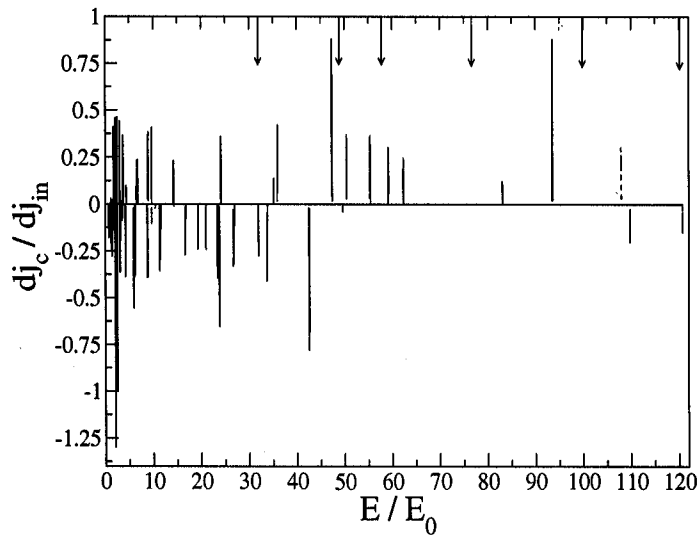


FIGURE 4.13: Both in (a) and (b), the dashed curve gives the partial current $dj_1(s)_L/dj_{in}$, the dotted curve gives the partial current $dj_2(s)_L/dj_{in}$ in the lower arm of the ring and the solid curve gives the circulating current dj_c/dj_{in} in the ring. All three quantities are plotted as a function of incident energy E/E_0 of the electron. (a) is for weak coupling $\epsilon = 0.2$ while (b) is for strong coupling $\epsilon = 0.48$. Other system parameters are $l_1 = 3.5$, $l_2 = 2.5$, $l_3 = 4.0$, $W = 1$, $2m_e V/\hbar^2 = 1$, $y_i = 0.21W$.

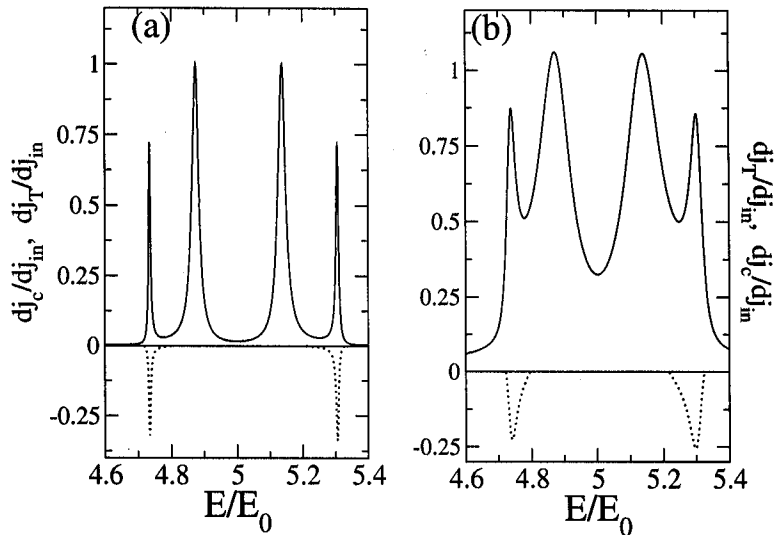


FIGURE 4.14: The circulating current dj_c/dj_{in} vs. E/E_0 is plotted for strong coupling $\epsilon = 0.48$ and attractive potential $2m_e V/\hbar^2 = -2.5$. The arrows on the graph denote the positions of different quasi-bound-states in the available energy range, $31.87 E_0, 49 E_0, 57.7 E_0, 76.53 E_0, 100 E_0, 120.12 E_0$. The other system parameters are $l_1 = 3.5$, $l_2 = 2.5$, $l_3 = 4.0$, $W = 1$, $y_i = 0.21W$.

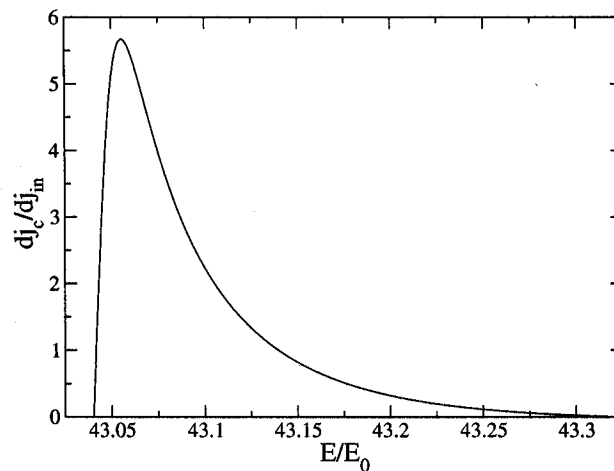


FIGURE 4.15: dj_T/dj_{in} (solid curve) and dj_c/dj_{in} (dotted curve) are plotted as a function of E/E_0 for coupling strengths(ϵ) 0.05 ((a)) and 0.2 ((b)) in presence of two propagating modes. Other system parameters are $l_1 = 2.5$, $l_2 = 1.5$, $l_3 = 3.0$, $W = 1$, $2m_e V/\hbar^2 = -2.4$, $y_i = 0.21W$. The quasi-bound-state is at $5.1025 E_0$.

Chapter 5

Phase time *for* tunneling particle

5.1 Introduction

Quantum tunneling, where a particle has finite probability to penetrate a classically forbidden region is an important feature of wave mechanics. Invention of the tunnel diode [95], the scanning tunneling microscope [96] etc. made it useful from a technological point of view. In 1932 MacColl [97] pointed out that tunneling is not only characterized by a tunneling probability but also by a time the tunneling particle takes to traverse the barrier. There is considerable interest on the question of time spent by a particle in a given region of space [58, 105?]. The recent development of nanotechnology brought new urgency to study the tunneling time as it is directly related to the maximum attainable speed of nanoscale electronic devices. In addition recent experimental results claiming superluminal tunneling speeds for photons [99, 100] boost the urgency. In a number of numerical [101], experimental [99, 102] and analytical study of quantum tunneling processes, various definitions of tunneling times have been investigated. These different time scales are based on various different operational definitions and physical interpretations. Till date there is no clear consensus about the existence of a simple expression for this time as there is no hermitian operator associated with it [58]. Furthermore, a corpuscular picture of tunneling is very hard to be realized due to the lack of a direct classical limit for the tunneling particle's trajectories and velocities. Among the various time scales, 'dwell time' [57] which gives the duration of a particle's stay in the barrier region regardless of how it escapes can be calculated as the total probability of the particle inside the barrier divided by the incident probability current. The 'conditional sojourn time' [98] gives the time of sojourn (dwell) in the spatial region of interest for some given conditions of scattering. It can be defined meaningfully by a 'clock' which is basically an extra degree of freedom that co-evolves with the sojourning particle. Büttiker and Landauer proposed [103] that one should study 'tunneling time' using the transmission coefficient through a static barrier of interest, supplemented by a small oscillatory perturbation. In another approach, the traversal time, is measured by the spin precession of the tunneling particle in a uniform infinitesimal magnetic field. This is called local 'Larmor time' [57, 104]. A large number of researchers interpret the 'phase time' [33, 105, 106] as the temporal delay of a transmitted wave packet. This time is usually taken as the difference between the time at which the peak of the transmitted packet

leaves the barrier and the time at which the peak of the incident quasi-monochromatic wave packet arrives at the barrier. Within the stationary phase approximation the phase time can be calculated from the energy derivative of the ‘phase shift’ in the transmitted or reflected amplitudes. Büttiker-Landauer [103] raised objection that the peak is not a reliable characteristic of packets distorted during the tunneling process. In contrast to ‘dwell time’ which can be defined locally, the ‘phase time’ is essentially asymptotic in character [107]. The ‘phase time’ statistics is intimately connected with dynamic admittance of micro-structures [108]. This ‘phase time’ is also directly related to the density of states [45]. The universality of ‘phase time’ distributions in random and chaotic systems has already been established earlier [109]. In the case of ‘not too opaque’ barriers, the tunneling time evaluated either as a simple ‘phase time’ [105] or calculated through the analysis of the wave packet behaviour [110] becomes independent of the barrier width. This phenomenon is termed as the Hartman effect [106, 110, 111]. This implies that for sufficiently large barriers the effective velocity of the particle can become arbitrarily large, even larger than the light speed in the vacuum (superluminal effect). Though this interpretation is a little far fetched for non-relativistic Schrödinger equation as velocity of light plays no role in it, this effect has been established even in relativistic quantum mechanics.

Though experiments with electrons for verifying this prediction are yet to be done, the formal identity between the Schrödinger equation and the Helmholtz equation for electromagnetic wave enables one to correlate the results for electromagnetic and microwaves to that for electrons. Photonic experiments show that electromagnetic pulses travel with group velocities in excess of the speed of light in vacuum as they tunnel through a constriction in a waveguide [100]. Experiments with photonic band-gap structures clearly demonstrate that ‘tunneling photons’ indeed travel with superluminal group velocities [99]. Their measured tunneling time is practically obtained by comparing the two peaks of the incident and transmitted wave packets. Thus all these experiments directly or indirectly confirmed the occurrence of Hartman effect without violating ‘Einstein causality’ *i.e.*, the signal velocity or the information transfer velocity is always bounded by the velocity of light. It should also be noted that in the photonic tunneling time experiments by Nimtz et al., based on frustrated total internal reflection, the velocity of the half-width of the pulse (not the peak of the wave packet) is monitored. The velocity of the half-width is found to be superluminal (according to theory and experiment). Relation of this result to the causality principle is discussed in the references [112, 113]. The ‘Hartman effect’ has been extensively studied both for nonrelativistic (Schrödinger equation) and relativistic (Dirac equation) [58, 100, 105] cases. Recently Winful [114] showed that the saturation of phase time is a direct consequence of saturation of integrated probability density under the barrier (equivalently in the electromagnetic waves saturation of stored energy). The Hartman effect has been found in one dimensional barrier tunneling [110] as well as for cases beyond one dimension as in tunneling through mesoscopic rings in presence of Aharonov-Bohm flux [25]. In the current note we extend the study of phase times for branched networks of quantum wires.

In section 5.2 we study the Hartman effect on a quantum ring geometry *i.e.* beyond one dimension and in the presence of Aharonov-Bohm (AB-) flux [21, 22]. Here due to non-zero AB-flux, electron, though traveling in sub-barrier regime, picks up one phase factor inside the ring. Our results show that even the ‘phase time’ for a given incident energy becomes

independent of the barrier thickness as well as the magnitude of the flux. These results confirm ‘Hartman effect’ in quantum ring even in presence of AB-flux. We have extended [21] this effect for a circular ring having two potential barriers with an intermediate free space where a quantum particle can propagate. Interestingly, the saturated phase time becomes independent of the intermediate free length (in the large length limit of the barriers) in the off resonant case. This result can be interpreted as a “space collapse or space destroyer” [115]. Even though in the intermediate free space (can be treated as potential well, due to two barriers at the two ends of it) inside the ring electronic wave can travel as a free propagating mode (and not as a evanescent mode), surprisingly the saturated delay time is independent of the length of the well (as if it does not count). In section 5.3 we shall present phase times [27] for branched networks of quantum wires which can readily be realized in optical wave propagation experiments. This geometry allows us to check other nonlocality effect such as tuning the saturation value of ‘phase time’ and consequently the superluminal speed in one branch by changing barrier strength or width in any other branch, spatially separated from the former.

5.2 Hartman effect in presence of AB-flux

We study the scattering problem across a quantum ring connected to one or two ideal semi infinite leads (as schematized in Fig. 5.1). Such ring geometry systems are extensively

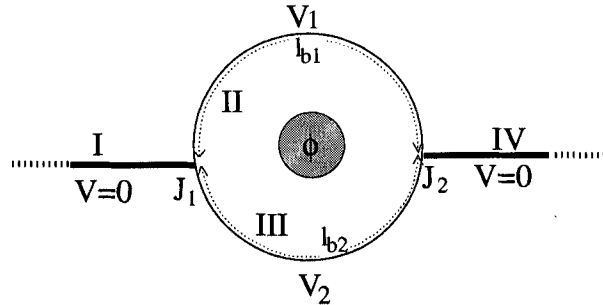


FIGURE 5.1: Schematic diagram of a ring connected to two leads in the presence of an Aharonov-Bohm flux, ϕ .

investigated in mesoscopic physics in analyzing normal state Aharonov-Bohm effect which has been observed experimentally [16, 17]. A magnetic field is applied perpendicular to the plane of the ring. Due to this a magnetic flux ϕ as shown in Fig. 5.1 is enclosed by the ring. There is a finite quantum mechanical potential of strength V inside the ring while that in the connecting leads are set to be zero. We focus on a situation wherein the incident electrons have an energy E less than V . The impinging electrons in this sub-barrier regime travels as an evanescent mode/wave throughout the circumference of the ring and the transmission or the conductance involve contributions from both the Aharonov-Bohm effect as well as quantum tunneling. Here we are interested in a single channel case where the Fermi energy lies in the lowest sub-band. To excite the evanescent modes in the ring we have to make the

width of the ring much less than that of the connecting wires. The electrons occupying the lowest sub-band in the connecting wire on entering the ring experience a higher barrier (due to higher quantum zero point energy) and propagate in the ring as evanescent mode. The transmission or conductance across such systems has been studied in detail [116, 117]. An analysis of the phase time for different ring systems is carried out in the following subsections.

5.2.1 Ring connected with two leads

We approach the scattering problem using the quantum wave guide theory [15, 116] for the system shown in Fig. 5.1. In the stationary case the incoming particles are represented by a plane wave e^{ikx} of unit amplitude. The effective mass of the propagating particle is m and the energy is $E = \hbar^2 k^2 / 2m$ where k is the wave vector corresponding to the free particle. The wave function in different regions (which are solutions of the Schrödinger equation) in the absence of magnetic flux are given below

$$\psi_0(x_0) = e^{ikx_0} + r e^{-ikx_0} \quad (\text{in region I}) \quad (5.1)$$

$$\psi_1(x_1) = A_1 e^{iq_1 x_1} + B_1 e^{-iq_1 x_1} \quad (\text{in region II}) \quad (5.2)$$

$$\psi_2(x_2) = A_2 e^{iq_2 x_2} + B_2 e^{-iq_2 x_2} \quad (\text{in region III}) \quad (5.3)$$

$$\psi_3(x_3) = t e^{ikx_3} \quad (\text{in region IV}) \quad (5.4)$$

with k being the wave-vector of electrons in the leads. $q_1 = \sqrt{2m(E - V_1)/\hbar^2}$ is the wave-vector for propagating electrons in the barrier of strength V_1 on the upper arm while $q_2 = \sqrt{2m(E - V_2)/\hbar^2}$ is that in the V_2 on the lower arm of the ring. The origin of the co-ordinates of x_0 and x_1 is assumed to be at J_1 and that for x_2 and x_3 are at J_2 . At J_1 , $x_2 = lb_2$, at J_2 , $x_1 = lb_1$, where lb_1 and lb_2 are the length of the two barriers on the upper and lower arms of the ring respectively. Total circumference of the ring is $L = lb_1 + lb_2$.

We use Griffith's boundary conditions [52]

$$\psi_0(0) = \psi_1(0) = \psi_2(lb_2) \quad (5.5)$$

and

$$\left. \frac{\partial \psi_0(x_0)}{\partial x_0} \right|_{J_1} + \left. \frac{\partial \psi_1(x_1)}{\partial x_1} \right|_{J_1} + \left. \frac{\partial \psi_2(x_2)}{\partial x_2} \right|_{J_1} = 0, \quad (5.6)$$

at the junction J_1 . All the derivatives are taken either outward or inward from the junction [15]. Similar boundary conditions hold for J_2 as well.

$$\psi_1(lb_1) = \psi_2(0) = \psi_3(0) \quad (5.7)$$

$$\text{and} \quad \left. \frac{\partial \psi_1(x_1)}{\partial x_1} \right|_{J_2} + \left. \frac{\partial \psi_2(x_2)}{\partial x_2} \right|_{J_2} + \left. \frac{\partial \psi_3(x_3)}{\partial x_3} \right|_{J_2} = 0, \quad (5.8)$$

We choose a gauge for the vector potential in which the magnetic field appears only in the boundary conditions rather than explicitly in the Hamiltonian [15, 16]. Thus the electrons propagating clockwise and anticlockwise will pick up opposite phases. The electrons propagating in the clockwise direction from J_1 will pick up phases $i\alpha_1$ at J_2 and electrons propagating anticlockwise from J_2 to J_1 in the upper arm pick up a phase $-i\alpha_1$ at J_1 .

Similarly, an electron picks up a phase $i\alpha_2$ at J_1 moving in the clockwise direction from J_2 in the lower arm and $-i\alpha_2$ at J_2 when moving anticlockwise from J_1 in the lower arm of the ring. The total phase around the ring is $\alpha_1 + \alpha_2 = 2\pi\phi/\phi_0$, where ϕ and ϕ_0 are the magnetic flux and flux quantum, respectively. Hence from above mentioned boundary conditions we get for tunneling particle

$$\text{at } J_1 : \quad 1 + r - A_1 - B_1 \exp(-i\alpha_1) = 0, \quad (5.9)$$

$$A_2 \exp(-\kappa_2 lb_2) \exp(i\alpha_2) + B_2 \exp(\kappa_2 lb_2) - 1 - r = 0, \quad (5.10)$$

$$ik(1-r) + \kappa_1 A_1 - \kappa_1 B_1 \exp(-i\alpha_1) - \kappa_2 A_2 \exp(-\kappa_2 lb_2) \exp(i\alpha_2) + \kappa_2 B_2 \exp(\kappa_2 lb_2) = 0, \quad (5.11)$$

$$\text{at } J_2 : \quad A_1 \exp(-\kappa_1 lb_1) \exp(i\alpha_1) + B_1 \exp(\kappa_1 lb_1) - t = 0, \quad (5.12)$$

$$A_2 + B_2 \exp(-i\alpha_2) - t = 0, \quad (5.13)$$

$$ikt + \kappa_1 A_1 \exp(-\kappa_1 lb_1) \exp(i\alpha_1) - \kappa_1 B_1 \exp(\kappa_1 lb_1) - \kappa_2 A_2 + \kappa_2 B_2 \exp(-i\alpha_2) = 0, \quad (5.14)$$

with $\kappa_1 = \sqrt{2m(V_1 - E)/\hbar^2}$ and $\kappa_2 = \sqrt{2m(V_2 - E)/\hbar^2}$ being the imaginary wave vectors, in presence of rectangular barriers of strength V_1 and V_2 respectively, inside the ring.

Solving Eqs. (5.9) - (5.14) for an electron traversing the ring with two barriers of equal strength $V_1 = V_2 = V$ along its entire circumference, as shown in Fig. 5.1, we obtain an analytical expression for the complex transmission amplitude t as

$$t = \frac{4ik\kappa \exp(i\alpha_1) [P \exp(\kappa lb_1) + Q e^{\kappa lb_2}]}{PQk^2 + 2ik\kappa S_- + 4\kappa^2 [\exp(\kappa L) (1 + \exp(4i\pi\frac{\phi}{\phi_0})) - S_+]} \quad (5.15)$$

where

$$\begin{aligned} P &= \exp(2i\pi\frac{\phi}{\phi_0}) (\exp(2\kappa lb_2) - 1), \\ Q &= (\exp(2\kappa lb_1) - 1), \\ S_{\pm} &= \exp(2i\pi\frac{\phi}{\phi_0}) (\exp(2\kappa L) \pm 1), \end{aligned}$$

with κ being the imaginary wave vector for the evanescent wave inside the barriers. Once t is known, the transmission phase time can be calculated from the energy derivative of the phase of the transmission amplitude

$$\tau_t = \hbar \frac{\partial \arg[t]}{\partial E} = \frac{1}{v} \frac{\partial \arg[t]}{\partial k}, \quad (5.16)$$

where, $v = \hbar k/m$ is the velocity of the free particle. In what follows, let us set $\hbar = 1$ and $2m = 1$. We express all the physical quantities in dimensionless units i.e. the barrier strength in unit of incident energy E ($V \equiv V/E$), barrier widths in units of inverse wave vector k^{-1} ($lb_n \equiv k lb_n$), where $k = \sqrt{E}$ and 'transmission phase time' τ_t in units of inverse of incident energy E ($\tau_t \equiv E \tau_t$). We now proceed to analyze the behaviour of 'transmission phase time' as a function of various physical parameters for different ring systems.

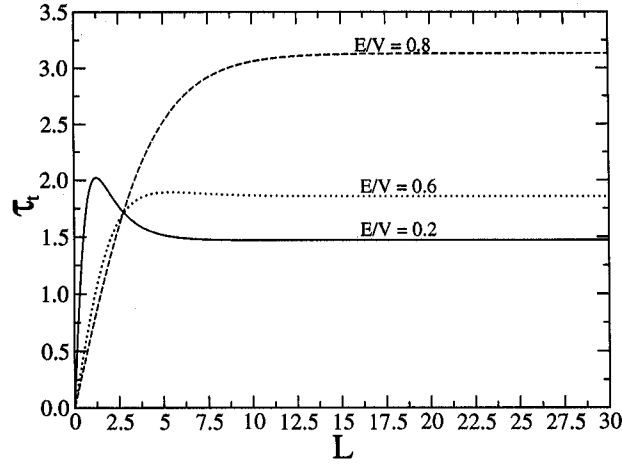


FIGURE 5.2: Plot of τ_t versus L for three different values of E/V with $\phi = 0$ and $lb_1 = lb_2$.

In Fig. 5.2 we plot phase time τ_t as a function of length L of the ring for different values of incident energies in the absence of magnetic flux ϕ for the case where the two arm lengths lb_1 and lb_2 are equal. From the figure we clearly see that τ_t evolves as a function of length L and asymptotically saturates to a value ($\tau_{t,s}$) which is independent of L thus confirming the Hartman effect. The saturation value, $\tau_{t,s}$, increases with increasing incident energy and the corresponding $\tau_{t,s}$ values for $E = 0.2V$, $0.6V$ and $0.8V$ are 1.47, 1.86 and 3.13 respectively. From Fig. 5.2, note that, depending upon the incident electron energy, τ_t is a monotonic or non-monotonic function of L in the small length limit.

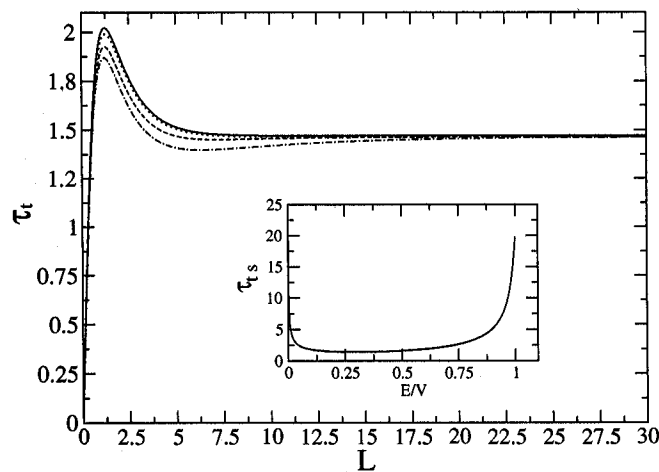


FIGURE 5.3: Plot of τ_t versus L for different arm length ratios. The ratio $lb_1 : lb_2$ for the solid, dotted, dashed and dot-dashed curves are 1 : 1, 3 : 2, 4 : 1, 9 : 1 respectively. Inset shows $\tau_{t,s}$ versus E/V for $L = 30$ with equal arm length ratios.

In Fig. 5.3 we plot the transmission phase time versus L for a particular energy, $E = 0.2V$, in the absence of magnetic flux ϕ but for different length ratios of the upper and lower arms. We observe that the saturation value of the phase time is independent of the arm length ratios for a given energy as one can anticipate. In the inset of Fig. 5.3 we plot τ_{ts} versus E/V for $\phi = 0$, $L = 30$ with equal upper and lower arm lengths. Plots with different arm length ratios ($lb_1 : lb_2$) with different ϕ in the asymptotic limit were found to overlap with the above curve in the entire energy regime. Analytically, in the large L ($> 1/\kappa$) limit, the transmission phase time τ_t becomes independent of L and the magnetic flux (in accordance with Hartman effect) and is given by

$$\tau_{ts} = \frac{4\kappa^3 + 5k^2\kappa + (k^4/\kappa)}{2k((2\kappa^2 - (k^2/2))^2 + 4k^2\kappa^2)}. \quad (5.17)$$

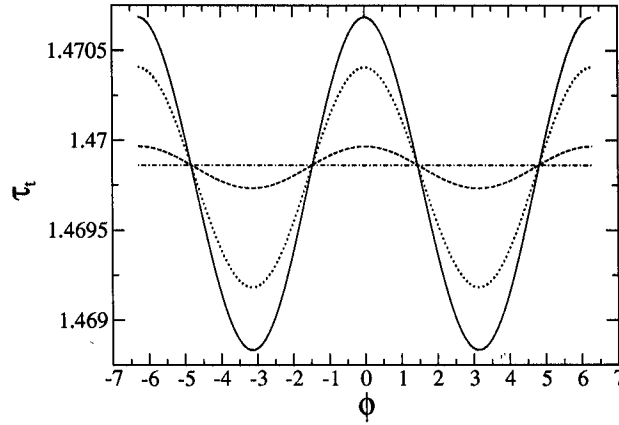


FIGURE 5.4: Plot of τ_t versus ϕ for different L . The solid, dotted, dashed and dot-dashed curves are for $L = 10, 10.5, 12.5, 30$ respectively with equal upper and lower arm-lengths.

In Fig. 5.4 we have plotted transmission phase time as a function of flux ϕ for various values of circumference of the ring with $lb_1 = lb_2$ and $E = 0.2V$. We observe that τ_t is flux periodic with periodicity ϕ_0 . This is consistent with the fact that all the physical properties in presence of Aharonov-Bohm flux across the ring must be periodic function of flux with a period ϕ_0 [5, 17, 45]. However, we observe that as we increase the length of the ring the visibility or the magnitude of Aharonov-Bohm oscillations in τ_t decreases. Consequently in the large length limit the visibility of these oscillations vanishes as can be seen from Fig. 5.4. The constant value of τ_t thus obtained in the presence of flux is identical to τ_{ts} (1.4698) in the absence of flux (see Fig. 5.2) in the large length regime. This numerically obtained value of τ_{ts} is in perfect agreement with the analytical expression for τ_{ts} , Eq. (5.17), given above. This result clearly indicates that the delay time in the presence of opaque barrier becomes not only independent of length of the circumference but also is independent of the AB-flux thereby observing the Hartman effect in the presence of AB-flux. We also find that the behaviour of reflection delay time is same as transmission delay time as anticipated from general symmetry laws from the simple geometric structure considered in the present case.

5.2.2 Ring connected with one lead

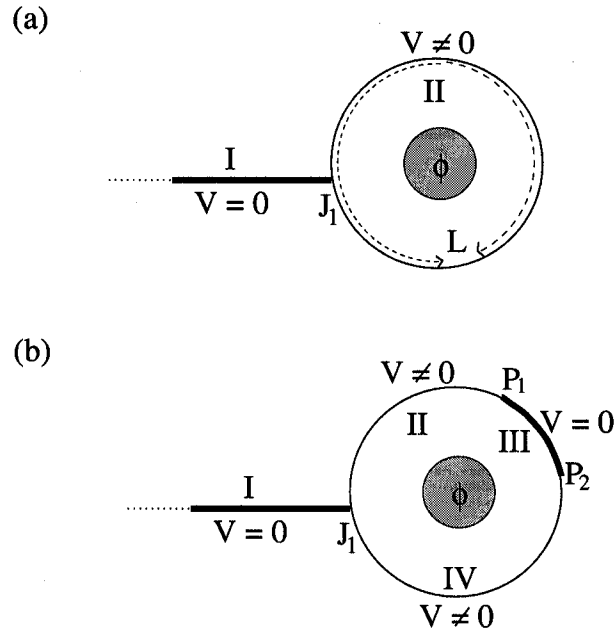


FIGURE 5.5: Schematic diagram of a circular ring connected to semi infinite lead.

Now we discuss the ‘reflection phase time’ for the above quantum ring but connected to a single wire of semi-infinite length and in presence of AB-flux as shown in Fig 5.5(a). Here also we focus on the tunneling of an electron in the sub-barrier regime. We analyze the phase time of the reflected wave. It is well known that in one dimensional scattering/tunneling problem, reflection involves prompt part as well as the multiple scattering arising from the edges of the scattering center (say, for the square barrier). However, transmission across the scattering region does not have the prompt part but has only contributions from multiple scattering. We would like to emphasize here the fact that the unitarity of the scattering matrix forces transmission and reflection phase times to coincide for a one dimensional tunneling problem (to be identical in magnitude) [as we see in section 2.5], even though reflection has a prompt part as mentioned above. For symmetric barrier the phase of the reflection and the transmission amplitudes differ by a constant phase $\pi/2$ [see in section 2.5]. Hence, the information we get does not depend on whether we study the phase time in the reflection or in the transmission mode. Thus in the present section we have chosen a simple and generalized geometry where we can analytically study the phase time in a reflection mode and in presence of Aharonov-Bohm flux. We show that this phase time in the opaque barrier regime becomes independent of the length of the circumference of the ring and the magnitude of the AB-flux. We have also studied this effect by including an additional potential well between two barriers in the circular ring (Fig. 5.5 (b)). Interestingly, the saturated reflection phase time becomes independent of the length of the potential well (in the large length limit) for energy away from resonances. Inside the potential well the electron

travels as a free wave. Increasing or decreasing the free path (length of the well) does not alter the saturated reflection phase time through the system. It seems as if electronic wave does not count the free space in between two barriers. This result is regarded as a “space collapse” or “space destroyer” [115].

We use the same quantum wave guide theory [15, 116] discussed above to get the reflection phase time for the system shown in Fig. 5.5(b). The wave functions in different regions are

$$\psi_0(x_0) = e^{ikx_0} + r e^{-ikx_0} \quad (\text{in region I}) \quad (5.18)$$

$$\psi_1(x_1) = A_1 e^{-\kappa_1 x_1} + B_1 e^{\kappa_1 x_1} \quad (\text{in region II}) \quad (5.19)$$

$$\psi_w(x_w) = C e^{ikx_w} + D e^{-ikx_w} \quad (\text{in region III}) \quad (5.20)$$

$$\psi_2(x_2) = A_2 e^{\kappa_2 x_2} + B_2 e^{-\kappa_2 x_2} \quad (\text{in region IV}) \quad (5.21)$$

with k being the wave-vector of electrons in the lead and in the intermediate free space between two barriers inside the ring. $\kappa_1 = \sqrt{2m(V_1 - E)/\hbar^2}$ and $\kappa_2 = \sqrt{2m(V_2 - E)/\hbar^2}$ are the imaginary wave-vectors respectively for tunneling electrons in the barriers of strength V_1 and V_2 inside the ring. The origin of the co-ordinates of x_0 and x_1 is assumed to be at J_1 and that for x_w and x_2 are at P_1 and P_2 respectively. At P_1 , $x_1 = lb_1$, at P_2 , $x_w = w$ and at J_1 , $x_2 = lb_2$, where lb_1 and lb_2 are the length of the two barriers separated by a well region of length w inside the ring. Total circumference of the ring is $L = lb_1 + lb_2 + w$.

In presence of the AB-flux, following the same method described above, the boundary conditions for the current system (shown in Fig. 5.5(b)) become

$$1 + r - A_1 - B_1 \exp(-i\alpha_1) = 0, \quad (5.22)$$

$$A_2 \exp(-\kappa_2 lb_2) \exp(i\alpha_2) + B_2 \exp(\kappa_2 lb_2) - 1 - r = 0, \quad (5.23)$$

$$ik(1 - r) + \kappa_1(A_1 - B_1 \exp(-i\alpha_1)) - \kappa_2 A_2 \exp(-\kappa_2 lb_2) \exp(i\alpha_2) - \kappa_2 B_2 \exp(\kappa_2 lb_2) = 0, \quad (5.24)$$

$$A_1 \exp(-\kappa_1 lb_1) \exp[i\alpha_1] + B_1 \exp(\kappa_1 lb_1) - C - D \exp(-i\alpha_w) = 0, \quad (5.25)$$

$$\kappa_1 A_1 \exp(-\kappa_1 lb_1) \exp(i\alpha_1) - \kappa_1 B_1 \exp(\kappa_1 lb_1) + ikC - ikD \exp(-i\alpha_w) = 0, \quad (5.26)$$

$$C \exp(ikw) \exp(i\alpha_w) + D \exp(-ikw) - A_2 - B_2 \exp(-i\alpha_2) = 0, \quad (5.27)$$

$$ikC \exp(ikw) - ikD \exp(-ikw) \exp(-i\alpha_w) + \kappa_2 A_2 - \kappa_2 B_2 \exp(-i\alpha_2) = 0, \quad (5.28)$$

where $i\alpha_1$, $i(\alpha_1 + \alpha_w)$ are the phases picked up respectively at P_1 and P_2 by the electron traveling clockwise from J_1 and $i(\alpha_1 + \alpha_w + \alpha_2)$ is the phase picked up by the same electron at J_1 after traversing once along the ring. The total phase around the ring becomes $\alpha_1 + \alpha_w + \alpha_2 = 2\pi\phi/\phi_0$.

Solving Eqs. (5.22)- (5.28) for a ring system with a rectangular barrier of strength V along its entire circumference (Fig. 5.5(a)) we obtain an analytical expression for the reflection

amplitude as

$$r = \frac{-\kappa_1 (2 \cos(\alpha) - \exp(kL)) + i \frac{k}{2} \exp(kL)}{\kappa_1 (2 \cos(\alpha) - \exp(kL)) + i \frac{k}{2} \exp(kL)}, \quad (5.29)$$

where $\alpha = \alpha_1 + \alpha_w + \alpha_2$. After knowing r , the 'reflection phase time' τ_r can be calculated from the energy derivative of its phase [33, 105] as

$$\tau_r = \frac{\partial \text{Arg}[r]}{\partial E}. \quad (5.30)$$

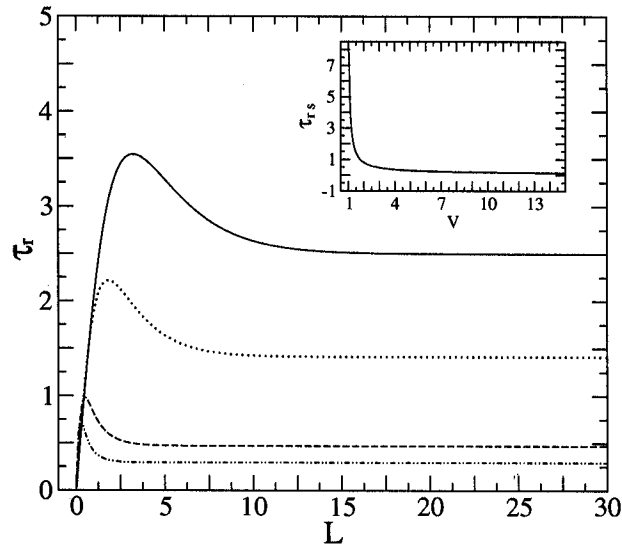


FIGURE 5.6: In absence of magnetic flux (*i.e.* $\phi = 0$), for a ring with a barrier of strength V throughout its circumference, the reflection phase time τ_r is plotted as a function of ring's circumference L . The solid, dotted, dashed and dash-dotted curves are for $V = 1.25, 1.5, 3, 5$ respectively. Incident energy is set to be $E = 1$. In the inset the saturated value of phase time τ_{rs} is plotted as a function of the barrier's strength for same E .

We now proceed to analyze the behavior of τ_r as a function of various physical parameters for different ring systems. In the similar fashion, described above, here also we express all the physical quantities in dimensionless units. Thus the reflection phase time τ_r is expressed in units of inverse of incident energy E ($\tau_r \equiv E \tau_r$). After straight forward algebra in the large length (L) limit and in absence of magnetic flux, we obtain an analytical expression for the saturated reflection phase time (using Eq. (5.29) in Eq. (5.30)), which is given by,

$$\tau_{rs} = \frac{\frac{1}{k\kappa} + \frac{k}{\kappa^3}}{\left(2 + \frac{k^2}{2\kappa^2}\right)}, \quad (5.31)$$

with κ being the imaginary wave vector of the electron inside the barrier of strength V and width lb ($= L$).

First we take up a ring system with a single barrier along the circumference of the ring. For a tunneling particle having energy less than the barrier's strength we find out the reflection phase time τ_r as a function of barrier's width L which in turn is the circumference of the ring. We see (Fig. 5.6) that in absence of magnetic flux, τ_r evolves as a function of L and asymptotically saturates to a value $\tau_{r,s}$ which is independent of L thus confirming the 'Hartman effect'. From Fig. 5.6 it is clear that the saturation value increases with the decreasing barrier-strength. In the inset of Fig. 5.6, we have plotted $\tau_{r,s}$ as a function of barrier-strength. From this we can see that for electrons with incident energy close to the barrier-strength the value of $\tau_{r,s}$ is quite large.

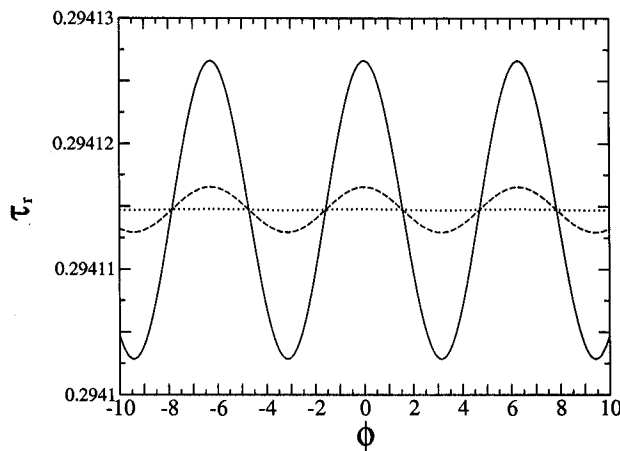


FIGURE 5.7: For a ring with a barrier of strength V lies throughout its circumference, the saturated phase time $\tau_{r,s}$ is plotted as a function of magnetic flux ϕ . The solid, dashed and dotted curves are for $L = 6, 7, 9$ respectively. Other system parameters are $V = 5$, $E = 1$.

To see the effect of magnetic flux on 'Hartman effect', we consider the same system but in presence of Aharonov-Bohm (AB) flux. We find out, for the tunneling particle, the reflection phase time as a function of embedded magnetic flux for different lengths L of the barrier covering the ring's circumference. We have chosen the lengths such that in absence of the 'AB-flux', for a given system (*i.e.* for known E and V) the reflection phase time τ_r gets saturated in these lengths. From Fig. 5.7 we see that τ_r as a function of ϕ shows AB-oscillations with an average value which is the saturation value $\tau_{r,s}$ for the same system in absence of AB-flux. Further observe that (Fig. 5.7) τ_r is flux periodic with periodicity ϕ_0 . This is consistent with the fact that all the physical properties in presence of AB-flux across the ring must be periodic function of the flux with a period ϕ_0 [5, 17, 108]. However, we see that as we increase L the magnitude of AB-oscillation in τ_r decreases. Consequently in the large length limit the visibility vanishes. This clearly establishes 'Hartman effect' even in presence of AB-flux. The constant value of τ_r thus obtained in the presence of flux is identical to $\tau_{r,s}$ (0.294115) in the absence of flux (see Fig. 5.7) in the large length regime and its magnitude is given by Eq. (5.31). This result clearly indicates that the reflection phase time in the presence of opaque barrier becomes not only independent of length of the circumference but also is independent of the AB-flux thereby observing the 'Hartman effect'

in the presence of AB-flux.

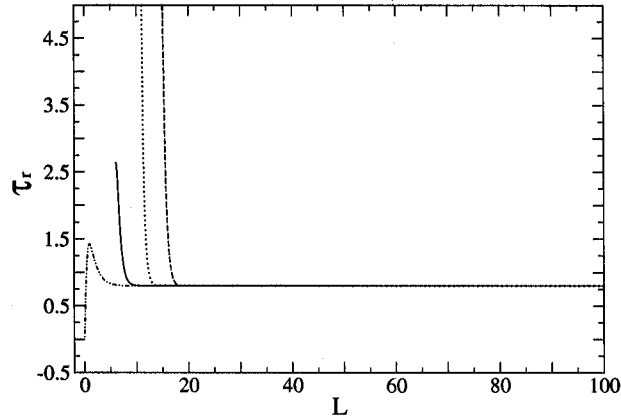


FIGURE 5.8: In absence of magnetic flux (*i.e.* $\phi = 0$), for a ring with two barriers of strength V_1 and V_2 separated by an intermediate well region, the reflection phase time τ_r is plotted as a function of ring's circumference L for different width w of the well. The dashed-dotted, solid, dotted and dashed curves are for $w = 0, 1, 5, 10$. Other system parameters are $lb_2 = 5$, $V_1 = V_2 = 2$ and $E = 1$.

Now we consider the ring system with the ring having two successive barriers separated by an intermediate free space as shown in Fig. 5.5(b). In absence of magnetic flux, we see the effect of 'quantum well' on the reflection phase time τ_r . In Fig. 5.8 τ_r is plotted as a function of one of the barrier's length (say lb_1) while other barrier's length is fixed ($lb_2 = 5$) and for few different values of length of the well. Here, the fixed value of the barrier's length lb_2 is chosen in such a way that in absence of the well region the reflection phase time reaches saturation at this length. From Fig. 5.8 we see that for all parameter values of well's width, the saturation value of reflection phase time $\tau_{r,s}$ is same and it is equal to what we obtained in absence of the well in the ring system. Thus the saturated phase time becomes independent of the width of the well (in the long length limit) for the energy away from the resonances. This is as if the effective velocity of the electron in the well becomes infinite or equivalently length of the well does not count (space collapse or space destroyer) while traversing the ring.

Finally consider a similar system as that shown in Fig. 5.5(b). Here we see the effect of resonances, present in the ring system with a well, on the saturated reflection phase time $\tau_{r,s}$. For the system described above with $V_1 = V_2 = 2$, $lb_2 = 5$, $\phi = 0$ we have plotted $\tau_{r,s}$, for the electrons with incident energy $E = 1$, as a function of the well's width for different parameter values lb_1 in Fig. 5.9. We see that the resonances which have Lorentzian shape become sharper and narrower as the width of the barrier lb_1 becomes large. For very large lb_1 the resonances are very hard to detect. It should be noted that as we increase the length of the well for fixed E for particular barrier lengths incident energy E coincides with resonances (or resonant states) in the well (which arise due to constructive interference due to multiple scatterings inside the well). For these values of lengths we observe sharp rise in the saturated delay time and its magnitude depends on the length of the well. It is worth to mention that

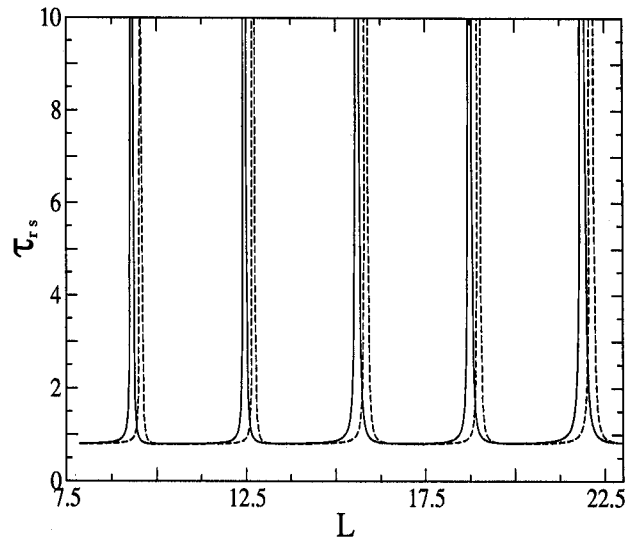


FIGURE 5.9: In absence of magnetic flux (*i.e.* $\phi = 0$), for a ring with two barriers of strength V_1 and V_2 separated by an intermediate well region, the saturated phase time τ_{rs} is plotted as a function of ring's circumference L for different width lb_1 of the barrier. The solid and dashed curves are for $lb_1 = 2.75, 3$ respectively. Other systems parameters are $lb_2 = 5$, $V_1 = V_2 = 2$ and $E = 1$.

away from the resonance the value of τ_{rs} is independent of the length of the well (see Fig.5.8) and depends only on the barrier strength.

5.3 Hartman effect and non-locality in quantum networks

Hartman effect is itself one of the manifestations of quantum non-locality [99]. Here we study the effect for various quantum mechanical networks having potential barriers in its arms. In such systems it is possible to control the 'super arrival' time in one of the arms by changing parameters on another, spatially separated from it. This is yet another quantum nonlocal effect. Negative time delays (time advancement) and 'ultra Hartman effect' with negative saturation times have been observed in some parameter regimes.

As a model system, we choose a network of thin wires. The width of these wires are so narrow that only the motion along the length of the wires is of interest (a single channel case). The motion in the perpendicular direction is frozen in the lowest transverse sub-band. In a three-port Y-branch circuit (Fig. 5.10) two side branches of quantum wire S_1 and S_2 are connected to a 'base' arm S_0 at the junction J . In general one can have $N(\geq 2)$ such side branches connected to the 'base' wire.

We study the scattering problem across a network geometry as presented schematically in Fig. 5.10. Such geometries are important from the point of view of basic science due to their properties of tunneling and interference [16, 17] as well as in applications such as wiring in nano-structures. In particular, the Y-junction carbon nanotubes are in extensive studies and

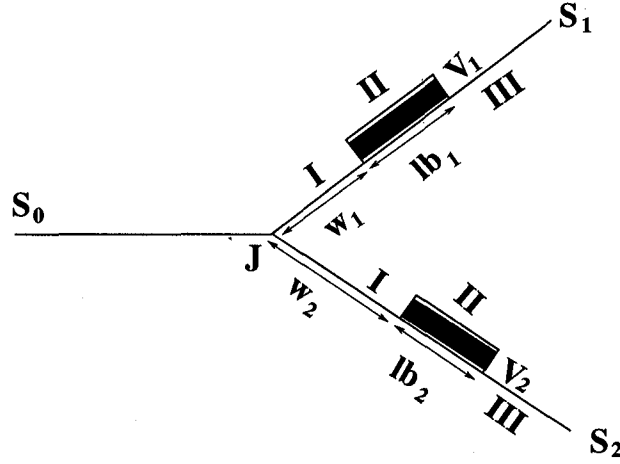


FIGURE 5.10: Schematic diagram of a Y-junction or three-way splitter.

they show various interesting properties like asymmetric current voltage characteristics [118]. In our system of interest there are finite quantum mechanical potential barriers of strength V_n and width lb_n in the n -th side branch. The number of side branches can vary from $n = 2, 3, \dots, N$. We focus on a situation wherein the incident electrons have an energy E less than V_n for all n . The impinging electrons in this sub-barrier regime travels as an evanescent mode/wave and the transmission involve contributions from quantum tunneling and multiple reflections between each pair of barriers and the junction point. Here we are interested in a single channel case where the Fermi energy lie in the lowest sub-band. To excite the evanescent modes in the side branches one has to produce constrictions by making the width of the regions of wires containing barriers much thinner than that of other parts of the wires. The electrons occupying the lowest sub-band in the connecting wire on entering the constrictions experience a potential barrier (due to higher quantum zero point energy) and propagate as an evanescent mode [116, 117]. In this work an analysis of the phase time or the group delay time in such a system is carried out.

5.3.1 Theoretical treatment

We approach this scattering problem using the quantum wave guide theory [15, 66] as we did in the previous case. The wave functions, in different regions of the system considered (Fig. 5.10) can be written as,

$$\begin{aligned}\psi_{in}(x_0) &= e^{ikx_0} + Re^{-ikx_0} \quad (\text{in } S_0), \\ \psi_{(n)I}(x_n) &= A_n e^{ikx_n} + B_n e^{-ikx_n} \quad (\text{region I in } S_n), \\ \psi_{(n)II}(x_n) &= C_n e^{-\kappa_n(x_n-w_n)} + D_n e^{\kappa_n(x_n-w_n)} \quad (\text{region II in } S_n), \\ \psi_{(n)III}(x_n) &= t_n e^{ik(x_n-w_n-lb_n)} \quad (\text{region III in } S_n),\end{aligned}$$

with $\kappa_n = \sqrt{2m(V_n - E)/\hbar^2}$ being the imaginary wave vector in presence of rectangular barrier of strength V_n . $\psi_{(n)I}$, $\psi_{(n)II}$ and $\psi_{(n)III}$ denote wave functions in three regions I, II

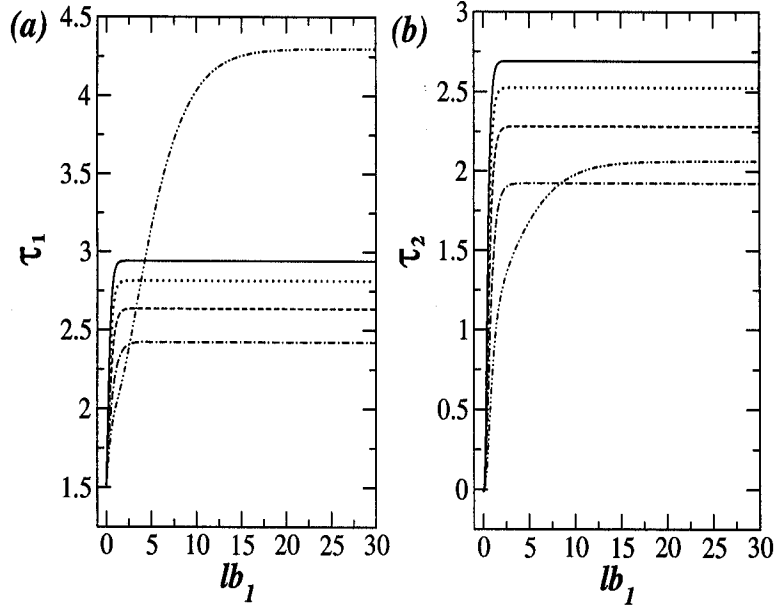


FIGURE 5.11: For a 3-way splitter with a barrier in S_1 arm, the ‘phase times’ τ_1 and τ_2 are plotted as a function of barrier width ‘ lb_1 ’ in (a) and (b) respectively. The solid, dotted, dashed, dot-dashed and the dashed-double dotted curves are for $V_1 = 5, 4, 3, 2,$ and 1.05 respectively. Other system parameters are $E = 1, w_1 = 3$.

and III , respectively, on n -th side branch. x_0 is the spatial coordinate for the ‘base’ wire, whereas x_n is spatial coordinate for the n -th arm. All these coordinates are measured from the junction J . In n -th side branch, the barrier starts at a distance w_n from the junction J .

To solve the problem, we use Griffith’s boundary conditions [52]

$$\psi_{in}(J) = \psi_{(n=1)_I}(J) = \psi_{(n=2)_I}(J) = \dots = \psi_{(n=N)_I}(J), \quad (5.32)$$

and

$$\left. \frac{\partial \psi_{in}(x_0)}{\partial x_0} \right|_J = \sum_n \left. \frac{\partial \psi_{(n)_I}}{\partial x_n} \right|_J, \quad (5.33)$$

at the junction J . All the derivatives are taken either outward or inward from the junction [15]. In each side branch, at the starting and end points of the barrier, the boundary conditions can be written as

$$\psi_{(n)_I}(w_n) = \psi_{(n)_{II}}(w_n), \quad (5.34)$$

$$\psi_{(n)_{II}}(w_n + lb_n) = \psi_{(n)_{III}}(w_n + lb_n), \quad (5.35)$$

$$\left. \frac{\partial \psi_{(n)_I}}{\partial x_n} \right|_{(w_n)} = \left. \frac{\partial \psi_{(n)_{II}}}{\partial x_n} \right|_{(w_n)}, \quad (5.36)$$

$$\left. \frac{\partial \psi_{(n)_{II}}}{\partial x_n} \right|_{(w_n + lb_n)} = \left. \frac{\partial \psi_{(n)_{III}}}{\partial x_n} \right|_{(w_n + lb_n)}. \quad (5.37)$$

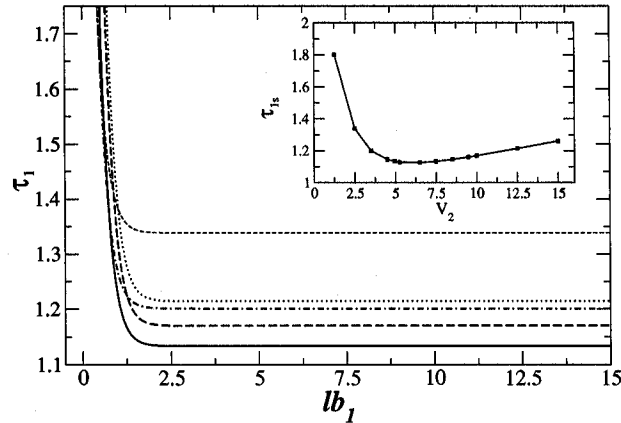


FIGURE 5.12: Here for a 3-way splitter with one barrier in each branched arm S_1 and S_2 , the ‘phase times’ τ_1 is plotted as a function of barrier width ‘ lb_1 ’ keeping $lb_2(= 1)$ and $V_1(= 5)$ fixed and for different values of parameter V_2 . The small dashed, dot-dashed, solid, long dashed and dotted curves are for $V_2 = 2.5, 3.5, 5.0, 10.0$ and 12.5 respectively. Other system parameters are $E = 1, w_1 = w_2 = 3$. In the inset τ_{s1} is plotted as a function of V_2 for the same system parameters.

From the above mentioned boundary conditions one can obtain the complex transmission amplitudes t_n on each of the side branches.

5.3.2 Results and Discussions

In the similar fashion, as we did in the earlier section, following the method introduced by Wigner [33], we can calculate the ‘phase time’ (phase time for transmission) from the energy derivative of the phase of the transmission amplitude t_n [33, 105] as

$$\tau_n = \hbar \frac{\partial \text{Arg}[t_n]}{\partial E}, \quad (5.38)$$

where, $v = \hbar k/m$ is the velocity of the free particle.

In what follows, let us set $\hbar = 1$ and $2m = 1$. We now proceed to analyze the behavior of τ_n as a function of various physical parameters for different network topologies. We measure time at the far end of each barrier in the branched arms containing barriers and in the case of arms in absence of any barrier we measure the phase time at the junction points. We express all the physical quantities in dimensionless units *i.e.* all the barrier strengths V_n in units of incident energy E ($V_n \equiv V_n/E$), all the barrier widths lb_n in units of inverse wave vector k^{-1} ($lb_n \equiv k lb_n$), where $k = \sqrt{E}$ and all the extrapolated phase time τ_n in units of inverse of incident energy E ($\tau_n \equiv E \tau_n$).

First we take up a system similar to the Y-junction shown in Fig. 5.10 in presence of a barrier V_1 of width lb_1 in arm S_1 but in absence of any barrier in arm S_2 . For a tunneling particle having energy $E < V_1$ we find out the phase time τ_1 in arm S_1 as well as τ_2 in arm S_2 as a function of barrier width lb_1 (Fig. 5.11). From Fig. 5.11(a) it is clear that τ_1 evolves with lb_1 and eventually saturates to τ_{s1} for large lb_1 to show the Hartman effect. Fig. 5.11(b)

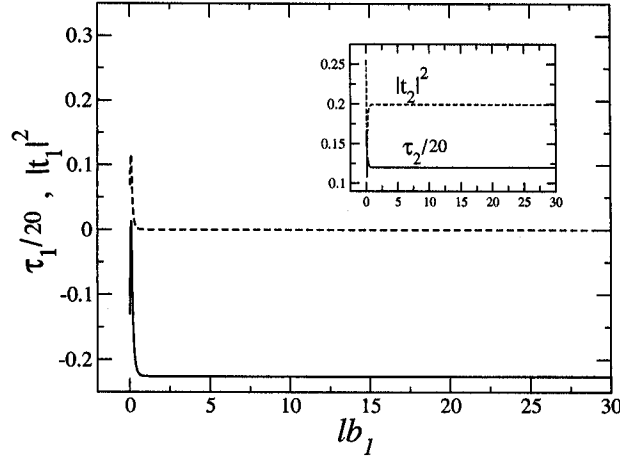


FIGURE 5.13: Here for a 3-way splitter with one barrier in each side branch S_1 and S_2 , the ‘phase times’ τ_1 (solid curve) and $|t_1|^2$ (dashed) are plotted as a function of ‘ lb_1 ’ for a very small $lb_2 (= 0.5)$. Other system parameters are $E = 1$, $w_1 = w_2 = 2.5$, $V_2 = 5$ and $V_1 = 15$. In the inset, the solid and dashed curves represent τ_2 and $|t_2|^2$ respectively as a function of lb_1 . For better visibility we have plotted phase times scaled down by a factor of 20.

shows the phase time τ_2 in arm S_2 which does not contain any barrier. This also evolves and saturates with lb_1 , the length of the barrier in the other arm S_1 . This delay is due to the contribution from paths which undergo multiple reflection in the first branch before entering the second branch via junction point J . In absence of a barrier in the n -th arm the phase time τ_n measured close to the junction J should go to zero *i.e.* $\tau_n \rightarrow 0$ in the absence of multiple scatterings in the first arm. Note that τ_{s1} and τ_{s2} change with energies of the incident particle (Fig. 5.11). From Fig.5.11 it can be easily seen that τ_{s2} is always smaller than τ_{s1} for any particular V_1 *i.e.* the saturation time in the arm having no barrier is smaller. The phase time in both the arms show non-monotonic behavior as a function of V_1 . As we decrease the strength of the barrier V_1 the value of τ_1 (τ_2) decreases in the whole range of widths of the barrier and also the saturated value of τ_{s1} (τ_{s2}) decreases until V_1 reaches 1.6 and with further decrease in V_1 the values of τ_1 (τ_2) as well as τ_{s1} (τ_{s2}) starts increasing.

As the second case we take up another Y-junction which contain potential barriers in both its side branches as shown in Fig. 5.10. We fix the values of $V_1 (= 5)$ and vary lb_1 for each values of V_2 to study the lb_1 -dependence of τ_1 (Fig.5.12). From Fig. 5.12 we see that τ_1 decreases with increase in lb_1 to saturate to a value τ_{s1} at each value of V_2 thereby showing ‘Hartman effect’ for arm ‘ S_1 ’. But now, we can tune the saturation phase time at arm S_1 non-locally by tuning strength of the barrier potential V_2 sitting on another arm S_2 ! Thus ‘quantum nonlocality’ enables us to control the ‘super arrival’ time in one of the arms (S_1) by changing a parameter (V_2) on another, spatially separated from it. In the inset of Fig. 5.12 we plot τ_{s1} as a function of V_2 . It clearly shows that when the barrier strengths V_1 and V_2 are very close the ‘phase time’ reaches its minimum value. In all other cases *i.e.* whenever $V_1 \neq V_2$, the value of τ_{s1} is larger.

We shall show now another interesting result related to the Hartman effect. For this we

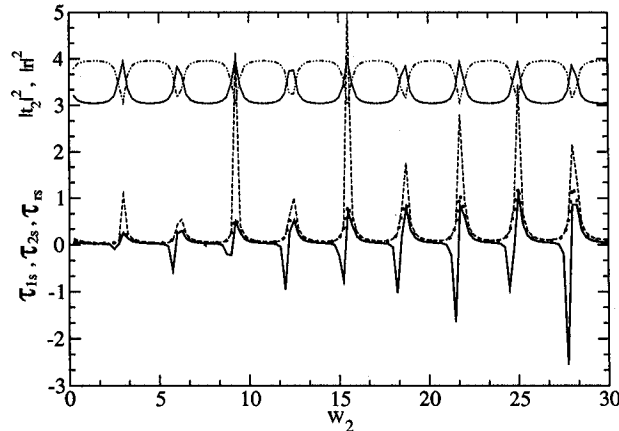


FIGURE 5.14: Here for a 3-way splitter with one barrier in each side branch S_1 and S_2 , the ‘saturated phase times’ τ_{1s} (thick solid), τ_{2s} (thick dotted) and τ_{rs} (dashed) are shown as a function of ‘ w_2 ’. For better visibility, while plotting all three quantities are divided by 50. The square modulus of transmission amplitude through the 2nd barrier $|t_2|^2$ (solid) and the reflection amplitude $|r|^2$ (double dot-dashed) are shifted upwards along the the positive y -direction by 3. The different system parameters are $E = 1$, $V_1 = 15$, $V_2 = 5$, $lb_1 = 100.0$, $lb_2 = 0.5$ and $w_1 = 2.5$.

keep $V_2 (= 5)$ unaltered and reduce lb_2 . For very small $lb_2 (= 0.5)$ we see from Fig. 5.13 that τ_1 is negative for almost the whole range of lb_1 -values showing ‘time-advancement’ and eventually after a sharp decrease saturates to a negative value of $\tau_{s1} = -4.514$ implying ‘Hartman effect’ with advanced time. It might be noted that, in principle, the ‘time-advancement’ (Fig. 5.13) can be measured experimentally as $|t_1|^2$ has a non-zero finite value for a small range of lb_1 at lower lb_1 regime where τ_1 is negative. In the inset we plot the corresponding τ_2 and $|t_2|^2$ as function of lb_1 . Again the values of τ_2 remains different from the one dimensional tunneling through a barrier of strength V_2 and width lb_2 in the whole range of lb_1 implying ‘quantum nonlocality’. In the cases discussed so far τ_2 vary more sharply in small lb_1 regime. Further the inset in Fig. 5.13 shows a dip in τ_2 at parameter regimes where $|t_2|^2$ has a minimum. For a wave packet with large spread in real space it is possible that the leading edge of the wave packet reaches the barrier much earlier than the peak of the packet. This leading edge in turn can tunnel through to produce a peak in the other end of the barrier much before the incident wave packet reaches the barrier region, sometimes referred to as pulse reshaping effect. This, in general, causes ‘time advancement’ [58]. This negative delay does not violate causality, however, the time is bounded from the below. In the presence of square wells in one dimensional systems negative time delays have been observed. This effect is termed as ‘ultra Hartman effect’ [see for details [119]].

As the next case we consider the same Y-junction network system with two side branches, each containing a potential barrier. The width of the barrier in arm S_1 is set at a large value (say 100) where all the phase times get saturated. Now we shift the position of the barrier in arm S_2 away from the junction and study its effect on the saturated transmission and reflection phase times. In Fig. 5.14 we have plotted all these three quantities τ_{s1} , τ_{s2} and τ_{sr}

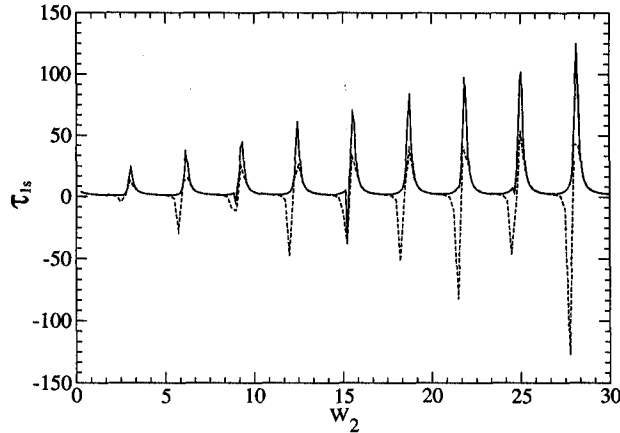


FIGURE 5.15: Here for a 3-way splitter with one barrier in each side branch S_1 and S_2 , the ‘saturated phase time’ τ_{1s} is plotted as a function of ‘ w_2 ’. The dashed and solid curves are for $lb_2 = 0.5$ and 2.0 respectively. Other system parameters are $E = 1$, $V_1 = 15$, $V_2 = 5$, $lb_1 = 100.0$ and $w_1 = 2.5$.

as a function w_2 . Earlier we have shown in Fig. 5.12 that by changing a nonlocal parameter V_2 one can tune τ_{s1} whereas Fig. 5.14 shows change of another parameter w_2 can tune τ_{s1} nonlocally. Note that τ_{s2} , τ_{sr} also depend on w_2 . From Fig. 5.14 we see that $|t_2|^2$ ($|r|^2$) shows resonances (anti-resonances) as a function of w_2 . These resonances are associated with resonances in all three phase times. Among which τ_{s1} shows maxima-minima structures at these resonance w_2 values whereas other two phase times show only positive peaks. As $|t_2|^2$ and $|r|^2$ have finite non-zero values, these variations in phase times should, in principle, be observable in experiments. In Fig. 5.15 we have plotted τ_{s1} as a function w_2 for two different values of the width lb_2 of the barrier in arm S_2 . Note that as we increase the width lb_2 , the frequency of getting negative saturation values (τ_{s1}) reduces (see the solid curve in Fig. 5.15) and increasing the width lb_2 further, the negative saturation goes away. This is in agreement with the discussions in previous paragraph.

Finally consider a similar system as that shown in Fig. 5.10, but in presence of $N(\geq 2)$ identical side branches and study phase time as a function of increasing N . All the side branches being identical the ‘phase times’ for transmission through each of these arms $S_n, n = 2, 3, \dots, N$ saturate to the same value τ_s for very large lb_n . In Fig. 5.16 we plot the saturation value τ_s as a function of the total number of side branches N present in the system. From the figure we see that for $V = 5$, τ_s first increases with N to a maximum value of 3.776 at $N = 9$ and thereafter keeps on decreasing with the increase of N . As we start reducing the strength of the barriers from 5 we see that for $V = 1.49$ the increasing nature of τ_s in small N range vanishes. In general, at larger N , the decreasing nature of τ_s with N persists, *e.g.*, note the solid curve in Fig. 5.16 plotted at $V = 1.25$, but the initial increase in τ_s is not a generic feature. For larger N transmission amplitude in each side branch reduces with increase in N and hence the corresponding peaks of wave packets reach the far end at earlier times thereby reducing τ_s .

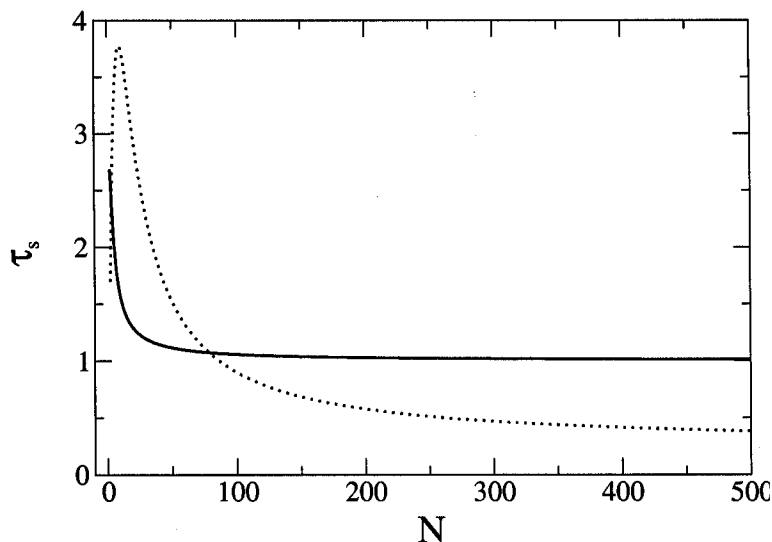


FIGURE 5.16: Here $N(\geq 2)$ number of side branches each with a barrier of strength V and width $lb(= 100)$ are connected with the incident arm S_0 . In each arm barriers start at the same point $w(= 1)$. Thus all the side branches being identical the ‘phase time’ for transmission through these arms $S_n, n = 2, 3, \dots, N$ saturate to the same value τ_s . The saturated ‘phase time’ τ_s is plotted as a function of the total number of side branches N in the system. The dotted and solid curves are for $V = 5.0$ and 1.25 respectively. The incident energy is kept at $E = 1$.

5.4 Conclusions

We have verified the Hartman effect in different quantum ring geometries in the presence of Aharonov-Bohm flux. We have studied the transmission phase time for a ring connected with two leads and reflection phase time for a ring connected with a single lead. Both the studies show that the phase time for a given incident energy becomes independent of the barrier thickness as well as the magnitude of the flux in the limit of opaque barrier. In addition, for the later case of a ring connected with a single lead, introducing a potential well between two successive opaque barriers covering the entire circumference of the ring, we have found that the saturated reflection phase time becomes independent of the width of the well for energies away from the resonances. This implies, as if, the effective velocity of the electron within the well becomes infinite or equivalently length of the well does not count (space collapse or space destroyer). In absence of AB-flux we have obtained analytical expressions for the saturated reflection and transmission phase times for the two above mentioned geometries.

We have then extended our studies on Hartman effect in quantum network consisting of a main one dimensional arm having $N(\geq 2)$ side branches. These side branches may or may not have barriers. In presence of barrier the ‘phase time’ for transmission through a side branch shows the ‘Hartman effect’. In general, as the number of side branches N increases, the saturated ‘phase time’ decreases. Due to quantum nonlocality the ‘phase time’ and its saturated value at any side branch feels the presence of barriers in other branches. Thus one

can tune the saturation value of ‘phase time’ and consequently the superluminal speed in one branch by changing barrier strength or width in any other branch, spatially separated from the former. Moreover Hartman effect with negative saturation times (time advancement) has been observed for some cases. In conclusion generalization of Hartman effect in branched networks exhibits several counter-intuitive results due to quantum non-locality. System parameters such as number of side branches N and barrier widths lb_n , strengths V_n , distance w_n (from J) and incident energy E etc. play very sensitive roles in determining delay times. The delay times are also sensitive to the junction S -matrix elements used for a given problem. In our present problem junction S -matrix is determined uniquely by the wave guide transport methods. Depending on w_n there may be one or several bound states located between the barriers in different branched arms and as a consequence saturated delay time can be varied from the negative (ultra Hartman effect) to positive and vice-versa. We have verified this by looking at the transmission coefficient in the second arm S_2 which exhibits clear resonances as a function of w_2 . Moreover the reported effects are amenable to experimental verifications in the electromagnetic wave-guide networks.

Chapter 6

Conclusions

In this thesis we have discussed several new results. We started off with an introduction in chapter 1 and discussion of some theoretical and experimental background in chapter 2. In chapter 3 we have shown that for an open mesoscopic conductor the system-environment (conductor-lead) coupling plays a very important role in its conductance phenomena. The effect of environment (reservoir) through a term called self energy, which is a function of system-lead coupling, modifies the canonical FSR, which connects the experimentally measurable scattering phase shifts to the DOS of the system. We have verified the FSR for Q1D quantum wire in presence of static impurity. For single channel transport, our studies for attractive impurity show that the self energy is negligible at Fano resonance, a strongly quantum regime arising due to degeneracy of scattering states with quasi - bound states. Thus the canonical form of FSR is shown to be exact at a strongly quantum regime, in contrary to the earlier belief that FSR should be exact only in WKB or quasi-classical limit. Far from the Fano resonance, at almost all energies available for single propagating channel, self energy dependent term is not negligible. We have further shown that, both for attractive and repulsive scatterers, at the upper band edge the energy derivative of self energy vanishes making canonical FSR exact. In multichannel propagation, again, we have obtained the same results. We further observed that for attractive impurity, the energy slope of scattering phase shift (phase time) can be negative indicating super-luminescence. Then in section 3.6 we have explained the origin of Fano resonance, ubiquitous in quantum transports, by an exactly solvable model, namely, one-dimensional Dirac delta potential.

In chapter 4 we have shown the presence of current magnification (CM) in a multi-channel quantum ring in presence of a scatterer that gives rise to mode mixing. This is a non-equilibrium effect driven by the chemical potentials of reservoirs the ring is connected to. We have shown that CM is a robust effect for a system weakly coupled to reservoirs, despite all the mode mixing and cancellations. The circulating currents are large and are mostly with Fano resonances in total transport current. We discussed the impact of impurity strength, system-lead coupling etc. on CM. The persistent current, an equilibrium effect due to external magnetic field, is known to increase with increase in number of propagating channels. In contrast to that, the magnitude of circulating current in CM is independent of the number of propagating channels. We have discussed the experimental possibilities to verify the different predictions of our theoretical calculation of CM.

In chapter 5 we have probed Wigner phase time in different quantum geometries. We have verified Hartman effect in ring geometries (in presence and absence of magnetic flux) and in quantum networks. We have verified the concept of space collapse in ring geometry. We have, further, shown due to quantum non-locality the phase time and its saturated value at any side branch feels the presence of barriers in other branches. Therefore, non-local tuning of saturation phase time is possible. Moreover time - advancement and ultra Hartman effect was observed. The delay times are also sensitive to junction S -matrix and therefore system lead coupling is expected to modify them. The reported effects are amenable to experimental verifications.

Our investigations in the realm of mesoscopic physics have highlighted some basic and important points. We worked in a regime of length scales $< l_\phi$ the phase coherence length. Within this length scale interference effect plays the leading role. This is which gives rise to phenomena like CM and quantum non-locality. Mesoscopic wires being Q1D, confinement plays a crucial role by generating independent channels. Thus multimoded transport along with mode-mixing at the scatterer sites are important in studies of mesoscopic physics. The other principal point is the finite size (inter-facial) effect introduced by system-lead coupling. The inherent small size of mesoscopic samples makes it pertinent to study the impact of this before deciding if in some special cases such effects could be neglected.

In general electrons at or near the Fermi level take part in quantum transport. In low temperature transport in mesoscopic systems electrons are assumed to be non-interacting as we have done throughout this thesis. However, in mesoscopic sample sizes, electron-electron coupling should play a crucial role. A full many body calculation incorporating various interactions of electrons with other electrons, phonons, electromagnetic fields, other excitations etc. is a way forward. At the Fermi level, electrons of a normal metal being unpolarized [120] we often neglect the associated spin degree. But for ferromagnetic metals, the electrons can occupy either up or down states at Fermi energy. Thus electronic current is spin-polarized. A spin-polarized FET like transistor has been proposed [121] in which conductance can be controlled by choosing polarization of the reservoirs and a gate voltage utilizing Rashba spin-orbit effect. Spin polarized transport and spintronics are other future direction. Quantum adiabatic transport and quantum pump is the other field where both theoretical [122] and experimental [123] progresses have been achieved. Other interesting areas are single electron tunneling, quantum chaos in micro-structures, mesoscopic structures combining normal metal and super-conducting components etc.

With the ever increasing miniaturization, the transport concepts derived from classical drift-diffusion theory does not remain valid in characterization of sub-micron sized devices. The currently available devices contain feature sizes of $\sim 100nm$. With the advent of nanotechnology it appears that, sooner rather than later, quantum effects will become very important in operations of futuristic room temperature devices of dimensions in the molecular range. STM, AFM techniques may be useful to achieve such devices. The effects we have studies in this thesis can be verified in low temperature experimental facilities that are currently available. In addition, some of the effects discussed may find applications in futuristic devices.

Appendix A

Scattering and transition amplitudes in Q1D quantum wire

In this appendix we recall the ‘mode rescaling procedure’ [60] to obtain different scattering and transition amplitudes of a multi-channel Q1D quantum wire in presence of a Dirac delta type static impurity potential.

A.1 Mode rescaling procedure

Bagwell [60] introduced a very useful technique, namely, ‘mode rescaling procedure’ to study multi-channel systems as shown in Fig. 2.8 with ‘singular’ impurity potential. This method we have used in our study on Q1D geometries, namely, the quantum wire and the mesoscopic ring, in presence of Dirac δ impurity. Below we sketch the ‘mode rescaling procedure’ which would be repeatedly referred in the body of the thesis.

Using $\psi(x, y)$ from Eq. (2.39) into the Schrödinger Eq. (3.63a), we obtain an equation of motion for the Fourier coefficients c_n as

$$\frac{d^2 c_n(x)}{dx^2} + k_n^2 c_n(x) = \sum_m \Gamma_{nm}(x) c_m(x), \quad (\text{A.1})$$

where $\Gamma_{nm}(x)$ are the mode coupling constants which give the amount of mixing between different modes at the impurity potential as

$$\Gamma_{nm}(x) = \frac{2m_e}{\hbar^2} \int dy \chi_n^*(y) V_d(x, y) \chi_m(y). \quad (\text{A.2})$$

The longitudinal wave vector k_n becomes n dependent wave vector as

$$k_n^2 = \frac{2m_e}{\hbar^2} (E - E_n). \quad (\text{A.3})$$

The sum on the right hand side of Eq. (A.1) includes both $m = n$ and $m \neq n$ terms *i.e.* contributions from all the modes are taken into account. Now we consider a singular

potential as the impurity, *e.g.*, a Dirac-delta function potential at $x = 0$ and $y = y_i$ in the quasi-one-dimensional (Q1D) wire sample as shown in Fig. A.1. Thus

$$V_d(x, y) = \gamma \delta(x) \delta(y - y_i), \quad (\text{A.4})$$

with strength γ . Using Eq. (A.4) in Eq. (A.2) and then the orthogonality condition for the normal modes, Eq. (A.1) reduces to

$$\left. \frac{dc_n(x)}{dx} \right|_{x=0^+} - \left. \frac{dc_n(x)}{dx} \right|_{x=0^-} = \sum_m \Gamma_{nm} c_m(0), \quad (\text{A.5})$$

where the x-independent mode coupling constant

$$\Gamma_{nm} = \frac{2m_e \gamma}{\hbar^2} \chi_n^*(y_i) \chi_m(y_i) \quad (\text{A.6})$$

are proportional to the strength of the impurity and the size of the wave-function at the impurity.

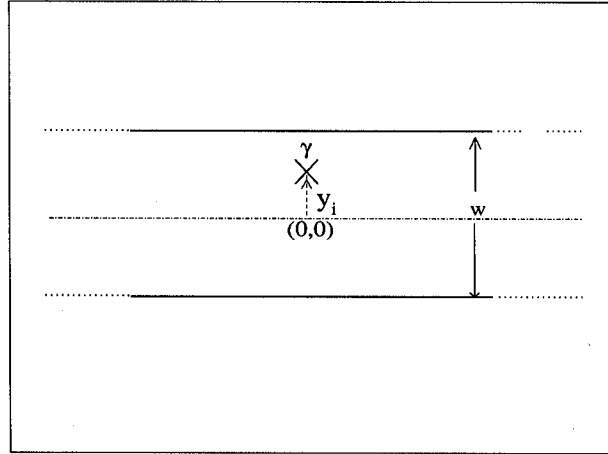


FIGURE A.1: Quasi-one-dimensional wire with a Dirac-delta function impurity potential $V(x, y) = \gamma \delta(x) \delta(y - y_i)$, marked as \times , of strength γ is situated at $x = 0$ and $y = y_i$.

In the regions where the impurity potential is absent *eg.* on the left and right of the impurity, the solutions to Eq. (A.1) are

$$c_n(x) = \begin{cases} A_n e^{ik_n x} + B_n e^{-ik_n x}, & x < 0 \\ C_n e^{ik_n x} + D_n e^{-ik_n x}, & x > 0, \end{cases} \quad (\text{A.7})$$

for the propagating modes and for evanescent modes

$$c_n(x) = \begin{cases} A_n e^{-\kappa_n x} + B_n e^{\kappa_n x}, & x < 0 \\ C_n e^{-\kappa_n x} + D_n e^{\kappa_n x}, & x > 0. \end{cases} \quad (\text{A.8})$$

with $\kappa_n^2 = \frac{2m_e}{\hbar^2} (E_n - E)$. From Eq. (A.5), for n -th propagating and evanescent mode using respectively Eq. (A.7) and Eq. (A.8) we obtain

$$i k_n (C_n - D_n) - i k_n (A_n - B_n) = \sum_m \Gamma_{nm} (A_m + B_m) \quad (\text{A.9})$$

$$-\kappa_n (C_n - D_n) + \kappa_n (A_n - B_n) = \sum_m \Gamma_{nm} (A_m + B_m). \quad (\text{A.10})$$

Continuity of wave function at the position of the impurity potential gives another boundary condition

$$A_n + B_n = C_n + D_n \quad (\text{A.11})$$

for all normal mode indices n . Following normal textbook on Quantum mechanics, we consider particles incident only from the left *i.e.* $D_n = 0$ for all n . Besides, for evanescent waves, $A_n = 0$ as far away from the impurity the evanescent waves vanish. Thus we obtain from Eq. (A.11), $A_n + B_n = C_n$ for all propagating modes and $B_n = C_n$ for all evanescent modes. Once A_n , B_n and C_n are known, the current transmission and reflection amplitudes in the scattering matrix can be obtained as $\tilde{t}_{nm} = \sqrt{\frac{k_m}{k_n}} t_{nm} = \sqrt{\frac{k_m}{k_n}} \frac{C_m}{A_n}$ and $\tilde{r}_{nm} = \sqrt{\frac{k_m}{k_n}} r_{nm} = \sqrt{\frac{k_m}{k_n}} \frac{B_m}{A_n}$ respectively. Bagwell showed [60] a very effective technique for solving infinite set of coupled equations (A.9), (A.10) and (A.11) by truncating them to a finite size.

For an example, consider electron is coming with an energy $E_2 < E < E_3$ so that two propagating modes are present in the system. In addition, let us consider only two evanescent modes in the Q1D wire. For the case when mode one is incident on the impurity *i.e.* $A_2 = 0$ and $B_2 = C_2$ we can write the coupled matrix equation from Eq. (A.9), (A.10) and (A.11) as

$$\begin{bmatrix} -2ik_1 \\ 0 \\ 0 \\ 0 \end{bmatrix} = \begin{bmatrix} \Gamma_{11} - 2ik_1 & \Gamma_{12} & \Gamma_{13} & \Gamma_{14} \\ \Gamma_{21} & \Gamma_{22} - 2ik_2 & \Gamma_{23} & \Gamma_{24} \\ \Gamma_{31} & \Gamma_{32} & \Gamma_{33} + 2\kappa_3 & \Gamma_{34} \\ \Gamma_{41} & \Gamma_{42} & \Gamma_{43} & \Gamma_{44} + 2\kappa_4 \end{bmatrix} \begin{bmatrix} t_{11} \\ t_{12} \\ t_{13} \\ t_{14} \end{bmatrix}. \quad (\text{A.12})$$

In Eq. (A.12), let us eliminate the highest evanescent mode *i.e.* expressing t_{14} in terms of t_{11} , t_{12} and t_{13} , we obtain the 3×3 matrix equation

$$\begin{bmatrix} -2ik_1 \\ 0 \\ 0 \end{bmatrix} = \begin{bmatrix} \Gamma_{11,4} - 2ik_1 & \Gamma_{12,4} & \Gamma_{13,4} \\ \Gamma_{21,4} & \Gamma_{22,4} - 2ik_2 & \Gamma_{23,4} \\ \Gamma_{31,4} & \Gamma_{32,4} & \Gamma_{33,4} + 2\kappa_3 \end{bmatrix} \begin{bmatrix} t_{11} \\ t_{12} \\ t_{13} \end{bmatrix}, \quad (\text{A.13})$$

where the previous ‘mode coupling constant’ is rescaled by the highest possible evanescent mode (*i.e.* mode four) present in the system as

$$\Gamma_{nm,4} = \Gamma_{nm} \frac{2\kappa_4}{\Gamma_{44} + 2\kappa_4}, \quad n, m = 1, 2, 3. \quad (\text{A.14})$$

In Eq. (A.13) further expressing t_{13} in terms of other two transmission coefficients *i.e.* t_{11} and t_{12} we obtain

$$\begin{bmatrix} -2ik_1 \\ 0 \end{bmatrix} = \begin{bmatrix} \Gamma_{11,3-4} - 2ik_1 & \Gamma_{12,3-4} \\ \Gamma_{21,3-4} & \Gamma_{22,3-4} - 2ik_2 \end{bmatrix} \begin{bmatrix} t_{11} \\ t_{12} \end{bmatrix}, \quad (\text{A.15})$$

where the new ‘rescaled mode coupling constants’ are

$$\Gamma_{nm,3-4} = \Gamma_{nm,4} \frac{2\kappa_3}{\Gamma_{33} + 2\kappa_3}, \quad n, m = 1, 2. \quad (\text{A.16})$$

In general, for electron incident on the impurity with energy lying in the range $E_p < E < E_{p+1}$ *i.e.* maximum number of propagating modes present in the system is $p (\geq 1)$, the rescaled ‘mode coupling constant’ is

$$\Gamma_{nm,(p+1)-e} = \Gamma_{nm,(p+2)-e} \frac{2\kappa_{p+1}}{\Gamma_{p+1,p+1} + 2\kappa_{p+1}}, \quad n, m = 1, 2, \dots, p, \quad (\text{A.17})$$

where e is the maximum number of evanescent modes. From the above rescaling procedure, it is clear that the total effect of the evanescent modes comes into ‘rescaled mode coupling constants’ which eventually become energy dependent [compare Eq. (A.6) and Eq. (A.17)]. Whenever incident energy of the electron aligns with the bottom of a subband, all the modes completely decouple from each other and each separate mode shows perfect transmission. For example, in the system considered above with two propagating modes, if $E = E_3$, then from Eq. (A.16), $\Gamma_{nm,3-4} = 0$ and from Eq. (A.15), $t_{11} = 1$ and $t_{12} = 0$. For the case when mode two is incident on the impurity, a similar equation for t_{21} and t_{22} , as Eq. (A.15), gives $t_{21} = 0$ and $t_{22} = 1$. In the mode rescaling procedure, the infinite set of coupled equations (Eq. (A.9), Eq. (A.10)) are truncated to a finite set of equations. In this process of truncation, to get the correct result, the number of evanescent modes are considered depending upon the strength of the impurity in a way such that the density of states of the evanescent modes ($\frac{1}{W} \frac{m_e}{\hbar^2 \kappa_n}$) times the strength of the impurity is very small *i.e.* $\frac{1}{W} \frac{m_e}{\hbar^2 \kappa_n} \gamma \ll 1$.

A.2 transmission and reflection amplitudes

Considering one propagating mode in Eq. (A.12) *i.e.* when energy of incident electron lies in the range $E_1 < E < E_2$, one can obtain (see [60])

$$t_{11} = 1 + r_{11}, \quad (\text{A.18})$$

$$\text{where } r_{11} = \frac{\Gamma_{11,2-e}}{2ik_1 \left(1 - \frac{\Gamma_{11,2-e}}{2ik_1}\right)} \quad (\text{A.19})$$

$$\text{and } |\tilde{t}_{11}|^2 + |\tilde{r}_{11}|^2 = 1 \quad (\text{A.20})$$

which is the current conservation identity. In the similar fashion, for two propagating modes *i.e.* when energy of incident electron lies in the range $E_2 < E < E_3$, Eq. (A.12) gives

$$t_{11} = 1 + r_{11}, \quad (\text{A.21})$$

$$\text{where } r_{11} = \frac{\Gamma_{11,3-e}}{2ik_1 \left(1 - \frac{\Gamma_{11,3-e}}{2ik_1} - \frac{\Gamma_{22,3-e}}{2ik_2}\right)}; \quad (\text{A.22})$$

$$t_{12} = r_{12} = \frac{\Gamma_{21,3-e}}{2ik_2 \left(1 - \frac{\Gamma_{11,3-e}}{2ik_1} - \frac{\Gamma_{22,3-e}}{2ik_2}\right)} \quad (\text{A.23})$$

$$t_{21} = r_{21} = \frac{\Gamma_{12,3-e}}{2ik_1 \left(1 - \frac{\Gamma_{11,3-e}}{2ik_1} - \frac{\Gamma_{22,3-e}}{2ik_2}\right)}; \quad (\text{A.24})$$

$$t_{22} = 1 + r_{22}, \quad (\text{A.25})$$

$$\text{where } r_{22} = \frac{\Gamma_{22,3-e}}{2ik_2 \left(1 - \frac{\Gamma_{11,3-e}}{2ik_1} - \frac{\Gamma_{22,3-e}}{2ik_2}\right)}. \quad (\text{A.26})$$

In this case, the current conservation satisfies the following equations

$$|t_{11}|^2 + |t_{12}|^2 + |r_{11}|^2 + |r_{12}|^2 = 1, \quad (\text{A.27})$$

$$|t_{21}|^2 + |t_{22}|^2 + |r_{21}|^2 + |r_{22}|^2 = 1. \quad (\text{A.28})$$

From Eq. (A.19), Eq. (A.23), Eq. (A.23), Eq. (A.24) and Eq. (A.26) one can obtain the reflection amplitudes \tilde{r}_{nm} (see Ref. ([60])) as

$$\tilde{r}_{nm} = \frac{-i \frac{\Gamma_{nm}}{2\sqrt{k_n k_m}}}{1 + \sum_j^e \frac{\Gamma_{jj}}{2k_j} + i \sum_j^p \frac{\Gamma_{jj}}{2k_j}}, \quad (\text{A.29})$$

where \sum_j^e represents a sum over all the evanescent modes while \sum_j^p represents a sum over all the propagating modes considered in the problem. Here the subscripts m and n correspond propagating modes. Eq. (A.29) also holds for intermode transmission amplitudes \tilde{t}_{nm} where $m \neq n$, as we can see from Eq. (A.23) and Eq. (A.24). The intramode transmission amplitudes \tilde{t}_{nn} are obtained from \tilde{r}_{nn} as $\tilde{t}_{nn} = 1 + \tilde{r}_{nn}$ (note Eq. (A.18) and Eq. (A.19)).

A.3 Transition amplitude from propagating to evanescent mode

From Eq. (A.12), for one propagating mode and one evanescent mode we find out the transition amplitude from propagating mode 1 to evanescent mode 2 as

$$t_{12} = \frac{-\frac{\Gamma_{12}}{2\kappa_2}}{1 + \frac{\Gamma_{22}}{2\kappa_2} + i \frac{\Gamma_{11}}{2k_1}}. \quad (\text{A.30})$$

Similarly, for two evanescent modes Eq. (A.12), we calculate the transition amplitudes to find,

$$t_{12} = \frac{-\frac{\Gamma_{12}}{2\kappa_2}}{1 + \frac{\Gamma_{22}}{2\kappa_2} + \frac{\Gamma_{33}}{2\kappa_3} + i \frac{\Gamma_{11}}{2k_1}}. \quad (\text{A.31})$$

$$t_{13} = \frac{-\frac{\Gamma_{13}}{2\kappa_3}}{1 + \frac{\Gamma_{22}}{2\kappa_2} + \frac{\Gamma_{33}}{2\kappa_3} + i \frac{\Gamma_{11}}{2k_1}}. \quad (\text{A.32})$$

Increasing number of evanescent modes in Eq. (A.12), we have also obtained the the general expression for the transition amplitude from the propagating mode to the j -th evanescent mode as

$$t_{1j} = \frac{-\frac{\Gamma_{1j}}{2\kappa_j}}{1 + \sum_{j>1}^e \frac{\Gamma_{jj}}{2\kappa_j} + i \frac{\Gamma_{11}}{2k_1}},$$

which is the Eq. (3.28) in section 3.4.

Appendix B

Global DOS in a Q1D quantum wire

In this appendix B we present the derivation of Eq.(3.27) *i.e.* change in global DOS in presence of a Dirac delta type static scatterer in a multi-channel Q1D quantum wire. As an example, here we consider only two propagating modes. The global density of states is given by

$$\rho(E) = \sum_{m,k_m} \delta(E - E_{m,k_m}) \int_{-\infty}^{\infty} dx \int_{-\frac{W}{2}}^{\frac{W}{2}} dy \sum_{n,k_n} |\psi_{n,k_n}(x,y)|^2 \quad (\text{B.1})$$

where $\psi_{n,k_n}(x,y) = \sum_n c_n^{(m)}(x)\chi_n(y)$ and E_{m,k_m} is the energy of an electron in the leads. $E_{m,k_m} = \frac{m^2\pi^2\hbar^2}{2m_e W^2} + \frac{\hbar^2 k_m^2}{2m_e}$, where $m = \pm 1, \pm 2$, as there are two propagating modes in the leads. As $\chi_n(y)$'s form an orthonormal set,

$$\rho(E) = \sum_{m,k_m} \delta(E - E_{m,k_m}) \int_{-\infty}^{\infty} dx \sum_n |c_n^{(m)}(x)|^2$$

First considering electron incident from the left, the partial density of states is

$$\begin{aligned} \rho_1(E) &= \frac{1}{\hbar v_1} \int_{-\infty}^{\infty} dx \sum_n |c_n^{(1)}(x)|^2 + \frac{1}{\hbar v_2} \int_{-\infty}^{\infty} dx \sum_n |c_n^{(2)}(x)|^2 \\ &= \frac{1}{\hbar v_1} T1 + \frac{1}{\hbar v_2} T2 \end{aligned} \quad (\text{B.2})$$

So

$$\rho(E) = \rho_1(E) + \rho_2(E)$$

where $\rho_2(E)$ is the partial DOS for electron incident from the right. Here, $v_1 = \frac{\hbar k_1}{m_e}$ and $v_2 = \frac{\hbar k_2}{m_e}$.

Now,

$$T1 = \int_{-\infty}^{\infty} dx \sum_n |c_n^{(1)}(x)|^2$$

where electron is incident in the fundamental mode (denoted by superscript(1)),

$$c_1^{(1)}(x) = \begin{cases} e^{ik_1x} + \tilde{r}_{11}e^{-ik_1x} & \text{for } x < 0 \\ \tilde{t}_{11} e^{ik_1x} & \text{for } x > 0 \end{cases}$$

$$c_2^{(1)}(x) = \begin{cases} \tilde{r}_{12} e^{-ik_2x} & \text{for } x < 0 \\ \tilde{t}_{12} e^{ik_2x} & \text{for } x > 0 \end{cases}$$

and for $n > 2$,

$$c_n^{(1)}(x) = \begin{cases} t_{1n} e^{\kappa_n x} & \text{for } x < 0 \\ t_{1n} e^{-\kappa_n x} & \text{for } x > 0 \end{cases}$$

So,

$$T1 = \int_{-\infty}^0 dx [1 + |\tilde{r}_{11}|^2 + 2|\tilde{r}_{11}| \cos(2k_1x + \eta_1)] + \int_0^{\infty} dx |\tilde{t}_{11}|^2$$

$$+ \int_{-\infty}^0 dx |\tilde{r}_{12}|^2 + \int_0^{\infty} dx |\tilde{t}_{12}|^2 + \frac{|t_{13}|^2}{\kappa_3} + \frac{|t_{14}|^2}{\kappa_4} + \dots$$

Here, η_1 is defined as $\tilde{r}_{11} = |\tilde{r}_{11}|e^{-i\theta_1}$.

Similarly, when electron is incident in the 1st excited mode (denoted by superscript(2))

$$T2 = \int_{-\infty}^{\infty} dx \sum_n |c_n^{(2)}(x)|^2$$

$$= \int_{-\infty}^0 dx [1 + |\tilde{r}_{22}|^2 + 2|\tilde{r}_{22}| \cos(2k_2x + \eta_2)] + \int_0^{\infty} dx |\tilde{t}_{22}|^2$$

$$+ \int_{-\infty}^0 dx |\tilde{r}_{21}|^2 + \int_0^{\infty} dx |\tilde{t}_{21}|^2 + \frac{|t_{23}|^2}{\kappa_3} + \frac{|t_{24}|^2}{\kappa_3} + \dots$$

Here, η_2 is defined as $\tilde{r}_{22} = |\tilde{r}_{22}|e^{-i\eta_2}$. Therefore,

$$\rho_1(E) = \frac{1 + |\tilde{r}_{11}|^2}{hv_1} \int_{-\infty}^0 dx + \frac{1 + |\tilde{r}_{22}|^2}{hv_2} \int_{-\infty}^0 dx + \frac{|\tilde{r}_{12}|^2}{hv_1} \int_{-\infty}^0 dx + \frac{|\tilde{r}_{21}|^2}{hv_2} \int_{-\infty}^0 dx$$

$$+ \frac{2|\tilde{r}_{11}|}{hv_1} \int_{-\infty}^0 dx \cos(2k_1x + \eta_1) + \frac{2|\tilde{r}_{22}|}{hv_2} \int_{-\infty}^0 dx \cos(2k_2x + \eta_2)$$

$$+ \frac{|\tilde{t}_{11}|^2 + |\tilde{t}_{12}|^2}{hv_1} \int_0^{\infty} dx + \frac{|\tilde{t}_{21}|^2 + |\tilde{t}_{22}|^2}{hv_2} \int_0^{\infty} dx$$

$$+ \frac{1}{hv_1} \left(\frac{|t_{13}|^2}{\kappa_3} + \frac{|t_{14}|^2}{\kappa_4} + \dots \right) + \frac{1}{hv_2} \left(\frac{|t_{23}|^2}{\kappa_3} + \frac{|t_{24}|^2}{\kappa_4} + \dots \right).$$

Due to time reversal symmetry, $\tilde{r}_{12} = \tilde{r}_{21}$ & $\tilde{t}_{12} = \tilde{t}_{21}$. We put $\tilde{r}_{12} = \tilde{r}_{21}$, $\tilde{r}_{21} = \tilde{r}_{12}$, $\tilde{t}_{12} = \tilde{t}_{21}$, $\tilde{t}_{21} = \tilde{t}_{12}$ in the 3rd, 4th, 7th and 8th terms respectively.

Therefore,

$$\begin{aligned}
\rho_1(E) &= \frac{1 + |\tilde{r}_{11}|^2 + |\tilde{r}_{21}|^2}{hv_1} \int_{-\infty}^0 dx + \frac{1 + |\tilde{r}_{12}|^2 + |\tilde{r}_{22}|^2}{hv_2} \int_{-\infty}^0 dx \\
&+ \frac{|\tilde{t}_{11}|^2 + |\tilde{t}_{21}|^2}{hv_1} \int_0^{\infty} dx + \frac{|\tilde{t}_{12}|^2 + |\tilde{t}_{22}|^2}{hv_2} \int_0^{\infty} dx \\
&+ \frac{2|\tilde{r}_{11}|}{hv_1} \int_{-\infty}^0 dx \cos(2k_1x + \eta_1) + \frac{2|\tilde{r}_{22}|}{hv_2} \int_{-\infty}^0 dx \cos(2k_2x + \eta_2) \\
&+ \frac{1}{hv_1} \left(\frac{|t_{13}|^2}{\kappa_3} + \frac{|t_{14}|^2}{\kappa_4} + \dots \right) + \frac{1}{hv_2} \left(\frac{|t_{23}|^2}{\kappa_3} + \frac{|t_{24}|^2}{\kappa_4} + \dots \right).
\end{aligned}$$

Now adding and subtracting the following terms,

$$\frac{|\tilde{t}_{11}|^2}{hv_1} \int_{-\infty}^0 dx, \frac{|\tilde{t}_{21}|^2}{hv_1} \int_{-\infty}^0 dx, \frac{|\tilde{t}_{22}|^2}{hv_2} \int_{-\infty}^0 dx, \frac{|\tilde{t}_{12}|^2}{hv_2} \int_{-\infty}^0 dx,$$

we get,

$$\begin{aligned}
\rho_1(E) &= \frac{1 + |\tilde{r}_{11}|^2 + |\tilde{r}_{21}|^2 + |\tilde{t}_{11}|^2 + |\tilde{t}_{21}|^2}{hv_1} \int_{-\infty}^0 dx \\
&+ \frac{1 + |\tilde{r}_{12}|^2 + |\tilde{r}_{22}|^2 + |\tilde{t}_{12}|^2 + |\tilde{t}_{22}|^2}{hv_2} \int_{-\infty}^0 dx \\
&+ \frac{2|\tilde{r}_{11}|}{hv_1} \int_{-\infty}^0 dx \cos(2k_1x + \eta_1) + \frac{2|\tilde{r}_{22}|}{hv_2} \int_{-\infty}^0 dx \cos(2k_2x + \eta_2) \\
&+ \frac{1}{hv_1} \left(\frac{|t_{13}|^2}{\kappa_3} + \frac{|t_{14}|^2}{\kappa_4} + \dots \right) + \frac{1}{hv_2} \left(\frac{|t_{23}|^2}{\kappa_3} + \frac{|t_{24}|^2}{\kappa_4} + \dots \right).
\end{aligned}$$

Now $|\tilde{r}_{11}|^2 + |\tilde{r}_{21}|^2 + |\tilde{t}_{11}|^2 + |\tilde{t}_{21}|^2 = 1$ and $|\tilde{r}_{12}|^2 + |\tilde{r}_{22}|^2 + |\tilde{t}_{12}|^2 + |\tilde{t}_{22}|^2 = 1$. Similarly we can calculate $\rho_2(E)$ and thus,

$$\begin{aligned}
\rho(E) &= \frac{2}{hv_1} \int_{-\infty}^{\infty} dx + \frac{2}{hv_2} \int_{-\infty}^{\infty} dx \\
&+ \frac{2|\tilde{r}_{11}|}{hv_1} \int_{-\infty}^{\infty} dx \cos(2k_1x + \eta_1) + \frac{2|\tilde{r}_{22}|}{hv_2} \int_{-\infty}^{\infty} dx \cos(2k_2x + \eta_2) \\
&+ \frac{2}{hv_1} \left(\frac{|t_{13}|^2}{\kappa_3} + \frac{|t_{14}|^2}{\kappa_4} + \dots \right) + \frac{2}{hv_2} \left(\frac{|t_{23}|^2}{\kappa_3} + \frac{|t_{24}|^2}{\kappa_4} + \dots \right).
\end{aligned} \tag{B.3}$$

Now $\frac{2}{hv_1} \int_{-\infty}^{\infty} dx + \frac{2}{hv_2} \int_{-\infty}^{\infty} dx = \rho_0(E)$ i.e. DOS in the absence of scatterer. So we get

$$\begin{aligned}
\rho(E) - \rho_0(E) &= \frac{2|\tilde{r}_{11}|}{hv_1} \int_{-\infty}^{\infty} dx \cos(2k_1x + \eta_1) + \frac{2|\tilde{r}_{22}|}{hv_2} \int_{-\infty}^{\infty} dx \cos(2k_2x + \eta_2) \\
&+ \frac{2}{hv_1} \left(\frac{|t_{13}|^2}{\kappa_3} + \frac{|t_{14}|^2}{\kappa_4} + \dots \right) + \frac{2}{hv_2} \left(\frac{|t_{23}|^2}{\kappa_3} + \frac{|t_{24}|^2}{\kappa_4} + \dots \right).
\end{aligned} \tag{B.4}$$

Appendix C

Scattering amplitudes from double-delta potential in 1D

Considering the symmetric scattering potential in Fig. 3.1, the scattering matrix S of the structure can be found by cascading the scattering matrices of different parts, i.e.,

$$S = \begin{pmatrix} r & t \\ t & r \end{pmatrix} = S_1 \otimes S_2 \otimes S_3,$$

$$\text{where } S_1 = S_3 = \begin{pmatrix} r' & t' \\ t' & r' \end{pmatrix}$$

$$\text{and } S_2 = \begin{pmatrix} 0 & \tau \\ \tau & 0 \end{pmatrix}.$$

Here $\tau = e^{i\phi}$, $\phi = kl$ and $k = \sqrt{\frac{2m}{\hbar^2}E}$. S_2 is the scattering matrix for the free region II of length l between the two scatterers. r' & t' are the reflection & transmission amplitudes due to one of the two potentials when isolated.

After cascading these three matrices the resultant scattering matrix of our system becomes

$$S = \begin{pmatrix} r' + \frac{t'^2\tau^2r'}{1-r'^2\tau^2} & \frac{t'^2\tau}{1-r'^2\tau^2} \\ \frac{t'^2\tau}{1-r'^2\tau^2} & r' + \frac{t'^2\tau^2r'}{1-r'^2\tau^2} \end{pmatrix}.$$

And so,

$$\det[S] = \left(r' + \frac{t'^2\tau^2r'}{1-r'^2\tau^2} \right)^2 - \left(\frac{t'^2\tau}{1-r'^2\tau^2} \right)^2 \quad (\text{C.1})$$

$$= \frac{1}{(1-r'^2\tau^2)^2} (M + N), \quad (\text{C.2})$$

$$\text{where } M = r'^2(1-r'^2\tau^2)^2 \quad (\text{C.3})$$

$$\text{and } N = (1-r'^2\tau^2)(2t'^2r'^2\tau^2 - t'^4\tau^2). \quad (\text{C.4})$$

From Eq.(C.1),

$$\frac{\partial \det[S]}{\partial \phi} = 2 \left(A \frac{\partial A}{\partial \phi} - B \frac{\partial B}{\partial \phi} \right) \quad (\text{C.5})$$

$$\text{where } A = r' + \frac{t'^2 \tau^2 r'}{1 - r'^2 \tau^2} \quad (\text{C.6})$$

$$\text{and } B = \frac{t'^2 \tau}{1 - r'^2 \tau^2}. \quad (\text{C.7})$$

Using Eq. (C.5), (C.6) and (C.7) we find

$$\begin{aligned} \frac{\partial \det[S]}{\partial \phi} &= 2 \left[A \left(2r'B + \frac{2r'^3 \tau^2 B}{1 - r'^2 \tau^2} \right) - B \left(\frac{t'^2 + r'^2 t'^2 \tau^2}{(1 - r'^2 \tau^2)^2} \right) \right] \frac{\partial \tau}{\partial \phi} \\ &+ 2 \left[A \left(1 + B\tau + \frac{2r'^2 \tau^3 B}{1 - r'^2 \tau^2} \right) - B \left(\frac{2r' \tau^2 B}{1 - r'^2 \tau^2} \right) \right] \frac{\partial r'}{\partial \phi} \\ &+ 2 \left[2r' \tau A B - B \left(\frac{2\tau t'}{1 - r'^2 \tau^2} \right) \right] \frac{\partial t'}{\partial \phi}. \end{aligned} \quad (\text{C.8})$$

To obtain Eq. (C.8) we retain the energy dependence of r' , t' and τ . Hence our results correspond to real potentials and we do not parameterize the S matrix in a special way. Now we apply this result to the case of double delta function potential in Fig. 3.2 and illustrate the significance of the last two terms in comparison with the 1st one in Eq. (C.8). We should emphasize here that the calculation in this appendix holds even if the δ -function potential is replaced by the square-well or any arbitrary potential. Thus in the regime where $\frac{\partial r'}{\partial \phi} \rightarrow 0$ and $\frac{\partial t'}{\partial \phi} \rightarrow 0$ and using $\frac{\partial \tau}{\partial \phi} = i\tau$,

$$\frac{\partial \det[S]}{\partial \phi} = 2 \left[A \left(2r'B + \frac{2r'^3 \tau^2 B}{1 - r'^2 \tau^2} \right) - B \left(\frac{t'^2 + r'^2 t'^2 \tau^2}{(1 - r'^2 \tau^2)^2} \right) \right] i\tau. \quad (\text{C.9})$$

At this point we substitute the values of A and B from Eq. (C.6) and Eq. (C.7) respectively to get

$$\frac{\partial \det[S]}{\partial \phi} = 2i \frac{1}{(1 - r'^2 \tau^2)^3} N. \quad (\text{C.10})$$

$$\text{Now, } \theta_f = \frac{1}{2i} \ln(\det[S]) \quad (\text{C.11})$$

$$\text{and so } \frac{\partial \theta_f}{\partial E} = \frac{\partial \theta_f}{\partial \phi} \frac{\partial \phi}{\partial E}.$$

From Eq. (C.11), Eq. (C.2) and Eq. (C.10)

$$\begin{aligned} \frac{\partial \theta_f}{\partial \phi} &= \frac{1}{2i} \frac{1}{\det[S]} \frac{\partial \det[S]}{\partial \phi} \\ &= \frac{1}{1 - r'^2 \tau^2} \frac{1}{\frac{M}{N} + 1}. \end{aligned}$$

Multiplying the numerator and denominator by $\frac{(1-r'^2\tau^2)^*}{1-|r'|^4}$, we get

$$\begin{aligned}\frac{\partial\theta_f}{\partial\phi} &= \frac{1-|r'|^4}{|1-r'^2\tau^2|^2} \frac{(1-r'^2\tau^2)^*}{1-|r'|^4} \frac{1}{\frac{M}{N}+1} \\ &= \frac{1-|r'|^4}{|1-r'^2\tau^2|^2} Q,\end{aligned}\quad (\text{C.12})$$

$$\begin{aligned}\text{where, } Q &= \frac{(1-r'^2\tau^2)^*}{1-|r'|^4} \frac{1}{\frac{M}{N}+1} \\ &= \left[\frac{(1-r'^2\tau^2)^* - 1 + |r'|^4 |\tau|^4}{1-|r'|^4} + 1 \right] \frac{1}{\frac{M}{N}+1}, \\ &(\text{ as } |\tau|^4 = 1).\end{aligned}\quad (\text{C.13})$$

Since $1-|r'|^2 = |t'|^2$

$$Q = \left[\frac{-r'^2\tau^2 + |r'|^4 |\tau|^4}{(1+|r'|^2)|t'|^2} + 1 \right] \frac{1}{\frac{M}{N}+1}.\quad (\text{C.14})$$

Now substituting the values of M and N from Eq. (C.3) and (C.4)

$$Q = \frac{-r'^2\tau^2(1-r'^2\tau^2) + |t'|^2(1+|r'|^2)}{|t'|^2(1+|r'|^2)} \frac{-t'^2\tau^2(t'^2-2r'^2)}{r'^2(1-r'^2\tau^2) - t'^2\tau^2(t'^2-2r'^2)}.\quad (\text{C.15})$$

Using, $r' = |r'| e^{i\theta_r}$ and $t' = |t'| e^{i\theta_t}$,

$$\begin{aligned}Q &= \frac{[|r'|^2|t'|^2|\tau|^4 e^{2i\theta_t} e^{2i(\theta_t-\theta_r)} - |r'|^4|t'|^2|\tau|^4 \tau^2 e^{4i\theta_t} \\ &- |t'|^4 \tau^2 e^{4i\theta_t} - |t'|^4 |r'|^2 \tau^2 e^{4i\theta_t} - 2|r'|^4 |\tau|^4 e^{2i\theta_t} \\ &+ 2|r'|^6 |\tau|^4 \tau^2 e^{2i(\theta_t+\theta_r)} + 2|r'|^2 |t'|^2 \tau^2 e^{2i(\theta_t+\theta_r)} + 2|r'|^4 |t'|^2 \tau^2 e^{2i(\theta_t+\theta_r)}] / D,\end{aligned}$$

$$\begin{aligned}\text{where, } D &= (1+|r'|^2)(-|t'|^4 \tau^2 e^{4i\theta_t} - |r'|^4 \tau^2 e^{4i\theta_r} \\ &+ 2|t'|^2 |r'|^2 \tau^2 e^{2i(\theta_r+\theta_t)} + |r'|^2 e^{2i\theta_r}).\end{aligned}\quad (\text{C.16})$$

Now it follows from unitarity that $e^{2i(\theta_t-\theta_r)} = e^{i\pi} = -1$ and $|\tau|^4 = 1$ and so

$$\begin{aligned}Q &= \frac{[-|r'|^2|t'|^2 e^{2i\theta_t} - |r'|^4|t'|^2 \tau^2 e^{4i\theta_t} - |t'|^4 \tau^2 e^{4i\theta_t} - |t'|^4 |r'|^2 \tau^2 e^{4i\theta_t} - 2|r'|^4 e^{2i\theta_t} \\ &+ 2|r'|^6 \tau^2 e^{2i(\theta_t+\theta_r)} + 2|r'|^2 |t'|^2 \tau^2 e^{2i(\theta_t+\theta_r)} + 2|r'|^4 |t'|^2 \tau^2 e^{2i(\theta_t+\theta_r)}] / D \\ &= \frac{[-e^{2i\theta_t} |r'|^2 \{|t'|^2 + 2|r'|^2\} - (|t'|^2 + |r'|^2 \{|r'|^2 + |t'|^2\}) \\ &(e^{4i\theta_t} |t'|^2 \tau^2 - e^{2i(\theta_t+\theta_r)} 2|r'|^2 \tau^2)] / D.\end{aligned}\quad (\text{C.17})$$

Now inside the $\{\}$ brackets if we use the fact that $|r'|^2 + |t'|^2 = 1$, then

$$Q = \frac{[-e^{2i\theta_t} |r'|^2 (1+|r'|^2) - e^{4i\theta_t} |t'|^2 \tau^2 + 2e^{2i(\theta_t+\theta_r)} |r'|^2 \tau^2] / D,\quad (\text{C.18})$$

Multiplying numerator and denominator above by $e^{-2i(\theta_r+\theta_t)}$ and putting $e^{2i(\theta_t-\theta_r)} = e^{i\pi} = -1$, we get

$$\begin{aligned}Q &= \frac{-e^{-2i\theta_r} |r'|^2 (1+|r'|^2) + \tau^2 (|t'|^2 + |r'|^2) + |r'|^2 \tau^2}{D'}, \\ \text{where, } D' &= D e^{-2i(\theta_r+\theta_t)}.\end{aligned}\quad (\text{C.19})$$

Again using $|r'|^2 + |t'|^2 = 1$,

$$Q = \frac{(1 + |r'|^2)(\tau^2 - |r'|^2 e^{-2i\theta_r})}{D'}. \quad (\text{C.20})$$

Now from expressions (C.19) and (C.16)

$$D' = (1 + |r'|^2)[|r'|^2 e^{-2i\theta_t} - |r'|^4 \tau^2 e^{-2i(\theta_t - \theta_r)} - |t'|^4 \tau^2 e^{2i(\theta_t - \theta_r)} + 2|t'|^2 |r'|^2 \tau^2].$$

As $\theta_t - \theta_r = \frac{\pi}{2}$,

$$D' = (1 + |r'|^2)[|r'|^2 e^{-2i\theta_t} + \tau^2(|r'|^2 + |t'|^2)^2]$$

where of course $|r'|^2 + |t'|^2 = 1$. Substituting D' in Eq. (C.20),

$$Q = \frac{\tau^2 - |r'|^2 e^{-2i\theta_r}}{\tau^2 + |r'|^2 e^{-2i\theta_t}}.$$

Multiplying numerator and denominator of Q by $e^{2i\theta_t}$ and using $e^{2i(\theta_t - \theta_r)} = e^{i\pi} = -1$, we get from (C.12)

$$\frac{\partial \theta_f}{\partial \phi} = \frac{1 - |r'|^4}{|1 - r'^2 \tau^2|^2}$$

Appendix D

Location of the transmission zero

For scattering in three dimensions from spherically symmetric potentials the S -matrix is diagonal in the orbital angular momentum partial wave channels and hence unitarity forces each diagonal-element to be of the form $e^{2i\delta_l}$, where δ_l is the corresponding phase shift. For a one dimensional problem with particles incident from the left $\langle x|k\rangle = \frac{1}{\sqrt{2\pi}} e^{ikx}$ we search for solutions of the form

$$\psi(x) \longrightarrow \begin{cases} e^{ikx} + a_R^{(L)} e^{-ikx} & x \rightarrow -\infty \\ a_T^{(L)} e^{ikx}, & x \rightarrow +\infty \end{cases} \quad (\text{D.1})$$

where $a_R^{(L)}$ is the reflection amplitude and $a_T^{(L)}$ is the transmission amplitude for left incident particles. Similarly for particles incident from the right $\langle x|-k\rangle = \frac{1}{\sqrt{2\pi}} e^{-ikx}$ we look for

$$\psi(x) \longrightarrow \begin{cases} e^{-ikx} + a_R^{(R)} e^{ikx} & x \rightarrow +\infty \\ a_T^{(R)} e^{-ikx}, & x \rightarrow -\infty \end{cases} \quad (\text{D.2})$$

where $a_R^{(R)}$ is the reflection amplitude and $a_T^{(R)}$ is the transmission amplitude for right incident particles. Thus the S -matrix has the form

$$S = \begin{pmatrix} a_T^{(L)} & a_R^{(R)} \\ a_R^{(L)} & a_T^{(R)} \end{pmatrix} \quad (\text{D.3})$$

If $V(x)$ has the symmetry $V(-x) = V(x)$, then clearly $a_R^{(L)} = a_R^{(R)} = a_R$ and $a_T^{(L)} = a_T^{(R)} = a_T$, and accordingly as $S = \begin{pmatrix} a_T & a_R \\ a_R & a_T \end{pmatrix}$, which has the eigenvectors $\frac{1}{\sqrt{2}} \begin{pmatrix} 1 \\ 1 \end{pmatrix}$ and $\frac{1}{\sqrt{2}} \begin{pmatrix} 1 \\ -1 \end{pmatrix}$ belonging to the eigenvalues $a_T + a_R$ and $a_T - a_R$ respectively. Hence with these eigenchannels as basis, the S -matrix is diagonal with $S = \begin{pmatrix} a_T + a_R & 0 \\ 0 & a_T - a_R \end{pmatrix}$. Note that for $V(x) = -\lambda\delta(x)$ we have non-trivial scattering only in the even channel. Thus $a_T - a_R = 1$ and $a_T + a_R = A$. Therefore, $a_T = \frac{1}{2}(1 + A)$. Some authors adopt a different definition of the S -matrix from what we have used [5]. For the present purpose we prefer our convention because as $V \rightarrow 0$ we have $S \rightarrow \mathbb{I}$ as in the case for three dimensional case.

Appendix E

Location of the Resonance and determination of the width

It is best to look at A above the threshold $E = \Delta$ for the opening of the inelastic channel viz. both channels open and track its pole in k so that the sheet structure also becomes clear. Eq. (3.69) gives for the pole

$$q - i\frac{\tilde{\lambda}}{2} + \frac{\tilde{\lambda}_c^2}{4k} = 0. \quad (\text{E.1})$$

At $\tilde{\lambda}_c = 0$ the pole is at $q = i\frac{\tilde{\lambda}}{2}$ or $k^2 = \tilde{\Delta} - \frac{\tilde{\lambda}^2}{4}$ with $\tilde{\Delta} = \frac{2m\Delta}{\hbar^2}$. Now if we switch on $\tilde{\lambda}_c$ and assume $\tilde{\lambda}_c$ is very small, we may write

$$k = \sqrt{\tilde{\Delta} - \frac{\tilde{\lambda}^2}{4}} (1 + \delta_1 + i\delta_2), \quad (\text{E.2})$$

where δ_1 and δ_2 are small and become smaller with smaller $\tilde{\lambda}_c$.

Thus, $q^2 = k^2 - \tilde{\Delta} \simeq -\frac{\tilde{\lambda}^2}{4} + (\tilde{\Delta} - \frac{\tilde{\lambda}^2}{4})(\delta_1^2 - \delta_2^2 + 2\delta_1 + 2i\delta_2 + 2i\delta_1\delta_2)$ and

$$\begin{aligned} q &= i\frac{\tilde{\lambda}}{2} \left[1 - \frac{2(\tilde{\Delta} - \frac{\tilde{\lambda}^2}{4})}{\tilde{\lambda}^2} (\delta_1^2 - \delta_2^2 + 2\delta_1 + 2i\delta_2 + 2i\delta_1\delta_2) \right. \\ &\quad \left. - \frac{8(\tilde{\Delta} - \frac{\tilde{\lambda}^2}{4})^2}{\tilde{\lambda}^4} (\delta_1^2 - \delta_2^2 + 2i\delta_1\delta_2) \right]. \end{aligned} \quad (\text{E.3})$$

In taking the square-root of q^2 we have carefully taken the correct sign so that $\tilde{\lambda}_c \rightarrow 0$, the pole is at $q = i\frac{\tilde{\lambda}}{2}$.

$$\begin{aligned} \frac{1}{k} &= \frac{1}{\sqrt{\tilde{\Delta} - \frac{\tilde{\lambda}^2}{4}}} (1 + \delta_1 + i\delta_2)^{-1} \\ &\simeq \frac{1}{\sqrt{\tilde{\Delta} - \frac{\tilde{\lambda}^2}{4}}} (1 - \delta_1 - i\delta_2 + \delta_1^2 - \delta_2^2 + 2i\delta_1\delta_2 + \dots) \end{aligned} \quad (\text{E.4})$$

If we keep terms up second order in δ in Eqs.(E.3) and (E.4) and use them in Eq.(E.1), we see that the lowest order terms in δ (with $\tilde{\lambda}_c^2$ of the same order) in imaginary and real part of the Eq.(E.1) yield

$$-\frac{2(\tilde{\Delta} - \frac{\tilde{\lambda}^2}{4})}{\tilde{\lambda}} \delta_1 - \frac{\tilde{\lambda}_c^2}{4} \frac{1}{\sqrt{\tilde{\Delta} - \frac{\tilde{\lambda}^2}{4}}} \delta_2 + 8 \frac{(\tilde{\Delta} - \frac{\tilde{\lambda}^2}{4})}{\tilde{\lambda}^4} \tilde{\Delta} \frac{\tilde{\lambda}}{2} \delta_2^2 = 0 \quad (\text{E.5a})$$

$$\frac{2(\tilde{\Delta} - \frac{\tilde{\lambda}^2}{4})}{\tilde{\lambda}} \delta_2 + \frac{\tilde{\lambda}_c^2}{4} \frac{1}{\sqrt{\tilde{\Delta} - \frac{\tilde{\lambda}^2}{4}}} (1 - \delta_1) = 0. \quad (\text{E.5b})$$

Note that although δ_1 is of $O(\tilde{\lambda}_c^4)$, δ_2 is of $O(\tilde{\lambda}_c^2)$. From the above two relations [(E.5a) and (E.5b)]

$$\delta_2 = -\tilde{\lambda}_c^2 \frac{\tilde{\lambda}}{8(\tilde{\Delta} - \frac{\tilde{\lambda}^2}{4})^{3/2}} \quad (\text{E.6})$$

Because δ_1 is of $O(\tilde{\lambda}_c^4)$, the imaginary part of the Eq.(E.1) must contain δ_1 and δ_2^2 which are functions of $\tilde{\lambda}_c^4$. Thus we obtain

$$\delta_1 = \tilde{\lambda}_c^4 \frac{(2\tilde{\Delta} + \tilde{\lambda}^2)}{64(\tilde{\Delta} - \frac{\tilde{\lambda}^2}{4})^3}. \quad (\text{E.7})$$

We use Eqs.(E.7) and (E.6) and find the pole position from Eq.(E.2) as

$$k_p \cong \sqrt{\tilde{\Delta} - \frac{\tilde{\lambda}^2}{4}} + \tilde{\lambda}_c^4 \frac{(2\tilde{\Delta} + \tilde{\lambda}^2)}{64(\tilde{\Delta} - \frac{\tilde{\lambda}^2}{4})^{5/2}} - i \tilde{\lambda}_c^2 \frac{\tilde{\lambda}}{8(\tilde{\Delta} - \frac{\tilde{\lambda}^2}{4})} \quad (\text{E.8})$$

$$E_p - i \frac{\Gamma}{2} \cong \frac{\hbar^2 k_p^2}{2m} \simeq \Delta - \frac{\hbar^2}{2m} \left[\frac{\tilde{\lambda}^2}{4} - \tilde{\lambda}_c^4 \frac{(\tilde{\Delta} + \frac{\tilde{\lambda}^2}{4})}{16(\tilde{\Delta} - \frac{\tilde{\lambda}^2}{4})^2} \right] - i \frac{\hbar^2}{2m} \tilde{\lambda}_c^2 \frac{\tilde{\lambda}}{4(\tilde{\Delta} - \frac{\tilde{\lambda}^2}{4})^{1/2}} \quad (\text{E.9})$$

which are Eqs.(3.70) and Eq.(3.71) in the text.

References

- [1] W. Brattain, W. Shockley and J. Bardeen, Nobel lecture 1956.
- [2] R. P. Feynman, 'There's plenty of room at the bottom' American Physical Society Meeting (Pasadena, CA), 1960 (www.its.caltech.edu/~feynman).
- [3] C. W. J. Beenakker and H. van Houten, *Solid State Physics* **44**, 1 (1991).
- [4] *Mesoscopic phenomena in solids*, edited by B. L. Altshuler, P. A. Lee and R. A. Webb (North-Holland, Amsterdam, 1991).
- [5] S. Datta, *Electronic Transport in Mesoscopic Systems*, Cambridge University Press, Cambridge, UK, (1997).
- [6] B. J. van Wees et al., *Phys. Rev. Lett.* **60**, 848850 (1988).
- [7] D. A. Wharam et al., *J. Phys. C* **21**, L209 (1988).
- [8] M. Büttiker, *IBM J. Res. Dev.* **32**, 317 (1988).
- [9] *Introduction to Mesoscopic Electron Transport* by L.P.Kouwenhoven, G.Schön and L.L.Sohn in 'Mesoscopic Electron Transport' NATO ASI Series E - 345 , eds. L.P.Kouwenhoven, G.Schön and L.L. Sohn, p. 1-44, Kluwer Academic Publishers (1997).
- [10] Y. Aharonov and D. Bohm, *Phys. Rev.* **115**, 485 (1959).
- [11] R. A. Webb et al., *Phys. Rev. Lett.* **54**, 2696 (1985).
- [12] T. J. Thornton et al., *Phys. Rev. Lett.* **56**, 1198 (1986).
- [13] H.Z.Zheng et al., *Phys. Rev. B* **34**, 5635 (1986).
- [14] C. W. J. Beenakker and H. van Houten, "Quantum Transport in Semiconductor Nanostructures," in *Solid State Physics*, edited by H. Ehrenreich and D. Turnbull (Academic, New York, 1991), **44**, 1-228.
- [15] J. B. Xia, *Phys. Rev.* **B45** (1992) 3593.
- [16] Y. Gefen, Y. Imry and M. Ya Azbel, *Phys. Rev. Lett.* **52** (1984) 129.

- [17] S. Washburn and R. A. Webb, *Adv. Phys.* **35**, 375 (1986).
- [18] Y. Imry, *Europhys. Lett.* **1**, 249 (1986).
- [19] R. A. Webb and S. Washburn, *Physics Today*, **41** 52 (1988).
- [20] M. Büttiker, *Phys. Rev. Lett.*, **57**, 1761 (1986).
- [21] S. Bandopadhyay, P. Singha Deo, *Phys. Rev. B* **68**, 113301 (2003).
- [22] P. Singha Deo, Swarnali Bandopadhyay and Sourin Das, *Int. J. Mod. Phys. B*, **16**, 2247 (2002).
- [23] Swarnali Bandopadhyay, Binayak Dutta-Ray and H.S.Mani, *Am. J. Phys.* **72** (12), 1501 (2004).
- [24] Swarnali Bandopadhyay, P. Singha Deo and A. M. Jayannavar, *Phys. Rev. B* **70** 075315 (2004).
- [25] Swarnali Bandopadhyay, Raishma Krishnan, and A. M. Jayannavar, *Solid State Commun.* **131**, 447 (2004).
- [26] Swarnali Bandopadhyay and A. M. Jayannavar, to appear in the proceedings of Condensed Matter Days 2004 (2005); quant-ph/0411161.
- [27] Swarnali Bandopadhyay and A. M. Jayannavar, *Phys. Lett. A*, **335**, 266 (2005).
- [28] Kerson Huang, *Statistical mechanics*, John Wiley, New York, (1987).
- [29] R. Landauer, *IBM J. Res. Dev.*, **1**, 223 (1957).
- [30] Y. Imry, in *Directions in Condensed Matter Physics*, G. Grinstein, G. Mazenko, eds., World Scientific, Singapore (1986).
- [31] A. Yacoby et. al., *Phys. Rev. Lett.* **74** 4047 (1995).
- [32] R. Schuster et. al., *Nature* **385** 417 (1997).
- [33] E. P. Wigner, *Phys. Rev.* **98** (1955) 145.
- [34] M. Büttiker, Y. Imry and R. Landauer, *Phys. Lett.* **96A**, 365 (1983).
- [35] F. Bloch, *Phys. Rev. B* **2**, 109 (1970).
- [36] E. Akkermans et. al., *Phys. Rev. Lett.* **66**, 76 (1991).
- [37] V. Chandrasekhar et. al., *Phys. Rev. Lett.* **67**, 3578 (1991).
- [38] D. Mailly et al., *Phys. Rev. Lett.* **70**, 2020 (1993).
- [39] A. M. Jayannavar and P. Singha Deo, *Phys. Rev. B* **51**, 10175 (1995).

- [40] T. P. Pareek , P. Singha Deo and A. M. Jayannavar , Phys. Rev. B **52**, 14657 (1995).
- [41] A. M. Jayannavar , P. Singha Deo and T. P. Pareek , Physica B **212**, 216 (1995).
- [42] D. F. Shaw, An Introduction to Electronics, 2nd ed., (Longman, London, 1970), p. 51.
- [43] G. Cernicchiaro et al., Phys. Rev. Lett. **79** , 273-276 (1997).
- [44] M. Büttiker, H. Thomas and A. Petre, Z. Phys. B **94**, 133 (1994).
- [45] M. Büttiker, Pramana Journal of Physics,**58**, 241 (2002).
- [46] G. Hackenbroich, Phys. Rep. **343**, 463 (2001).
- [47] V. A. Gopar, Phys. Rev. Lett. **77**, 3005 (1996).
- [48] M. Büttiker and A. M. Martin, Phys. Rev. B **61**, 2737 (2000).
- [49] J. Friedel, Philos. Mag. **43**, 153 (1952).
- [50] Roger Dashen, Shang-keng Ma and Herbert J. Bernstein, Phys. Rev. **187** 345 (1969).
- [51] A.L. Yeyati and M. Büttiker, Phys. Rev. B, **62**, 7307 (2000).
- [52] S. Griffith, Trans. Faraday Soc. **49**, 650 (1953).
- [53] P.S.Deo and A.M.Jayannavar, Mod. Phys. Lett. B **7**, 1045 (1993); P. Singha Deo and A. M. Jayannavar, Pramana Journal of Physics, **56**, 439 (2001) and references therein.
- [54] H. W. Lee, Phys. Rev. Lett. **82**, 2358 (1999).
- [55] T. Taniguchi and M. Buttiker, Phys. Rev.B **60**, 13814 (1999).
- [56] From the derivation of the FSR (one can see the book by Ziman in Ref. [49]), that the scattering phase shift is defined such that when we set the scattering potential to 0 the scattering phase shift is also 0. However, in the double delta function potential the $arg(t) = kl$ when the strength of the delta function potentials are set to zero. Hence the scattering phase shift is $arg(t) - kl$. However, the term coming from the derivative of kl cancels with the term coming from ρ_0 , leading to the Eq. in (3.20).
- [57] F. T. Smith Phys. Rev. **113**, 349 (1960).
- [58] R. Landauer and T. Martin, Rev. Mod. Phys. **66**, 217 (1994).
- [59] P. A. Mello and N. Kumar, *Quantum Transport in Mesoscopic Systems*, Oxford University Press (2004).
- [60] P. F. Bagwell, Phys. Rev.B **41**, 10354(1990).
- [61] P. S. Deo, Phys. Rev. B **53**, 15447 (1996).
- [62] P. Singha Deo, Solid State Commun. **107**, 69 (1998).

- [63] Eugen Merzbacher, *Quantum mechanics*, John Wiley, New York (1999).
- [64] Hua Wu et al., Phys. Rev. B 45, 11960-11967 (1992).
- [65] E. Tekman and P. F. Bagwell, Phys. Rev. B 48, 2553 (1993).
- [66] P. S. Deo and A. M. Jayannavar, Phys. Rev. B, **50**, 11629 (1994).
- [67] We have also found that if we take two delta function potentials in a single channel quantum wire and place two of them close to each other, then for very large strengths of the two potentials, the system becomes almost reflectionless. This is very counter-intuitive as large potentials are expected to give large reflections. It happens because strong potential couples the evanescent modes very strongly to the propagating mode at the positions of the delta potentials, and an incident electron is thrown into the evanescent channels rather than reflected. And since the two potentials are close to each other, the electron can easily tunnel from one potential site to the other and finally go to the transmission channel, again due to the large coupling between the evanescent and transmission channels.
- [68] V. Gasperin, T. Christen and M. Büttiker, Phys. Rev. A **54**, 4022 (1996).
- [69] O. K. Rice, J. Chem. Phys. **1**, 375 (1933).
- [70] U. Fano, Nuovo Cimento **12**, 156 (1935).
- [71] U. Fano, Phys. Rev. **124**, 1866-1878 (1961).
- [72] C.Fühner et al., "Phase measurements using two-channel Fano interference in a semiconductor quantum dot", cond-mat/0307590 (2003).
- [73] K.Kobayashi et al., Phys. Rev. Lett. **88**, 256806 (2002); Phys. Rev. B **68**, 235304 (2003).
- [74] B. F. Bayman and C. J. Mehoke, Am. J. Phys. **51**, 875-883 (1983).
- [75] Kurt Gottfried, *Quantum Mechanics*, Benjamin/Cummings, Boston, **1**, pp. 131-143 (1966).
- [76] J. W. Brown and R. V. Churchill, *Complex Variables and Applications*, McGraw-Hill, New York, 6th ed., pp. 176-179 and 276-281 (1996).
- [77] U. Fano and J. W. Cooper, Reviews of Modern physics, **40** No.3, 441-507 (1968).
- [78] M. V. Moskalets, Euro. Phys. Lett. **41**, 189 (1998).
- [79] T. Choi, C. M. Ryu and A. M. Jayannavar, Int. J. Mod. Phys. **B12**, 2091 (1998) and cond-mat/9808245.
- [80] S.K.Joshi, D.Sahoo and A.M.Jayannavar, Phys. Rev. B **64**, 075320 (2001).

- [81] C. Benjamin et al., *Mod. Phys.Lett. B* **15**, 19 (2001).
- [82] J. Yi et al., *Phys. Rev. B* **65**, 033305 (2002).
- [83] H.Wu et al., *Phys. Rev. B* **68**, 125330 (2003).
- [84] C. Benjamin and A. M. Jayannavar, *Phys. Rev. B* **64**, 2333406 (2001).
- [85] C. Benjamin and A. M. Jayannavar, *Int. J. Mod. Phys. B* **16**, 1787 (2002).
- [86] Hisashi Aikawa et al., *Phys. Rev. Lett.* **92**, 176802 (2004).
- [87] M. Büttiker , *Phys. Rev.B* **32**, 1846 (1985).
- [88] B. Shapiro, *Phys. Rev. Lett.* **50** , 747 (1983).
- [89] S. Pedersen et al., *Phys. Rev. B*, **61**, 5457 (1999).
- [90] C. Benjamin and A. M. Jayannavar, cond-mat/0309133.
- [91] C. Kittel, *Introduction to Solid State Physics*, 7th ed. (Wiley, New York, 1995), Chapter on Semiconductor Crystals.
- [92] M. Büttiker, in *Squid '85-Superconducting Quatum Interference Devices and Their Application*, edited by H. D. Hahlobohm and H. Lüebbig (de Gruyter, Berlin, 1985).
- [93] H. F. Cheung and E. K. Riedel, *Phys. Rev. B* **40**, 9498 (1989).
- [94] A. M. Jayannavar and P. Singha Deo , *Phys. Rev.B* **49**, 13685 (1994).
- [95] R. Tsu and L. Esaki, *Appl. Phys. Lett.* **22**, 562 (1973).
- [96] G. Binning and H. Rohrer, *IBM J. Res. Dev.* **30**, 355 (1986).
- [97] L. A. MacColl, *Phys. Rev.* **40**, 621 (1932).
- [98] S. Anantha Ramakrishna and N. Kumar, *Europhys. Lett.*, **60** (2002) 491; Colin Benjamin and A. M. Jayannavar, *Solid State Commun.*, **121** (2002) 591.
- [99] A. M. Steinberg, P. G. Kwiat, and R. Y. Chiao, *Phys. Rev. Lett.* **71** 708 1993; R. Y. Chiao, P. G. Kwiat, and A. M. Steinberg, *Scientific American*, p. 38-46, August 1993.
- [100] A. Enders and G. Nimtz, *J. Phys. I* **2** (1992) 1693; **3** (1993) 1089; A. Enders and G. Nimtz, *Phys. Rev. E*, **48**, 632 (1993); G. Nimtz, A. Enders and H. Spieker, *ibid* **4** (1994) 565.
- [101] S. Collins, D. Lowe and J. R. Barker, *J. Phys. C* **20**, 6213 (1987); R. S. Dumont and T. L. Marchioro II, *Phys. Rev. A* **47**, 85 (1993).
- [102] P. Guerent, E. Marclay, and H. Meier, *Solid State Commun.* **68**, 977 (1988); Ch. Spielmann, R. Szipocs, A. Sting, and F. Krausz, *Phys. Rev. Lett.* **73**, 2308 (1994); Th. Hills et al., *Phys. Rev. A* **58**, 4784 (1998).

- [103] M. Büttiker and R. Landauer, *Phys. Rev. Lett.* **49**, 1739 (1982).
- [104] M. Büttiker, *Phys. Rev. B* **27**, 6178 (1983).
- [105] E. H. Hauge and J. A. Støvneng, *Rev. Mod. Phys.* **61** (1989) 917.
- [106] T. E. Hartman, *J. Appl. Phys.* **33** (1962) 3427.
- [107] E. H. Hauge, J. P. Falck, and T. A. Fjeldly, *Phys. Rev. B* **36**, 4203 (1987).
- [108] M. Büttiker, *J. Phys. Condensed Matter*, **5** (1993) 9361; M. Büttiker, H. Thomas and A. Prêtre, *Phys. Lett. A* **180** (1993) 364.
- [109] A. M. Jayannavar, G. V. Vijaygobindan and N. Kumar, *Z. Phys. B* **75** (1989) 77; Sandeep K. Joshi, A. Kar Gupta and A. M. Jayannavar, *Phys. Rev.* **B58** (1998) 1092; Sandeep K. Joshi and A. M. Jayannavar, *Solid State Commun.* **106** (1998) 363; *ibid* **111** (1999) 547; For a review see Yan Fyodorov and H. Sommers, *J. Math. Phys.* **38** (1997) 1918.
- [110] V. S. Olkhovsky and E. Recami, *Physics Reports* **214** 339 (1992).
- [111] J. R. Fletcher, *J. Phys. C* **18**, L55 (1985).
- [112] On Universal Properties of Tunnelling, G. Nimtz et al., *APEIRON* **7**, Nr. 1-2, January - April, 2000.
- [113] A. Haibel and G. Nimtz, *Ann. Phys. (Leipzig)* **10**, ed. 8, 707-712 (2001).
- [114] H. G. Winful, *Phys. Rev. Lett.* **91** (2003) 260401; H. G. Winful, *Phys. Rev.* **E68** (2003) 016615; H. G. Winful, *Opt. Express* **10** (2002) 1491.
- [115] V. S. Olkhovsky, E. Recami and G. Salesi, *Europhys. Lett.* **57** 879 (2002).
- [116] A. M. Jayannavar and P. Singha Deo, *Mod. Phys. Lett. B* **8** (1994) 301-310.
- [117] B. C. Gupta, P. Singha Deo and A. M. Jayannavar, *Int. J. Mod. Phys. B* **10** 3595 (1996); Colin Benjamin and A. M. Jayannavar, *Phys. Rev. B* **68** 085325 (2003).
- [118] B. C. Satishkumar, P. John Thomas, A. Govindaraj, and C. N. R. Rao, *Applied Physics Letters* **77(16)** 2530 (2000).
- [119] J. G. Muga, I. L. Egusquiza, J. A. Damborenea, and F. Delgado, *Phys. Rev. A*, **66**, 042115 (2002).
- [120] S. Das Sharma, *American Scientist* Nov/Dec 2001 issue.
- [121] S. Datta and B. Das, *Appl. Phys. Lett.* **56**, 665 (1990).
- [122] P. W. Brouwer, *Phys. Rev. B* **58**, R10135 (1998); Ronald Benjamin and Colin Benjamin, *Phys. Rev. B* **69**, 085318 (2004).
- [123] M. Switkes et al., *Science* **283**, 1905 (1999).

-
- [124] K.Kobayashi et al., Phys. Rev. B **68**, 235304 (2003); Phys. Rev. B **70**, 035319 (2004).
[125] A. J. Leggett, in Granular Nano-Electronics, **251** of NATO Advanced Studies Institute, Series B: Physics, edited by D. K. Ferry, J. R. Barker and C. Jacoboni (Plenum, NY 1991) p. 297.